NPS-51RD0031A

# United States
# Naval Postgraduate School


## HYPERBAROCLINIC ZONES: NUMERICAL ANALYSIS AND APPLICATION TO FRONTS

by

R. J. Renard

23 March 1970

NAVAL POSTGRADUATE SCHOOL
Monterey, California

Rear Admiral R. W. McNitt, USN
Superintendent

R. F. Rinehart
Academic Dean

# HYPERBAROCLINIC ZONES: NUMERICAL ANALYSIS AND APPLICATION TO FRONTS

ABSTRACT:

An objective-numerical scheme for locating and specifying the intensity of hyperbaroclinic zones (HBZs) is presented and applied in both research and operational environments. The operational model, called DGθ*, employs the isobaric gradient of virtual potential temperature (θ*) to specify baroclinicity while a directional second derivative of θ* is the parameter used to locate the HBZs and indirectly give a measure of their intensity.

The DGθ* model is diagnosed from an analysis of modeled temperature profiles and a number of real-atmosphere temperature fields at 1000, 850, 700, and 500 mb, as taken from winter and summer situations in the years 1964-67. Consideration is given to location, intensity, frequency, slope, and vertical and horizontal distribution and consistency of the HBZs in relation to the numerical processing of data. A key synoptic time, 0000 GMT 6 March 1966, serves to exemplify analytical and diagnostic features of the HBZs. The numerically-analyzed 1000 mb fronts, produced operationally by Fleet Numerical Weather Central, Monterey, California since 1965, are statistically and graphically compared to subjectively-analyzed versions for winter and summer periods up to 30 days. The relation of the HBZ to vertical motion and cloud is illustrated by a case study from December 1966.

Experiments, using a high-resolution scheme for analyzing the HBZs, are also presented. A proposed model, employing parameters of vertical stability and isentropic slope, utilizes the thermal detail inherent in vertically-resolved radiosonde data to give an enhanced field of baroclinicity on the constant pressure surface. In addition, it is shown how the model may be coupled with a vertical extrapolation procedure to at least triple the amount of baroclinicity data used for HBZ analysis.

## ACKNOWLEDGMENTS

Space hardly permits citing all of the individuals and groups who helped to bring the research to this terminal point. Without the technical and financial support of the Navy's Fleet Numerical Weather Central, Monterey, California (FNWC), and its leader, Captain Paul Wolff, the study would not have begun. Mr. Leo Clarke, research meteorologist at FNWC, wrote most of the computer programs as well as collaborated in ensuring utility of the model for the objective analysis of fronts by the practicing meteorologist. In addition, much impetus in the early stages was given by financial support from the Office of Naval Research; more recently the project was supported by the Navy Weather Research Facility, Norfolk, Virginia. Appreciation is expressed to the Naval Postgraduate School (PGS) for the facilities afforded this investigator as a member of the faculty. In particular, Dr. George J. Haltiner, Chairman of the Department of Meteorology, PGS, is thanked for his constant encouragement to pursue the goals of this investigation.

For many of those facets of the problem that involved feasibility experimentation and model testing in both time and space scales, many, many students in the Department of Meteorology, PGS, gave valuable assistance, as did the civilian and military technicians associated with the teaching and research programs at the School.

Last, but certainly not least, Dr. Noel E. LaSeur, as well as other members of the Department of Meteorology, Florida State University, are sincerely thanked for giving of their time and advice in fostering a research study which was accepted by Florida State as a suitable doctoral dissertation study.

TABLE OF CONTENTS

LIST OF TABLES

## LIST OF ILLUSTRATIONS

NPS-51RD0031A
23 March 1970

# HYPERBAROCLINIC ZONES: NUMERICAL ANALYSIS AND APPLICATION TO FRONTS*

R. J. Renard

## CHAPTER I

## HISTORICAL BACKGROUND AND OBJECTIVES OF STUDY

It is difficult to ascertain exactly when meteorologists first became aware of, or concerned with, atmospheric baroclinicity. According to Bergeron (1959), Köppen was one of the first nineteenth century meteorologists to perceive observational evidence of air masses and their baroclinic boundaries, conventionally called fronts. However, it was not until the 1920s and 1930s that the so-called Norwegian air-mass and frontal concepts (Bjerknes, 1918) were firmly established. These ideas live on today in the form of frontal analyses (e.g., warm, cold and occluded fronts) found on operational weather charts of every major meteorological service in both hemispheres, without exception.

Since the 1940s, the broader concept of a baroclinic frontal zone, vice a frontal line, has become an increasingly important theoretical and synoptic consideration in the life history of many important facets of weather systems. In this connection, the term hyperbaroclinic zone (HBZ), after Godson (1951), is most appropriate to describe a restricted area of relatively large values of baroclinicity, without necessarily connoting a zone separating identifiable air masses. Many investigations in the pre-computer era have demonstrated the importance of HBZs to the dynamic and thermodynamic processes and structure of the atmosphere (Bjerknes, 1951; McClain and Danielsen, 1955; Newton, 1958; Palmen, 1951; Palmen and Newton,



*A Dissertation submitted to the Faculty of the Department of Meteorology, Florida State University, Tallahassee, Florida, in partial fulfillment of the requirements for the degree of Doctor of Philosophy.

1951; Reed and Sanders, 1953; Sanders, 1955). A synthesis of theories and examples of development and motion of waves, vortices, jet streams, and cloud and precipitation regimes as a function of baroclinicity may be found in dynamics texts (e.g., Haltiner and Martin [1957] or Hess [1959]) and applied manuals (e.g., Riehl et al. [1952, 1954], the United States Navy [1952] and the United States Weather Bureau [1960]). However, quantitative knowledge of the behavioral characteristics of HBZs on a synoptic hemispheric scale has remained incomplete. This is due to the shortcomings imposed by subjective analysis with its attendant ambiguity in locating and depicting the important HBZs and to the derived, not observed, nature of baroclinicity. The operational convention of specifying only the warm-side boundary of the HBZ (Taljaard et al., 1961) has further detracted from attention to the zone rather than the line.

Attempts at overcoming the frustrations of the manual analysis of HBZ boundaries have been pioneered by the Meteorological Service of Canada (Anderson et al., 1955). Their frontal-contour model, comprising three fronts and four air masses has been used to assist in a quasi-objective approach to frontal analysis. However, the model places undue emphasis on the labeling of air masses and fronts by means of empirically-determined frontal values of various temperature parameters, notably wet-bulb potential temperature. Moreover, the time involved in the subjective manipulations necessary for the objective placement of frontal contours exceeds the human capacity for anything but a regional effort, if operational deadlines are to be met.

The dilemna of real-time urgency in frontal analysis suggests numerical-objective vice manual-subjective or manual-objective analysis

of HBZs. Such an approach has been possible since the availability of high speed digital computers in the middle 1950s, but either was not attempted or was unsuccessfully attempted until the development reported on here.

The earliest and only past effort in numerical-objective HBZ analysis known to this writer[1], a statistical approach, was not successful, apparently because of an over specification of front-associated parameters and criteria for front location and intensity. It is a natural tendency to presume that the utilization of a multiple number of variables, such as pressure, wind, temperature, humidity, and their derivatives, would fare better than any one of them in objectively placing fronts. But, the diverse reactions of each of these parameters to the synoptic and mesoscale processes which affect baroclinicity, as modified by topography, complicates the standardization of locating HBZs by statistical formulae or by dynamical-statistical means. The more recent numerical-objective efforts by the United States Naval Weather Service (Hughes, 1967) and Air Weather Service (United States Air Force, 1965-1968), the Canadian Meteorological Service (Creswick, 1967), and British meteorologists (Kirk, 1965), have taken advantage of the research described in detail here and reported on earlier as preliminary accounts to the meteorological community (Renard and Clarke, 1965a, 1965b, 1966; Clarke and Renard, 1965, 1966a, 1966b; Renard, 1967a, 1967b, 1967c).

---

[1]Correspondence with personnel at the Third Weather Wing, United States Air Force, Offutt Air Force Base, Nebraska, and Travelers Research Center, Hartford, Connecticut; also, a Report Bibliography prepared for the writer by the Defense Documentation Center (1965).

Thus, the middle 1960s found numerical techniques and high-speed computers used to analyze, diagnose, and prognosticate the operationally-usable structure of the atmosphere, from near the surface to stratospheric levels, with one notable exception, namely frontal phenomena. Without philosophizing as to the inherent merits and deficiencies of frontal analysis and prognosis to weather processes (Sawyer, 1964), their importance is evident immediately from the most casual perusal of daily weather maps from the United States (civilian and military) or any other nation. Such charts always include front locations for at least one level in the troposphere.

An example, clearly illustrating the need for unique placement of fronts is shown in Fig. 1. This illustration displays the 0000 GMT 5 March 1964 surface fronts analyzed by sixteen United States and foreign civilian and military weather centers. The non-uniformity of concept, definition, and model are manifested by fronts which cross at angles as much as 90 degrees and differ in position by 300 miles or more when apparently indicating the same HBZ boundary. Such a situation is intolerable to a scientific discipline and, practically speaking, could be disasterous to a civilian or military operation which depended on such analyses for its success. What are the parametric criteria for placing each of the fronts? Are they concerned with temperature and/or temperature gradient, cloud and/or precipitation, vector wind and/or wind shift, pressure gradient and/or pressure tendency? Quantitative answers to these questions do not exist from any of the weather services whose frontal analyses are displayed in Fig. 1. The situation in 1970 differs very little from that in 1964 or 1960 (Jacobs-Haupt, 1963).

In order to improve the matters just described, experiments were begun in 1964 to develop a model for numerically specifying hyperbaroclinic

zones, their boundaries and intensities, with the aim of objectively specifying these phenomena on a real-time operational basis. During the initial phases of the investigation, the decision was made to adopt a definition for the HBZ which is simple and acceptable to theoreticians and synopticians alike. Such a definition is that implied for the frontal zone in the American Meteorological Society's Glossary of Meteorology (Brooks et al., 1959). In essence, the frontal zone is described as a three-dimensional zone or layer of large horizontal density gradient bounded by surfaces (i.e., frontal surfaces) across which this gradient is discontinuous. The intersection of a frontal surface with another identifiable surface or plane (e.g., a constant-pressure surface or the x, p plane) generates a line called the front. Such a definition agrees with that proposed by Taljaard et al. (1961) in their excellent appraisal of the state of frontal analysis in the early 1960s. Theirs is still a very timely estimation. Since the concept stated in the Glossary of Meteorology clearly isolates density gradient, and thus temperature gradient, as the essential front-location parameter, the measure of frontal phenomena and baroclinicity are of the same nature. Therefore, the hyperbaroclinic zone, a bounded region of relatively large baroclinicity, is alternately referred to as a frontal zone and the HBZ boundaries as fronts. However, the term front is not limited only to the warm-side boundary of HBZs as conventionally analyzed in connection with frontal wave cyclones of the middle and high latitudes. Also, at this point, the discontinuity aspect of the frontal-zone definition should be interpreted as a mathematical specification not necessarily substantiated in the real atmosphere due to a limited data network and the scale of analysis.

Fig. 1. Surface fronts at 0000 GMT 5 March 1964, as transcribed from analyses of the following international and national civilian and military weather-analysis centers:

National Meteorological Center, United States Weather Bureau; Central Analysis Office, Meteorological Branch, Department of Transport, Canada; Japanese Meteorological Agency; British Meteorological Office; Zentralamt, Deutscher Wetterdienst; Icelandic Weather Bureau; United States Navy Weather Centrals at Alameda, Guam, and Pearl Harbor; United States Navy Weather Facilities at Argentia, Miami, Norfolk, Quonset Point, San Diego, Sangley Point, and Yokosuka.

The subsequent chapters describe the development, characteristics, and applications of a numerical model for locating and measuring the intensity of real-atmosphere HBZs. Hemispheric, synoptic-scale case studies provide a limited four-dimensional (x, y, p, t) diagnosis of HBZs on a multi-seasonal basis. However, the reader may first wish to peruse Appendix I for a survey of the writer's preliminary experiments in numerical frontal analysis. These first probes, somewhat air-mass oriented and based on wet bulb and equivalent potential temperatures, were not extended due to the difficulties of adequately computing and portraying moisture on a hemispheric scale as well as the artificiality of air-mass labeling. Relegating this section to an appendix signifies the terminal nature of these early experiments. Following these preliminary experiments, research was directed toward a more dynamic approach to numerical HBZ analysis, utilizing virtual potential temperature and its derivatives. The model proposed for general operational use and diagnostic testing is discussed at length in Chapter II. Chapter III illustrates the model by examples derived from hemispheric application in a framework of an existent operational analysis and forecast complex, namely the Fleet Numerical Weather Central, Monterey, California. A more refined scheme for specifying HBZs, featuring high resolution derived from vertical soundings, is presented next (Chapter IV) as a prototype for analysis on the subsynoptic scale. Chapters V-VII return to the operational model appropriate to present-day synoptic-scale analysis (Chapter II) and focus on substudies concerned with the spatial and temporal consistency of numerical HBZ analysis and the relation of these analyses to cloud and vertical motion patterns. Finally, the treatise concludes with a resume' of the investigative results (Chapter VIII).

# CHAPTER II

## HYPERBAROCLINIC-ZONE ANALYSIS: DEVELOPMENT AND CHARACTERISTICS OF A NUMERICAL MODEL

### The Model

The preliminary experiments described in Appendix A, although valuable, merely suggested a continuation of the search for a more universal approach to objective hyperbaroclinic-zone analysis, that is, one void of intimate association with air-mass identification.

The definition of the HBZ, basic to the analysis model whose development is outlined in this chapter, is described in Chapter I. Since the essential parameter is atmospheric baroclinicity, the numerical specification of the HBZ proceeds from the definition of the magnitude of total baroclinicity about a local point, which is given by Saucier (1955) as

$$N = g\left|\nabla \ln \theta^*\right| . \qquad (1)$$

N represents the number of unit solenoids per unit area in a plane determined by the near-vertical three dimensional pressure gradient and a normal to the isolines of virtual potential temperature ($\theta^*$) on a constant pressure surface; g is gravity. Since $\nabla\theta^*$ has mathematical properties similar to $\nabla \ln \theta^*$ while offering greater facility in handling of data, the former is used in the development that follows.

Symbolizing the unit vector normal to the line bounding the HBZ as $\vec{n}_t$, a parameter for locating the line on a constant pressure surface may be defined by

$$DG\theta^*_t \equiv - \nabla|\nabla\theta^*| \cdot \vec{n}_t = - \frac{\partial^2 \theta^*}{\partial n_t^2}. \qquad (2)$$

Thus, $DG\theta^*_t$ is a directional second derivative of $\theta^*$, constrained to lie along $\vec{n}_t$.

With reference to the identity in Eq. 2, the direction implied by $\vec{n}_t$ is unknown initially, as the position and orientation of the front is the quantity being sought. However, since the HBZ tends to follow an isotherm channel, a suitable approximation to $\vec{n}_t$ is given by the unit vector perpendicular to isotherms. Therefore, with a view toward quantitative applications, the HBZ-location parameter on a constant pressure surface is redefined as

$$DG\theta^* \equiv - \nabla|\nabla\theta^*| \cdot \vec{n}_{\theta^*} = - \nabla G\theta^* \cdot \vec{n}_{\theta^*} = - \frac{\partial^2 \theta^*}{\partial n_{\theta^*}^2}, \qquad (3)$$

where $\vec{n}_{\theta^*}$ is a unit vector along $\nabla\theta^*$, and

$$G\theta^* \equiv |\nabla\theta^*| = \partial\theta^*/\partial n_{\theta^*}. \qquad (4)$$

A One-dimensional Schematic Analysis of $DG\theta^*$

A one-dimensional representation of $\theta^*$, $G\theta^*$, and $DG\theta^*$ which simulates the real atmosphere is an aid in describing the synoptic and thermo-physical properties of $DG\theta^*$. Fig. 2 presents continuous schematic profiles of $\theta^*$ and its derivatives oriented along $\nabla\theta^*$ on an isobaric surface. The profiles are slightly asymmetric about location 0. Points 1 and 2 in Fig. 2a are locations of relative maxima in the

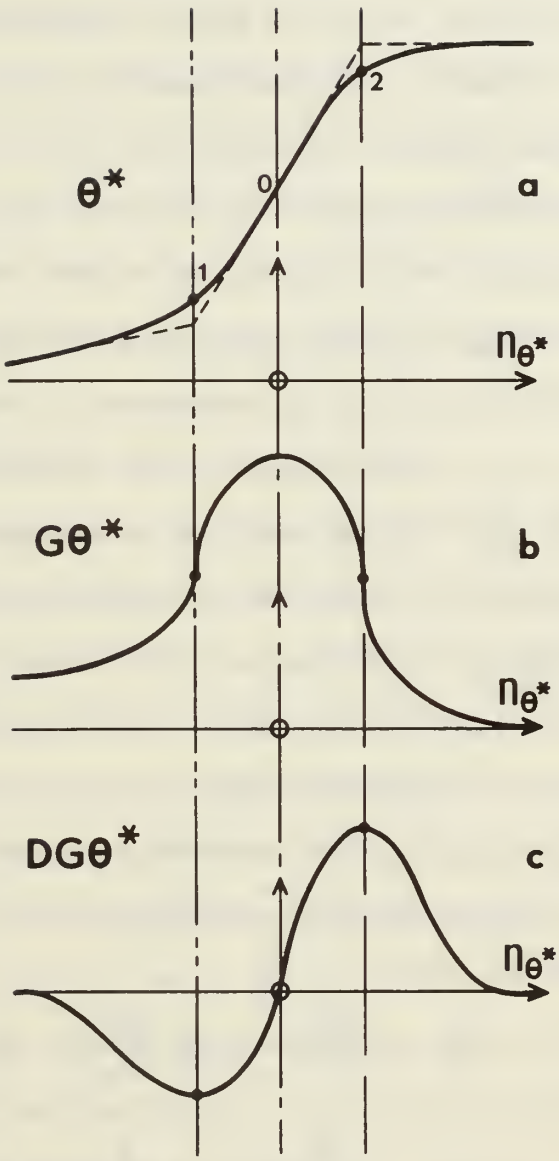


Fig. 2. A continuous schematic profile of θ* and the Gθ* and DGθ* profiles derived from it.

a. θ*; theoretical profile with first-order discontinuity also shown in the vicinity of points 1 and 2 (dashed line).

b. Gθ*, derived from Fig. a.

c. DGθ*, derived from Figs. a and b.

curvature of the θ* profile; theoretically, such points are first-order discontinuities in θ*.

The expression Gθ* is a measure of the baroclinicity (Fig. 2b), which is maximized at location 0 in the θ* profile. The inflection points (1, 2) in Gθ* are suitable boundaries of the zone containing relatively large magnitudes of baroclinicity, i.e., the HBZ. A higher-order derivative of θ* is required to give a clear and quantitative indication of the boundaries of the HBZ. This is shown by the DGθ* profile in Fig. 2c. The maximum and minimum values of DGθ* indicate warm-side and cold-side boundaries of the HBZ, respectively, with the zero point representative of the location of maximum baroclinicity (Fig. 2b). Though magnitude of baroclinicity is not explicitly given by the front-location parameter, DGθ*, a relatively large spatial change in ∇θ* implies the existence of high values of baroclinicity in the associated HBZ. Statistical and synoptic verifications of this relation are cited in this and later chapters.

Physical significance of DGθ* may be seen from the relations of geostrophic thermal wind, $\vec{V}_T$, and the isobaric virtual temperatures, T* and θ*.

$$|\vec{V}_T| \equiv |\frac{\partial \vec{V}g}{\partial z}| = \frac{g}{fT^*} \frac{\partial T^*}{\partial n_{T^*}} = \frac{g}{f} \frac{\partial \ln \theta^*}{\partial n_{\theta^*}} \tag{5}$$

and

$$|\frac{\partial \vec{V}_T}{\partial n_{\theta^*}}| = \frac{g}{f} \frac{\partial^2 \ln \theta^*}{\partial n_{\theta^*}^2}. \tag{6}$$

Therefore, the shear component of the thermal vorticity, given by the shear of the thermal wind in Eq. 6, also exhibits a maximum in magnitude at each of the HBZ boundaries.

## Analysis Characteristics of the Model

In order to demonstrate the effects of numerical differentiation and interpolation, and scale on the location and intensity of HBZs, three hypothetical, but realistic, $\theta^*$ profiles are presented (Fig. 3) and interpreted. The profiles are assumed to be oriented in the direction of $\nabla\theta^*$, here considered to be colinear with the I axis of the grid. Data are specified for whole-numbered grid points only (Table 1), consistent with numerically-analyzed observations. Although the distance between grid points, d, is somewhat arbitrary for the arguments set forth in this chapter, it will be of great practical value for what follows to consider d = 381 km[1].

The temperature scale in Fig. 3 is symbolic only, but as in the real atmosphere, the warm air is shown to be less baroclinic than the cold air in all three cases. The profiles are linear in the warm air but depart slightly from such in the cold air. The hyperbaroclinic zones, separating the coldest from the warmest air, are bounded by break points typical of nature's version of first-order discontinuities on the synoptic scale. These maximum-curvature points in the modeled profiles are labeled as $F_w$ and $F_k$ for boundaries on the warm- and cold-air sides of each of the HBZs, respectively. The profiles are labeled N (narrow), M (medium) and W (wide), descriptive of HBZ widths of one, two, and three mesh lengths, respectively. However, for all three profiles, the HBZ $\Delta\theta^*$ is 10 C. This results in HBZ gradients of 10 C $(381\ \text{km})^{-1}$ for N, 5 C $(381\ \text{km})^{-1}$ for M and 3.3 $(381\ \text{km})^{-1}$ for W.

---

[1] 381 km is the mesh length at 60 deg lat in the FNWC grid representation of the Northern Hemisphere.

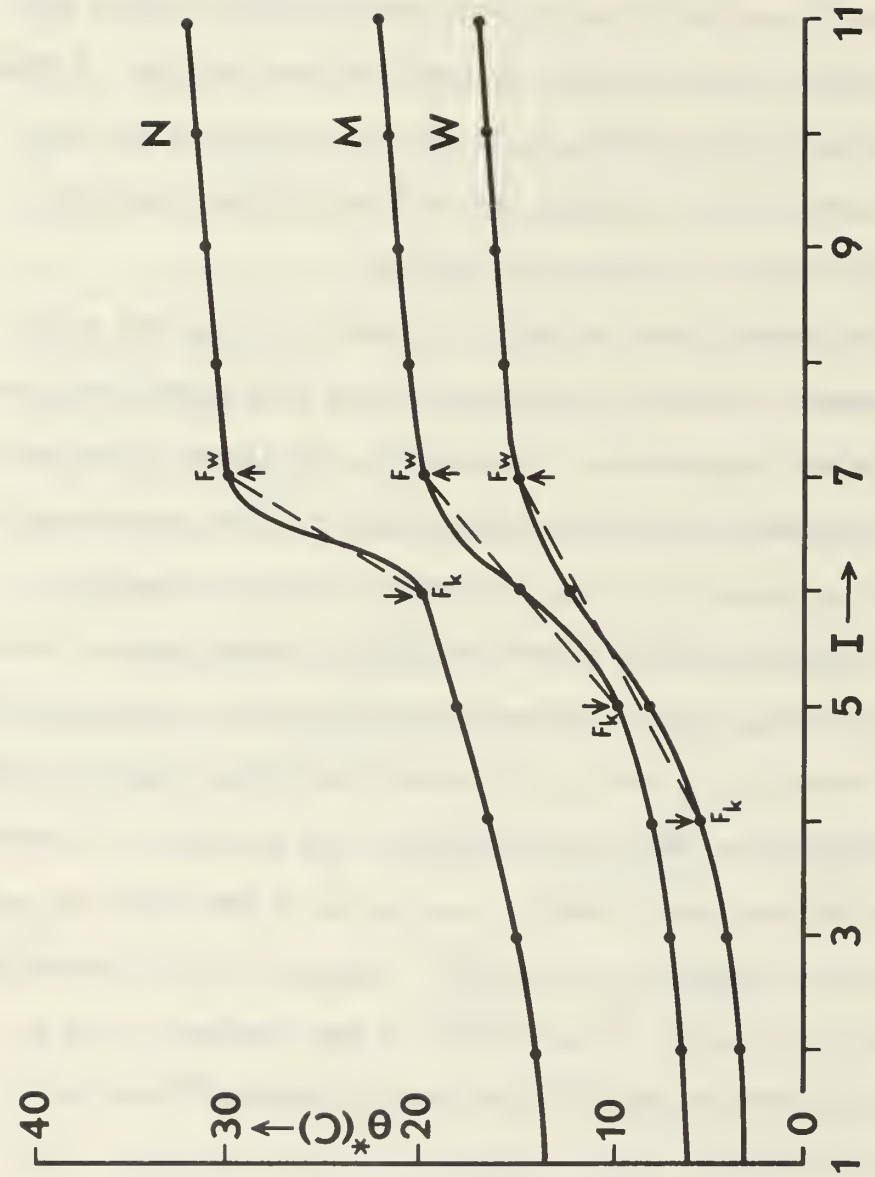


Fig. 3. Modeled profiles of θ* (solid lines), specified as N, M, and W, to identify the included narrow, medium, and wide HBZ widths, respectively, contained between $F_w$ and $F_k$.

The aim of this chapter is to simulate, in a systematic but simple fashion, numerical differentiation and interpolation of temperature data using computations of the type common to meteorological analysis. The modeled thermal data are considered numerically processed grid-point temperatures. Cases of definite physical-synoptic significance are selected for simulation, as, for example, numerical processing in relation to intensity of frontal zones, mesh length, closely adjacent fronts, frontal slopes, and the use of layer vice level in the DG$\theta$* computations.

## The Simulation Experiments

### Frontal-zone Intensity

Variation in HBZ width--First, the $\theta$* data in Fig. 3 are used to generate G$\theta$* values by employing the Lagrangian 3- and 5-point numerical differentiation formulae (Jennings, 1964) for centered differences. For the 3-point computation at the central grid point, $I_o$, the formulation is

$$G\theta^*_o = \frac{\left|(\theta^*_{o+1} - \theta^*_{o-1})\right|}{2d}, \tag{7}$$

while the 5-point $G\theta^*_o$ is given by the following expression:

$$G\theta^*_o = \frac{\left|8\,[\theta^*_{o+1} - \theta^*_{o-1}] - \theta^*_{o+2} + \theta^*_{o-2}\right|}{12d}. \tag{8}$$

G$\theta$* grid-point data are then used to generate the DG$\theta$*s, again using both the 3-point and 5-point numerical differentiations.

In order to show relative magnitudes of frontal parameters in and near the N, M, and W frontal zones, Table 1 lists the grid-point $\theta$*s (from Fig. 3) and the computed values of G$\theta$* and DG$\theta$*. It is to be noted that the magnitudes of G$\theta$* and DG$\theta$* at and between $F_w$ and $F_k$

Table 1. Grid point values of θ* (C), and computed Gθ* (C[100 km]$^{-1}$) and DGθ* (C[100 km]$^{-2}$) at intervals of 1I for the N, M, and W profiles in Fig. 3, both for the 3- and 5-point numerical differentiation schemes. Subsets of DGθ* values indicate interpolated HBZ-boundary locations and their attendant DGθ* maxima and minima (circled numbers). HBZ Δθ* = 10C. $F_w$ ($F_k$) is the position of the warm (cold) boundary of the modeled HBZs.

| N | | | | | | M | | | | | | W | | | | | |
|---|---|---|---|---|---|---|---|---|---|---|---|---|---|---|---|---|---|
| I | θ* | Gθ* | | DGθ* | | I | θ* | Gθ* | | DGθ* | | I | θ* | Gθ* | | DGθ* | |
| | | 3-pt | 5-pt | 3-pt | 5-pt | | | 3-pt | 5-pt | 3-pt | 5-pt | | | 3-pt | 5-pt | 3-pt | 5-pt |
| 13 | 32.55 | | | | | 13 | 22.55 | | | | | 13 | 17.55 | | | | |
| 12 | 32.5 | | | | | 12 | 22.5 | | | | | 12 | 17.5 | | | | |
| 11 | 32. | .13 | .14 | | | 11 | 22. | .13 | .14 | | | 11 | 17. | .13 | .13 | | |
| 10 | 31.5 | .13 | .13 | | | 10 | 21.5 | .13 | .13 | | | 10 | 16.5 | .13 | .13 | | |
| 9 | 31. | .13 | .13 | .00 | -.04 | 9 | 21. | .13 | .13 | .00 | -.03 | 9 | 16. | .13 | .13 | .00 | -.02 |
| 8 | 30.5 | .13 | .08 | +.16 | +.21 | 8 | 20.5 | .13 | .03 | +.08 | +.08 | 8 | 15.5 | .13 | .08 | +.04 | +.03 |
| 7 | 30. | 1.38 | 1.56 | +.17 | +.30($F_w$) | 7 | 20. | .72 | .72 | +.16 | +.23($F_w$) | 7 | 15. | .46 | .44 | +.10 | +.14($F_w$) |
| 6 | 20. | 1.58 | 1.79 | -.12 | -.23($F_k$) | 6 | 15. | 1.31 | 1.47 | +.03 | +.03 | 6 | 12. | .92 | 1.00 | +.06 | +.09 |
| 5 | 18. | .46 | .28 | -.16 | -.22 | 5 | 10. | .92 | .94 | -.12 | -.19($F_k$) | 5 | 8. | .92 | .98 | -.05 | -.08 |
| 4 | 16.5 | .39 | .39 | -.01 | +.04 | 4 | 8. | .39 | .33 | -.09 | -.10 | 4 | 5. | .52 | .51 | -.09 | -.13($F_k$) |
| 3 | 15. | .33 | .34 | -.03 | -.03 | 3 | 7. | .23 | .22 | -.03 | -.02 | 3 | 4. | .20 | .15 | -.05 | -.05 |
| 2 | 14. | .20 | .20 | | | 2 | 6.25 | .13 | .13 | | | 2 | 3.5 | .13 | .13 | | |
| 1 | 13.5 | .07 | .06 | | | 1 | 6.0 | .02 | .02 | | | 1 | 3. | .10 | .10 | | |
| 0 | 13.5 | | | | | 0 | 6.0 | | | | | 0 | 2.75 | | | | |
| -1 | 13.5 | | | | | -1 | 6.0 | | | | | -1 | 2.75 | | | | |
| 8 | | | | +.16 | +.21 | 8 | | | | +.08 | +.08 | 7 | | | | (+.10) | +.14($F_w$) |
| 7.4 | | | | (+.21) | | 7.1 | | | | (+.16) | | 6.7 | | | | | (+.15) |
| 7.3 | | | | | (+.32) | 7.0 | | | | +.16 | (+.23)($F_w$) | 6 | | | | +.06 | +.09 |
| 7 | | | | +.17 | +.30($F_w$) | 6 | | | | +.03 | +.03 | 5 | | | | -.05 | -.08 |
| 6 | | | | -.12 | -.23($F_k$) | 5 | | | | -.12 | -.19($F_k$) | 4.3 | | | | | (-.14) |
| 5.5 | | | | | (-.27) | 4.8 | | | | (-.12) | (-.20) | 4 | | | | (-.09) | -.13($F_k$) |
| 5.4 | | | | (-.17) | | 4 | | | | -.09 | -.10 | | | | | | |
| 5 | | | | -.16 | -.22 | | | | | | | | | | | | |

are similar to those found in frontal zones on the daily operational charts (Chapter III).

The foremost question to which the profiles and tabular data are directed is as follows. Assuming the modeled positions of the HBZ boundaries to be at $F_w$ and $F_k$, where are the frontal positions as located by numerical differentiation and interpolation of the grid-point temperature data? To answer this question, Bessel's central difference polynomial interpolation formula (Jennings, 1964) is utilized to interpolate the location of DG$\theta$* maxima and minima to the nearest .1 mesh length (i.e. about .3 deg lat for d = 381 km). These points are representative of the warm-side boundary (conventional front) and the cold-side boundary of the HBZ, respectively.

Setting DG$\theta$* = y, the formulation for DG$\theta$* is

$$DG\theta^*_{0+s} = y_{0+s} = \frac{y_1+y_0}{2} + B_1(y_1-y_0) + B_2(y_2-y_1+y_{-1}-y_0) + B_3[(y_2-y_1) - 2(y_1-y_0) + (y_0-y_{-1})], \quad (9)$$

where subscripts -1, 0, 1, and 2 indicate grid-point locations and s is the fractional distance between I = 0 and I = 1. The constants, $B_1$, $B_2$, and $B_3$ are functions of s in the form

$$B_1 = s - \frac{1}{2},$$

$$B_2 = \frac{s(s-1)}{2}, \quad (10)$$

and

$$B_3 = \frac{s(s-1)(s-\frac{1}{2})}{6}.$$

Consistent with the number of grid points used in the 5-point numerical differentiation formula (Eq. 8) the interpolation formula (Eq. 9) is truncated with the term which is cubic in s (third degree polynomial).

The numerically-interpolated locations of the HBZ boundaries and their attendant DG$\theta$* values are also shown in Table 1. For example, in the case of the N profile the interpolated frontal-zone boundaries are interpolated to be at 7.4I and 5.4I (7.3I and 5.5I) for the 3-point (5-point) computation with DG$\theta$* values of +0.21 and -0.17 (+0.32 and -0.27), respectively. By comparison, the modeled N-profile data indicate HBZ boundaries at I7 and I6 with DG$\theta$* values of +0.30 and -0.23, respectively.

The following conclusions are pertinent to Table 1:

1. The computed narrow (i.e. strong) frontal zone is broadened most relative to the modeled zone width, both for the 3- and the 5-point differentiation schemes. In fact, the weak frontal zone is foreshortened, not broadened, in the 5-point case.

2. The 3-point differentiation scheme broadens the HBZs more than the 5-point approximation. Specifically, the computed HBZ widths are broadened by the following percentages relative to the modeled zone widths:

| | N | M | W |
|---|---|---|---|
| 3-pt | 100 | 15 | 0 |
| 5-pt | 80 | 10 | -20 |

3. The broadening effect is up to 20 percent greater on the cold-side boundary of the HBZ. It is to be noted that the cold-side boundary borders on the most baroclinic of the two air masses.

4. The maximum grid-point magnitudes of 5-point G$\theta$* values exceed those of the 3-point scheme and may be greater than the values implied in the modeled HBZs of Fig. 3, as noted below for figures extracted from Table 1.

$G\theta^*$ (C[100 km]$^{-1}$)

| HBZ | Modeled | Computed | |
|---|---|---|---|
| | | 5-pt | 3-pt |
| N | 2.63 | 1.79 | 1.58 |
| M | 1.31 | 1.47 | 1.31 |
| W | .87 | 1.00 | .92 |

Hence, the 5-point $G\theta^*$ values are more desirable in order to yield frontal $DG\theta^*$s which clearly outline the HBZs.

5. The maximum $DG\theta^*$ is greater in magnitude than the minimum $DG\theta^*$ for a given HBZ, a consequence of greater baroclinicity in the colder of the two air masses.

Further, note that if the modeled HBZ boundary in Fig. 3 is located between grid points the broadening and magnitude problems are increased. For example, in the case of the N profile, the broadening is quantitatively increased up to nine-tenths of a mesh length by placing the HBZ boundaries at 6.0I and 6.1I while maintaining the $\theta^*$ value at 7.0I. Thus, with a HBZ width of 0.1I in the N case, the broadening percentage increases to 1700 percent for the 5-point differentiation. However, this circumstance is highly unlikely since a HBZ width < 40 km is unrealistic on the scale of present-day observations and analyses. In case of the M and W frontal profiles the HBZs could be reduced to a zone lying between 5.9I and 6.1I and 4.9I and 6.1I, respectively, without a change in grid-point temperature data. This would result in a percentage broadening of 1000 percent and 100 percent, respectively, for the M and W profiles in the 5-point case. However, nonmeteorological $\theta^*$ profiles would result for the M and W cases if the grid-point temperature data remained unchanged.

Variation in HBZ $\Delta\theta^*$--Frontal-zone intensity (i.e. average $\Delta\theta^*$ within the transition zone) is dependent on the change of $\theta^*$ in the zone (i.e. $\Delta\theta^*$) as well as distance ($\Delta n_{\theta^*}$) through which $\Delta\theta^*$ occurs. In order to demonstrate the effect of variations of $\nabla\theta^*$ in the HBZ due to changes in $\Delta\theta^*$, the $\Delta\theta^*$ is reduced to 5C for the N profile only of Fig. 3. This results in a modeled transition-zone gradient equivalent to that of the M profile in Fig. 3. Table 2 shows the $\theta^*$, $G\theta^*$, and $DG\theta^*$ tabulations and broadening effects for the 3- and 5-point differentiations in the same format as Table 1.

The broadening effect on the cold-side is greater than that on the warm-side boundary of the HBZ, an effect similar in kind to the N profile ($\Delta\theta^*$ = 10C) even though the computed $G\theta^*$s and $DG\theta^*$s resemble the W case of Table 1. The overall percentage broadening is about the same as the N case in Fig. 3, namely 110 percent for the 3-point and 70 percent for the 5-point differentiations, again showing the desirability of the latter. In view of these effects, it appears that it is the frontal-zone width more than the magnitude of $\Delta\theta^*$ which fosters significant computational broadening of the HBZ. That is, the real-atmosphere narrow transition zones are broadened relatively more than the wide zones by numerical processing, regardless of the magnitude of $\Delta\theta^*$ across the HBZ.

Both Tables 1 and 2 suggest the insignificance and noisiness of $DG\theta^*$ data outside the HBZ where values generally become $\leq |.05|C(100\ km)^{-2}$ within one mesh length of HBZ boundaries. Also, the zero $DG\theta^*$ values lie half-way between the maximum and minimum values (to the nearest .1 d) for all 5-point cases in Tables 1 and 2. These facts provide guidance in the development of an operational $DG\theta^*$ product, as discussed in Chapter III.

Table 2. Grid point values of $\theta^*$ (C), and computed $G\theta^*$ (C[100 km]$^{-1}$) and $DG\theta^*$ (C[100 km]$^{-2}$) at intervals of 1I for the N profile in Fig. 3, for the 3- and 5-point numerical differentiation schemes. Subsets of $DG\theta^*$ values indicate interpolated HBZ-boundary locations and their attendant $DG\theta^*$ maxima and minima (circled numbers). HBZ $\Delta\theta^* = 5C$. $F_w$ ($F_k$) is the position of the warm (cold) boundary of the modeled HBZs.

| I | $\theta^*$ | $G\theta^*$ | | $DG\theta^*$ | |
|---|---|---|---|---|---|
| | | 3-pt | 5-pt | 3-pt | 5-pt |
| 13 | 32.55 | | | | |
| 12 | 32.5 | | | | |
| 11 | 32. | .13 | .14 | | |
| 10 | 31.5 | .13 | .13 | | |
| 9 | 31. | .13 | .13 | .00 | -.02 |
| 8 | 30.5 | .13 | .03 | +.08 | +.10 |
| 7 | 30. | .72 | .79 | +.10 | +.17$F_w$ |
| 6 | 25. | .92 | 1.02 | -.03 | -.08$F_k$ |
| 5 | 23. | .46 | .39 | -.07 | -.10 |
| 4 | 21.5 | .39 | .39 | -.02 | +.00 |
| 3 | 20. | .33 | .34 | -.03 | -.03 |
| 2 | 19. | .20 | .20 | | |
| 1 | 18.5 | .07 | .06 | | |
| 0 | 18.5 | | | | |
| -1 | 18.5 | | | | |
| | | | | | |
| 8 | | | | +.08 | +.10 |
| 7.2 | | | | (+.11) | |
| 7.1 | | | | | (+.17) |
| 7 | | | | +.10 | +.17$F_w$ |
| 6 | | | | -.03 | -.08$F_k$ |
| 5.4 | | | | | (-.11) |
| 5.1 | | | | (-.07) | |
| 5.0 | | | | -.07 | -.10 |

Variation in Mesh Length

In order to demonstrate the increase of resolution in locating fronts with a decrease in mesh length, the N and M profiles of Fig. 3 were considered in connection with a doubling of the number of grid points. Linear interpolation was used to obtain the $\theta^*$ values at the positions intermediate to the whole numbered grid points in Fig. 3 (i.e., at $I_{3.5}$ $I_{4.5}$ $I_{5.5}$, etc.) with slight exception in the M case. Here, a deviation from linearity was employed to show maximum baroclinicity at the geometric center of the HBZ. The 5-point differentiation scheme and $\Delta\theta^* = 10C$ are common to the two cases computed.

N Case--Table 3 gives the pertinent information on this case. The positioning of the HBZ boundaries is precise, hence the broadening effect is zero compared to 80 percent broadening with data at whole-numbered grid points only. The maximum $G\theta^*$ value has increased by almost 70 percent compared to the N case in Table 1 with $G\theta^*$ exceeding the model value of 2.63 C $(100 \text{ km})^{-1}$; the associated $DG\theta^*$s have tripled, a desirable result for quantitative specification of the HBZ boundaries.

M Case--Table 3 also gives the details on the M case. Much like the N case the positioning is excellent, with the HBZ foreshortened by two-tenths mesh length (10 percent) compared to the modeled width, mostly due to conditions on the cold-side boundary. Again, magnitudes of $G\theta^*$ and $DG\theta^*$ have increased compared to their counterparts in Table 1.

The obvious conclusion is that a mesh-length reduction resolves the computed position and intensity of the HBZ. Any nominal foreshortening due to numerical processing is not only tolerable but desirable due to the smoothing inherent in generating the data at grid points from the reported observations.

Table 3. Grid point values of $\theta^*$ (C), and computed $G\theta^*$ (C[100 km]$^{-1}$) and $DG\theta^*$ (C[100 km]$^{-2}$) at intervals of .5I for the N and M profiles in Fig. 3, for the 5-point numerical differentiation scheme only. Subsets of $DG\theta^*$ values indicate interpolated HBZ-boundary locations and their attendant $DG\theta^*$ maxima and minima (circled numbers). HBZ $\Delta\theta^* = 10C$. $F_w$ ($F_k$) is the position of the warm (cold) boundary of the modeled HBZs.

| N | | | | M | | | |
|---|---|---|---|---|---|---|---|
| I | $\theta^*$ | $G\theta^*$ | $DG\theta^*$ | I | $\theta^*$ | $G\theta^*$ | $DG\theta^*$ |
| 9. | 31. | | | 9. | 21. | | |
| 8.5 | 30.75 | | | 8.5 | 20.75 | | |
| 8. | 30.5 | .14 | -.08 | 8. | 20.5 | .14 | -.04 |
| 7.5 | 30.25 | .08 | +.32 | 7.5 | 20.25 | .04 | +.12 |
| 7. | 30. | 1.38 | $+.96F_w$ | 7. | 20. | .62 | $+.40F_w$ |
| 6.5 | 25. | 3.00 | +.08 | 6.5 | 17.8 | 1.40 | +.28 |
| 6. | 20. | 1.58 | $-.88F_k$ | 6. | 15. | 1.52 | -.04 |
| 5.5 | 19. | .36 | -.56 | 5.5 | 12.2 | 1.36 | -.20 |
| 5. | 18. | .46 | +.04 | 5. | 10. | .82 | $-.24F_k$ |
| 4.5 | 17.25 | .38 | -.04 | 4.5 | 9. | .50 | -.08 |
| 4. | 16.5 | .40 | +.01 | 4. | 8. | .40 | -.08 |
| 3.5 | 15.75 | | | 3.5 | 7.5 | .24 | -.04 |
| 3. | 15. | | | 3. | 7. | .24 | -.01 |
| | | | | 2.5 | 6.62 | | |
| | | | | 2. | 6.25 | | |
| 7 | | | (+.96)$F_w$ | 7 | | | (+.40)$F_w$ |
| 6.5 | | | +.08 | 6.5 | | | +.28 |
| 6 | | | (-.88)$F_k$ | 6 | | | -.04 |
| | | | | 5.5 | | | -.20 |
| | | | | 5.2 | | | (-.28) |
| | | | | 5 | | | $-.24F_k$ |

Closely Adjacent Fronts

A typical occurrence is that which may be described as closely adjacent fronts. Operationally, the fronts are referred to as primary and secondary; the former designates the most equatorward of the two fronts. Usually both frontal zones are of the cold-front variety and the HBZ $\nabla\theta^*$ associated with the secondary is generally weaker than that of the primary.

Two examples are given to illustrate this case. (1) A combination of N and M profiles with an intervening subbaroclinic zone or air mass of one-mesh length dimension; appreciable baroclinicity occurs in the air separating the N and M transition zones. (2) Same as (1) except an intervening air mass of two mesh lengths.

Table 4 illustrates the multiple-front problem with values of $G\theta^*$ and $DG\theta^*$.

One-mesh air mass--In the one-mesh air-mass case the broadening effects noted with N and M profiles (Table 1) are reduced. In other words, the N or primary frontal zone shows 40 percent vice 80 percent broadening and the k-side is more accurately positioned than the w-side, compared to the uncomplicated profiles in Fig. 3. The M or secondary frontal zone is foreshortened by 40 percent (vice 10 percent broadening in Table 1) with the k-side again placed most accurately. The secondary, especially its w-boundary, behaves as a very weak front here.

When viewing the intensities, the w-boundary of the primary is similar to profile N in Table 1, while the k-boundary is reduced in magnitude. The w boundary of the secondary is close to the magnitude of the noise level criterion described earlier, hence the secondary is

Table 4. Grid point values of θ* (C), and computed Gθ* (C[100 km]$^{-1}$) and DGθ* (C[100 km]$^{-2}$) at intervals of 1I for the multiple-front case with air-mass dimensions of one and two mesh lengths. The primary (secondary) front is represented by the N (M) HBZ profile in Fig. 3; 5-point differentiation scheme only. Subsets of DGθ* values indicate interpolated HBZ-boundary locations and their attendant DGθ* maxima and minima (circled numbers). HBZ Δθ* = 10C. $F_w$ ($F_k$) is the position of the warm (cold) boundary of the modeled HBZs.

| | 1-Mesh Air Mass | | | | 2-Mesh Air Mass | | |
|---|---|---|---|---|---|---|---|
| I | θ* | Gθ* | DGθ* | I | θ* | Gθ* | DGθ* |
| 13 | 32.55 | | | 13 | 32.55 | | |
| 12 | 32.5 | | | 12 | 32.5 | | |
| 11 | 32. | .14 | | 11 | 32. | .14 | |
| 10 | 31.5 | .13 | | 10 | 31.5 | .13 | |
| 9 | 31. | .13 | -.04 | 9 | 31. | .13 | -.04 |
| 8 | 30.5 | .08 | +.21 | 8 | 30.5 | .08 | +.21 |
| 7 | 30. | 1.56 | +2.8$F_w$ | 7 | 30. | 1.56 | +.30$F_w$ |
| 6 | 20. | 1.72 | -.17$F_k$ | 6 | 20. | 1.79 | -.26$F_k$ |
| 5 | 18. | .74 | -.03$F_w$ | 5 | 18. | .21 | -.17 |
| 4 | 13. | 1.46 | +.04 | 4 | 16.5 | .84 | +.24$F_w$ |
| 3 | 8. | .79 | -.21$F_k$ | 3 | 11.5 | 1.46 | +.01 |
| 2 | 7. | .15 | -.08 | 2 | 6.5 | .94 | -.18$F_k$ |
| 1 | 6.25 | .13 | -.01 | 1 | 4.5 | .33 | -.10 |
| 0 | 6. | .02 | | 0 | 3.5 | .21 | -.01 |
| -1 | 6. | .01 | | -1 | 2.75 | .20 | |
| -2 | 6. | | | -2 | 2. | .16 | |
| 8 | | | +.21 | 8 | | | +.21 |
| 7.3 | | | (+.30) | 7.3 | | | (+.32) |
| 7 | | | +.28$F_w$ | 7 | | | +.30$F_w$ |
| 6 | | | -.17$F_k$ | 6 | | | -.26$F_k$ |
| 5.9 | | | (-.17) | 5.7 | | | (-.28) |
| 5 | | | -.03$F_w$ | 5 | | | -.17 |
| 4.2 | | | (+.05) | 4 | | | (+.24)$F_w$ |
| 4 | | | +.04 | 3 | | | +.01 |
| 3 | | | (-.21)$F_k$ | 2 | | | (-.18)$F_k$ |

poorly resolved. However, the secondary's k-boundary is well defined in magnitude.

It should be noted that a one-mesh air-mass distance is not very realistic. Further, as in the simple structures in Fig. 3, the numerical processing effect causes all HBZ widths to approach a medial value. The relatively narrow frontal zones broaden, the wide ones tend to foreshorten.

Two-mesh air mass--When the air-mass zone is widened to two mesh lengths both the primary and secondary zones behave as if the other were not present. In the two mesh case, the primary HBZ is broadened by 60 percent vice 80 percent while magnitudes are approximately the same as those of the N profile in Table 1. The secondary front is precisely located and magnitudes agree closely with the simple M profile in Table 1.

It is obvious from this experiment that the position and intensity of each of the HBZs become increasingly independent as the subbaroclinic zone separating them widens.

## Vertical Slope of HBZ Boundaries

What is the relationship of the slope of the HBZ boundaries and the vertical variation of HBZ widths as caused by numerical processing? There are two cases of interest: transition-zone baroclinicity weakens with increasing height; and transition-zone baroclinicity intensifies with increasing height. These are applied to the simple profiles (N, M, W) shown in Fig. 3. The frontal-zone intensity is a function of the width only.

HBZ weakens with increasing height--Fig. 4a illustrates the situation for a modeled warm-boundary slope of approximately 1/240, with frontal-zone characteristics changing from N to M to W from 1000 to 850 to 700 mb, respectively. This results in an associated cold-boundary slope of 1/480. The 1000 to 700 mb warm-boundary slope, determined from numerically-computed data, is 1/312, which is a 23 percent reduction from the modeled slope. At the cold boundary the average slope increases relative to the hypothetical slope by 26 percent (from 1/480 to 1/384) in the layer 1000 to 700 mb.

The computed transition-zone widths, in comparison with the modeled values, range from greater (i.e. broadening) at 1000 mb to less (i.e. foreshortening) at 700 mb. The overall effect is that of reducing the range of HBZ widths relative to the model values. Boundary values of $DG\theta^*$ decrease with height consistent with the vertical gradient of transition-zone baroclinicity.

HBZ intensifies with increasing height--Fig. 4b illustrates the case of the frontal intensity changing from W to M to N with increasing height in the layer 1000 to 700 mb. Again, 1/240 is taken as the slope of the warm-air edge of the HBZ; the computed value is 1/168. The modeled cold-side boundary of the HBZ is constrained to be vertical with the computed slopes ranging from 1/120 in the low layer to 1/72 in the upper layer. Thus, both the broadening effect and magnitude of $DG\theta^*$ maxima increase with increasing height.

## Use of Layer-mean Temperature, $\bar{\theta}^*$, in the $DG\theta^*$ Analysis

Low-troposphere mean temperature (i.e. isobaric-layer thickness) fields enjoy widespread use for locating fronts operationally. Here,

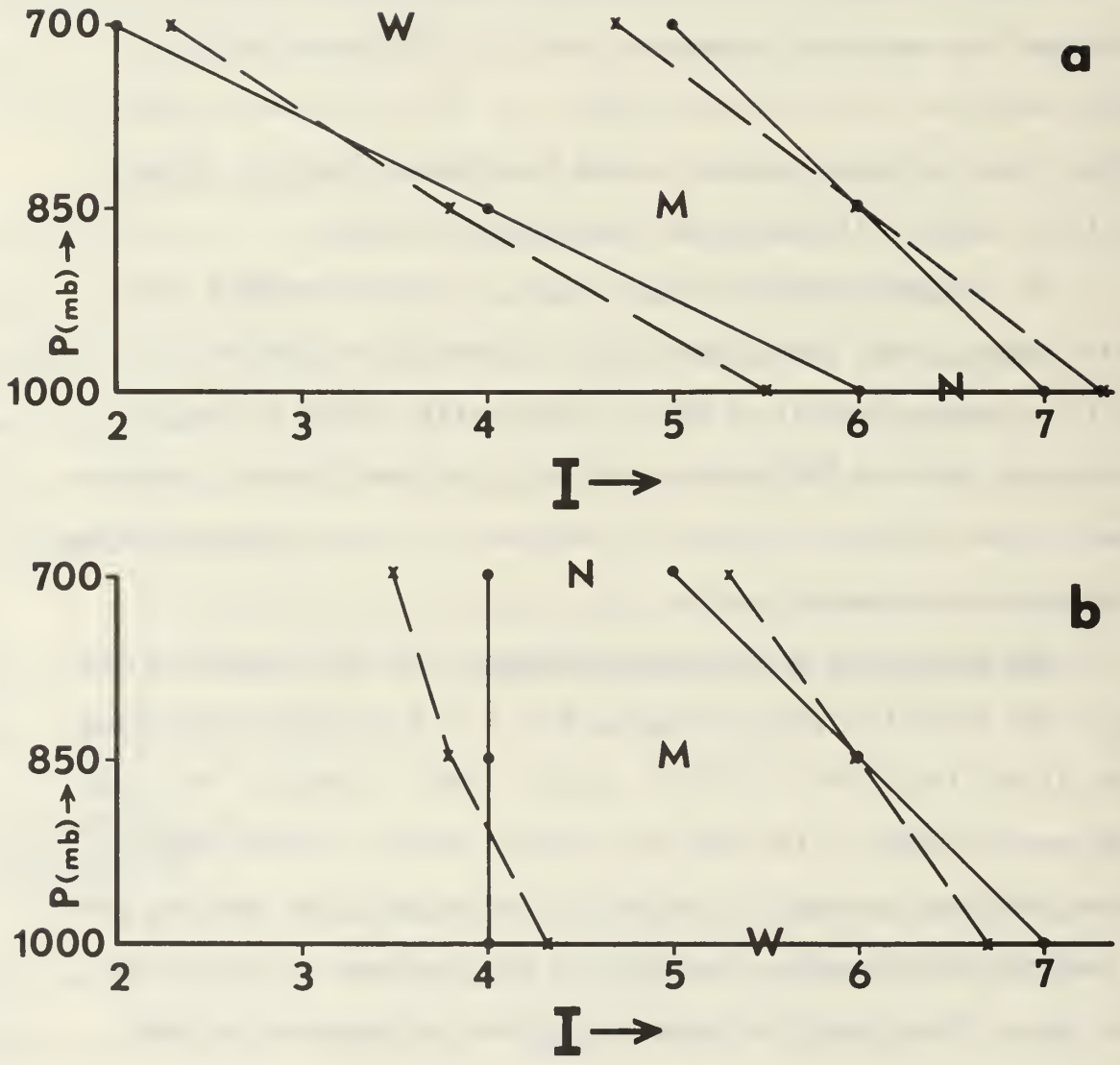


Fig. 4. Numerically-computed HBZ boundaries (dashed lines) in relation to the modeled boundaries (solid lines); HBZ $\Delta\theta^*$ = 10 C.

a. Slope of modeled warm-side boundary: 1/240; width of HBZ increases with height

b. Slope as in a; width of HBZ decreases with height

typical 1000/700 mb mean-layer temperature ($\bar{\theta}^*$) profiles are generated from information in Fig. 3 and reasonable vertical slopes. Only the 5-point derivative scheme is used. The following cases are considered for HBZ slopes of 1/120 and 1/240: (1) 1000 and 700 mb --N-type HBZs both levels; (2) 1000 mb --N-type HBZ, 700 mb --M-type HBZ; and (3) 1000 mb --M-type HBZ, 700 mb --N-type HBZ.

$\bar{\theta}^*$, at each grid point, is obtained as an arithmetic average of the 1000- and 700-mb information where the appropriate 700-mb profile (N or M) is displaced one (two) mesh length(s) toward the cold air for the 1/120 (1/240) slope case, respectively. In addition, 3C to 8C are added to the $\theta^*$ values at 700 mb in order to simulate the normal increase of $\theta^*$ with height, with the higher (lower) temperatures used in the warm (cold) air mass. The addition is made in such a way as to preserve the transition zone $\nabla\theta^*$ at each isobaric level. Such a manipulation of the data agrees with the observable result that the cold air is both more unstable and baroclinic than the warm air in the lower part of the troposphere. Table 5 shows $\bar{\theta}^*$, $G\bar{\theta}^*$, $DG\bar{\theta}^*$, and interpolated HBZ boundaries similar to previous sections.

N-type, both at 1000 and 700 mb; slope: 1/120--This case simulates a relatively strong cold front with steep slope. The numerical positioning of the HBZ boundary is exact, resembling the M profile, single level, while the magnitudes of $DG\bar{\theta}^*$ are intermediate to those for N and M at a single level (Table 1). The HBZ width for $\bar{\theta}^*$ is the distance from the 1000 mb warm-side to the 700 mb cold-side HBZ boundary, thus essentially doubling the hypothetical zone width compared to either 1000 or 700 mb.

Table 5. Grid point values of 1000/700 mb $\bar{\theta}$*, and computed $G\bar{\theta}$* (C[100 km]$^{-1}$) and $DG\bar{\theta}$* (C[100 km]$^{-2}$) at intervals of 1I for N, M, and W profile data derived from Fig. 3 and frontal slopes of 1/120 and 1/240; 5-point differentiation scheme only. Subsets of $DG\bar{\theta}$* values indicate interpolated HBZ-boundary locations and their attendant $DG\bar{\theta}$* maxima and minima (circled numbers). HBZ $\Delta\bar{\theta}$* = 10C. $F_w$ ($F_k$) is the position of the warm (cold) boundary of the modeled HBZs.

| $N^{1000}_{700}$; Slope: 1/120 | | | | $N^{1000}_{700}$; Slope: 1/240 | | | | $N1000_{M700}$; Slope: 1/120 | | | |
|---|---|---|---|---|---|---|---|---|---|---|---|
| I | $\bar{\theta}$* | $G\bar{\theta}$* | $DG\bar{\theta}$* | I | $\bar{\theta}$* | $G\bar{\theta}$* | $DG\bar{\theta}$* | I | $\bar{\theta}$* | $G\bar{\theta}$* | $DG\bar{\theta}$* |
| 13 | 36.8 | | | | 36.9 | | | | 36.65 | | |
| 12 | 36.7 | | | | 36.8 | | | | 36.65 | | |
| 11 | 36.2 | .16 | | | 36.5 | .10 | | | 36.5 | .12 | |
| 10 | 35.5 | .20 | | | 36.0 | .18 | | | 35.75 | .20 | |
| 9 | 34.7 | .20 | -.04 | | 35.2 | .20 | -.04 | | 35.0 | .24 | -.03 |
| 8 | 34.0 | .09 | +.08 | | 34.5 | .07 | +.11 | | 34.0 | .13 | +.09 |
| 7 | 33.2 | .85 | $+.27F_{w1}$ | | 33.8 | .92 | $+.14F_{w1}$ | | 33.25 | .89 | $+.20F_{w1}$ |
| 6 | 27.5 | 1.73 | $+.03F_{k1}F_{w7}$ | | 28.2 | .97 | $-.01F_{k1}$ | | 27.5 | 1.33 | $-.02F_{k1}F_{w7}$ |
| 5 | 21.5 | 1.06 | $-.22F_{k7}$ | | 26.5 | .97 | $+.03F_{w7}$ | | 24.0 | .86 | -.10 |
| 4 | 19.5 | .43 | -.08 | | 20.8 | 1.11 | $-.09F_{k7}$ | | 20.75 | .70 | $-.06F_{k7}$ |
| 3 | 17.7 | .39 | -.04 | | 18.8 | .39 | -.12 | | 18.75 | .41 | -.06 |
| 2 | 16.5 | .29 | | | 17.2 | .34 | -.01 | | 17.5 | .24 | -.00 |
| 1 | 15.5 | .17 | | | 16.2 | .22 | -.03 | | 16.87 | .09 | |
| 0 | 15.2 | | | | 15.5 | .13 | | | 16.75 | .01 | |
| -1 | 15.0 | | | | 15.2 | .06 | | | 16.75 | | |

| | | | | | | | | | | | |
|---|---|---|---|---|---|---|---|---|---|---|---|
| | | | | 8 | | +.11 | | | | | |
| 7 | | | (+.27)$F_{w1}$ | 7.3 | | (+.15) | | 7 | | | (+.20)$F_{w1}$ |
| 6 | | | $+.03F_{k1}F_{w7}$ | 7 | | $+.14F_{w1}$ | | 6 | | | $-.02F_{k1}F_{w7}$ |
| 5 | | | (-.22)$F_{k7}$ | 6 | | $-.01F_{k1}$ | | 5 | | | (-.10) |
| | | | | 5 | | $+.03F_{w7}$ | | 4 | | | $-.06F_{k7}$ |
| | | | | 4 | | $-.09F_{k7}$ | | 3.1 | | | (-.06) |
| | | | | 3.2 | | (-.12) | | 3 | | | -.06 |

| N1000 M700 ; Slope: 1/240 | | | | M1000 N700 ; Slope: 1/120 | | | | M1000 N700 ; Slope: 1/240 | | | |
|---|---|---|---|---|---|---|---|---|---|---|---|
| I | $\bar{\theta}$* | G$\bar{\theta}$* | DG$\bar{\theta}$* | I | $\bar{\theta}$* | G$\bar{\theta}$* | DG$\bar{\theta}$* | I | $\bar{\theta}$* | G$\bar{\theta}$* | DG$\bar{\theta}$* |
| 13 | 36.65 | | | | | | | | | | |
| 12 | 36.65 | | | | 36.52 | | | | 36.52 | | |
| 11 | 36.62 | .04 | | | 36.5 | | | | 36.52 | | |
| 10 | 36.25 | .15 | | | 35.75 | .21 | | | 36.25 | .15 | |
| 9 | 35.5 | .24 | -.02 | | 35.0 | .23 | | | 35.5 | .25 | |
| 8 | 34.5 | .13 | +.10 | | 34.0 | .18 | +.00 | | 34.5 | .19 | +.03 |
| 7 | 33.75 | .89 | +.15$F_{w1}$ | | 33.25 | .42 | + .22$F_{w1}$ | | 33.75 | .48 | +.09$F_{w1}$ |
| 6 | 28.25 | 1.02 | -.07$F_{k1}$ | | 30.0 | 1.58 | +.16$F_{w7}$ | | 30.75 | .81 | +.13 |
| 5 | 26.5 | .58 | -.01$F_{w7}$ | | 22.5 | 1.38 | -.19$F_{k1,7}$ | | 27.5 | 1.31 | +.05$F_{k1}F_{w7}$ |
| 4 | 23.25 | .92 | +.03 | | 20.25 | .47 | -.16 | | 21.5 | 1.08 | -.16$F_{k7}$ |
| 3 | 20.0 | .67 | -.09$F_{k7}$ | | 18.25 | .31 | -.02 | | 19.75 | .33 | -.12 |
| 2 | 18.25 | .34 | -.07 | | 17.75 | .19 | | | 18.37 | .29 | +.00 |
| 1 | 17.25 | .17 | -.04 | | 16.75 | .18 | | | 17.5 | .21 | |
| 0 | 16.87 | .05 | | | 16.5 | | | | 16.75 | .13 | |
| -1 | 16.75 | .01 | | | 16.5 | | | | 16.5 | | |

| | | | | | | | |
|---|---|---|---|---|---|---|---|
| 8 | +.10 | | | | | | |
| 7.2 | (+.15) | 7 | +.22$F_{w1}$ | 7 | +.09$F_{w1}$ | | |
| 7 | +.15$F_{w1}$ | 6.7 | (+.23) | 6 | (+.13) | | |
| 6 | -.07$F_{k1}$ | 6 | +.16$F_{w7}$ | 5 | +.05$F_{k1}F_{w7}$ | | |
| 5.8 | (-.07) | 5 | -.19$F_{k1,7}$ | 4 | -.16$F_{k7}$ | | |
| 5 | -.01$F_{w7}$ | 4.7 | (-.21) | 3.8 | (-.17) | | |
| 4.1 | (+.03) | | | | | | |
| 4 | +.03 | | | | | | |
| 3 | -.09$F_{k7}$ | | | | | | |
| 2.8 | (-.10) | | | | | | |

The nature of the vertical slope is such as to give the effect of an M case in both frontal intensity and width since the superposition of $F_k$ 1000 and $F_w$ 700 tends to obliterate the identity of each of these HBZ boundaries when using the mean temperature field.

N-type both at 1000 and 700 mb; slope: 1/240--Positioning is poor, with the numerical 1000 mb front displaced by one-third mesh length toward the warm air and the computed 700 mb cold-side HBZ boundary extended back into the cold air by eight-tenths mesh length, a 36 percent increase over the modeled HBZ width. Magnitudes of $DG\bar{\theta}^*$ are reduced to those of the W category, but the broadening is typical of the N category (Table 1), partly due to the greater geometric separation between the 1000 mb warm-side and 700 mb cold-side of the HBZ compared to the 1/120 slope case.

For further slope reduction the minor $DG\bar{\theta}^*$ minima and maxima, only evident as noise level values at I6 and I5 in Table 5, become stronger, until two separate and significant HBZs, $F_w$1000 to $F_k$1000 and $F_w$700 to $F_k$700, result. Limiting such occurrences is the fact that in the real atmosphere, the N-type fronts have large slope (i.e. > 1/120).

1000 mb -- N-type; 700 mb -- M-type; slope: 1/120--Position and intensity of the warm-side boundary of the HBZ behaves as the M type but the cold-side boundary, $F_k$700, appears as a doublet with small magnitudes in each case. The cold boundary complexity results from the superposition of a strong $F_k$1000 and a moderate $F_w$700 front.

1000 mb -- N-type; 700 mb -- M-type; slope: 1/240--In this case, due to increased separation of the HBZs at each level, the 1000 mb and 700 mb frontal zones manifest themselves as separate entities. With

further reduction in slope the $F_k1000$ and $F_w700$ boundaries become increasingly distinct. In this case, the $F_w700$ value of +0.03 may be disregarded as noise.

1000 mb -- M-type; 700 mb -- N-type; slope: 1/120--Some rather unexpected results show up for this case. The warm boundary is foreshortened, whereas a broadening effect occurs at the cold boundary. Magnitudes are typical of the M case (Table 1). Apparently, the $F_w700$ position is the cause of the peculiar positioning of the 1000 mb front giving the properties of the W profile to the warm boundary, while N properties are noted at the rear boundary where $F_k1000$ and $F_k700$ are superimposed.

1000 mb -- M-type; 700 mb -- N-type; slope: 1/240--Comment is similar to that immediately above with the added feature of a more intense cold-side HBZ boundary compared to the warm-side.

Summary of the 1000/700 mb layer simulation--Use of $\bar{\theta}^*$ vice $\theta^*$ appears to offer advantages for the front-location model. The broadening effect at the HBZ warm-air edge is reduced, hence this entity is more accurately located by numerical means. Although $DG\bar{\theta}^*$ values are less than $DG\theta^*$ for similar transition zones, the magnitudes remain well above noise-level values. With a view toward operational analysis of $DG\bar{\theta}^*$, it is not too serious that the cold-side boundary locations are complex or poorly located due to the smearing inherent in the thickness model since, by convention, only the warm edges of frontal zones are portrayed on the surface or near-surface isobaric charts.

The occurrence of fronts intensifying with height tends to produce foreshortening (Table 5) of the HBZ, which helps to balance the broadening effect due to sparse data.

General Conclusions

The general conclusions concerning the accuracy of numerical HBZ analysis as derived from experimentation with the profiles in Fig. 3, are as follows:

1. Use of the Lagrangian 5-point vice the 3-point numerical differentiation formula results in the most accurate placement and intensity of the HBZ.

2. There is a tendency toward uniform HBZ widths in the numerical analysis of DG$\theta$*, that is, the narrower zones are widened, the wider zones are narrowed. Stated another way, broadening of the HBZ is more of a function of scale than of degree of baroclinicity in the zone.

3. The most intense or sharply-focused HBZ boundary is the warm-side (i.e., the conventional front), just as in the actual atmosphere, a result of the relatively smaller amount of baroclinicity in the warm compared to the cold air.

4. Although there is a definite tendency toward an unreal uniformity of computed transition-zone widths, there is difficulty in devising an empirical correction as a function of the magnitude of the DG$\theta$* maximum since, by itself, frontal intensity ($\nabla\theta$*) is not a good indicator of the numerically-derived width. Rather, it is the true frontal-zone width which is a good indicator of the broadening effect, but true width is not known. However, it is apparent that the frontal zones with relatively large thermal gradients are most likely to be broadened but the weaker-gradient zones may be broadened or foreshortened due to numerical processing.

5. Overall, the $\bar{\theta}^*$ model is more desirable than the $\theta^*$ model since the effect of using a mean temperature biases the front-location properties toward those of the wide and weak-zone variety and this reduces the broadening effect. However, when using $\bar{\theta}^*$, the cold boundary of the lower-level frontal zone cannot be located. This is also true, to a large degree, for the cold boundary of frontal zones at the upper level of the layer.

6. Closely adjacent frontal zones are likely to be misplaced. In that case, foreshortening and weakening of the conventional boundary of the secondary is a likely effect.

7. Reduction of mesh size aids in resolving the true location and intensity of HBZs. Any tendency toward foreshortening of the HBZ, as mesh size is reduced, is also regarded as favorable considering the smoothing inherent in data processing and the relative sparsity of data.

8. The vertical variation of HBZ intensity, in terms of the zone's width, contributes toward uniformity of widths and vertical slopes of the HBZs.

It should be emphasized that the general analysis characteristics of the DG$\theta^*$ model presented in this chapter were reduced from a relatively simple set of temperature profiles and a controlled simulation experiment. The real atmosphere presents considerably greater complexity in temperature distributions with a wide range of concurrent conditions of frontal-zone intensity, width, slope, and contiguity. Thus, it is logical to consider next a two-dimensional application of the DG$\theta^*$ numerical analysis scheme to a hemispheric portion of the real atmosphere.

# CHAPTER III

## AN OPERATIONAL APPLICATION OF THE HYPERBAROCLINIC-ZONE ANALYSIS MODEL

Chapter II summarized the development of a numerical analysis model which has potential use in identifying, locating, and diagnosing HBZs in real time. Insight was also given on the effects of scale and numerical differentiation and interpolation on the computed values of baroclinicity and zones of hyperbaroclinicity. To this point in the presentation, neither operational merits and deficiencies of the $DG\theta^*$ analysis nor the effects of numerical data processing on the scheme have been considered. Thus, it became desirable to program the $DG\theta^*$ analysis scheme for use in a computer-oriented weather central with international responsibility. Such an environment, and the one most accessible to the physical location of the subject research, is that of the United States Navy's Fleet Numerical Weather Central, Monterey, California (FNWC). There follows a discussion of the FNWC automatic data processing program and examples of two-dimensional $DG\theta^*$ analyses as performed in that framework. Since field use is directed toward the analysis of the conventional front, numerical-objective and manual-subjective versions of frontal analyses are discussed in this and later chapters.

## Data-Processing Framework for the Operational DGθ* Analysis

Germane to the research on hyperbaroclinic zones is the FNWC data processing framework in which the DGθ* analysis is performed. Holl, et al. (1963, 1965) have developed a so-called mass structure model for numerically processing meteorological data in a physically consistent manner. The model is used currently by FNWC (Hughes, 1967). The features of the model, which relate directly to a comprehension of the peculiarities of the analysis of baroclinicity, are described below.

The data used as input to the DGθ* program are those objectively analyzed by FNWC from a Northern Hemisphere synoptic-time coverage of more than 4000 surface and 500 radiosonde observation stations. These data are processed at 12-hour intervals to produce objective analyses of sea-level pressure and height and temperature of all mandatory pressure levels up to 200 mb, as well as dew-point depressions at terrain level, 850, 700, and 500 mb. Except for terrain-level parameters, the analyses are produced on a square grid, 63 x 63, wherein the equator is an inscribed circle.

The mesh length is 381 km at 60 deg lat on a Northern Hemisphere polar stereographic projection. At other latitudes, $\Phi$, the geometric mesh distance is $381 \times \left(\frac{1 + \sin \Phi}{1 + \sin 60}\right)$ km.

The mass-structure processing of input data is accomplished in the following manner. A mean static stability for each of five layers (1000 - 775, 775 - 600, 600 - 400, 400 - 300, and 300 - 200 mb), at each radiosonde station, is determined as a function of the heights of the mandatory pressure levels and sea-level pressure. Objective analyses of the layer stabilities, the 1000-mb height, and the thickness of the

layer 1000 to 500 mb yields grid point values of these key parameters at each of the 3969 grid points. By a complex matrix solution, grid point values of temperature and height, at each of the mandatory pressure surfaces, are generated from the fields of the key parameters. The temperatures so produced are linear in $p^k$ at each grid point (p = pressure; $k = R_d/c_p$; $R_d$ = the gas constant for dry air; $c_p$ = the specific heat at constant pressure) and closely approximate virtual temperatures. The objectively-analyzed fields of the state parameters, pressure (or height), temperature, and moisture, are then available to compute other meteorological quantities, such as those selected for numerical frontal analysis.

For computing derivatives, the grid-point values are approximated by employing the Lagrangian 5-point differentiation formula for centered differences along each of the linear grid axes, I, J, with the two components combined vectorially. See Eq. 8, Chapter II. As a rule, the first derivatives were processed with a low-pass filter, having a cut-off wavelength of four mesh lengths (approximately 850 nautical miles) before further differentiation.

An Example of Two-Dimensional Analyses of DG$\theta$*

Fig. 5 indicates the typical mathematical relationships existing between FNWC's objectively-analyzed isobaric fields of $\theta$* and the patterns of G$\theta$* and DG$\theta$* derived from it for a 5 x 8 mesh-length area (d = 381 km). The illustrations may be regarded as simulations of middle-latitude winter conditions in the low troposphere.

The plan views contain two separate zones of concentrated thermal gradients (i.e., HBZs), the bounding lines of which are shown in each of

the Figs. 5a, b, and c. The field of $\theta^*$ in Fig. 5a is used to generate the isolines of $G\theta^*$ in Fig. 5b. The HBZ associated with the coldest temperatures is most baroclinic with $G\theta^*$ exceeding 2.0 C $(100 \text{ km})^{-1}$ along the zone's centrum. Fig. 5c shows the $DG\theta^*$ field, exhibiting elliptically shaped isolines.

The locus of points along which $\nabla\theta^*$ changes most rapidly in the direction of $\vec{n}_{\theta^*}$ defines the axes of maximal and minimal $DG\theta^*$. These are the warm- and cold-side boundaries of the HBZ, respectively. Both boundaries tend to parallel the isentropes, especially the former (Fig. 5a). It is to be noted that the axes of maximum and minimum $\nabla\theta^*$ (from Fig. 5b) nearly coincide with the zero isolines in Fig. 5c; these lines represent the centrums of the hyper- and sub-baroclinic regions, respectively. The imperfect coincidence of $G\theta^*$ axes and the zero isolines of $DG\theta^*$ is a result of the numerically-computed finite difference approximations to the analytic expressions. Fig. 5d illustrates profiles of $\theta^*$, $G\theta^*$, and $DG\theta^*$ along line N in Figs. 5a--c. The similarity to the schematic profiles in Fig. 2 is obvious.

## Operational Hemispheric HBZ Analysis

Following closely on the development of the HBZ analysis model, FNWC has been producing, twice daily, operational hemispheric 1000 mb numerical frontal analyses for the guidance of Fleet Weather Centrals and Facilities in analyzing the important synoptic-scale low-troposphere fronts. Analysis criteria, degree of smoothing, and other presentation features have evolved during the period 1965 to date.

In view of the experiments in Chapter II, a mean virtual potential temperature for the layer 1000/700 mb, $\overline{\theta}^*$, was selected to generate the

Fig. 5. Typical plan views and profiles of $\theta^*$, $G\theta^*$, and $DG\theta^*$.

a. $\theta^*$ isolines, at intervals of 2.5 K. Positive and negative axes of $DG\theta^*$ superimposed, the latter as dashed lines, the former as dashed lines with alternating circles and diamonds.
b. $G\theta^*$ isolines, at intervals of 0.2 C $(100\ km)^{-1}$. Axes in the $G\theta^*$ field shown as dotted lines. $DG\theta^*$ axes as in a.
c. $DG\theta^*$ isolines, at intervals of .05 C $(100\ km)^{-2}$, with axes as in a; $G\theta^*$ axes from b.
d. Profiles of $\theta^*$, $G\theta^*$, and $DG\theta^*$ along line N in a, b, and c.

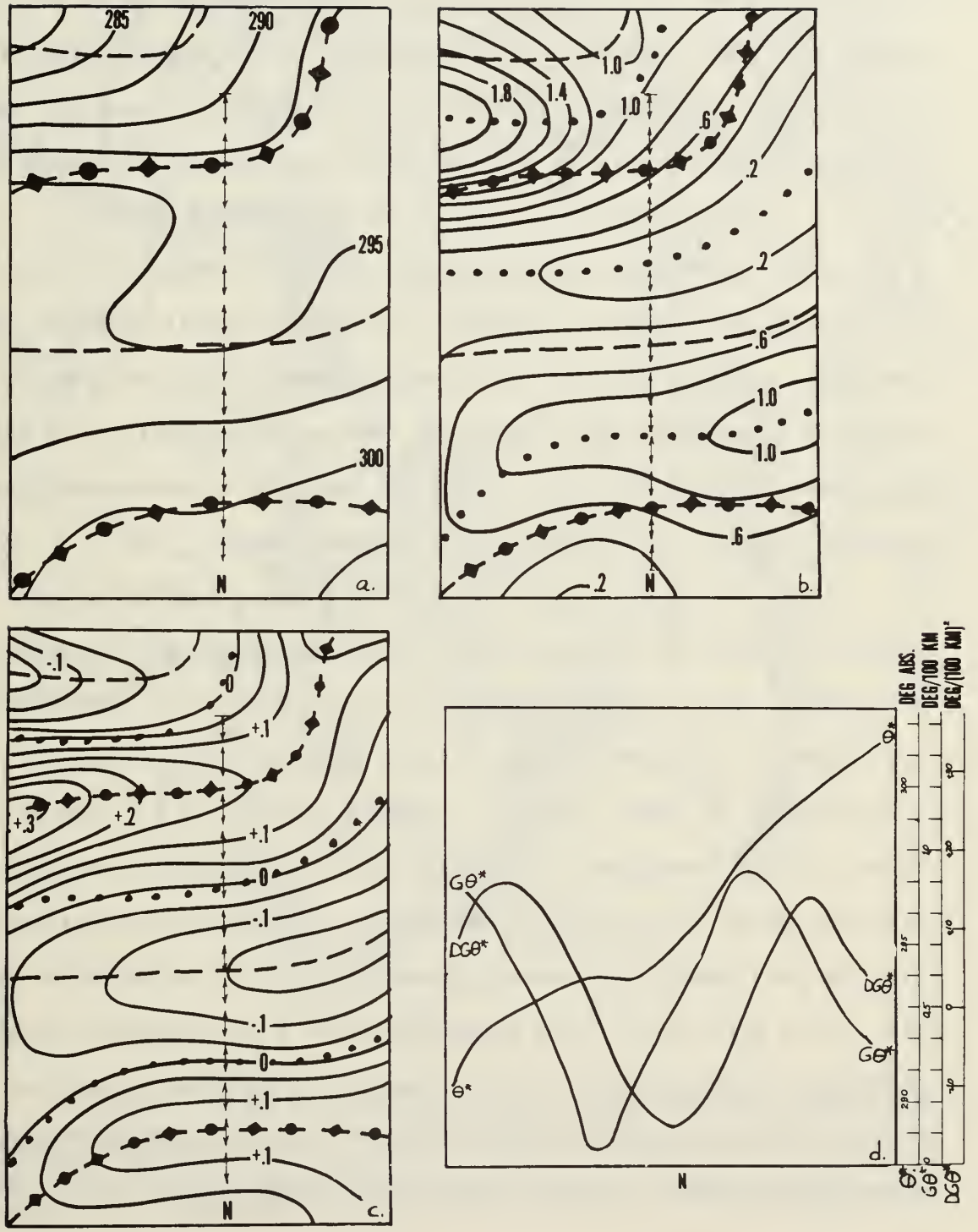
285
290
295
300
N
a.
1.0
1.8
1.4
1.0
.6
.2
.2
.6
1.0
1.0
.6
.2
N
b.
-.1
0
+.1
+.3
+.2
+.1
0
-.1
-.1
0
+.1
+.1
N
c.
Gθ*
DGθ*
θ*
θ*
DGθ*
Gθ*
d.
N
DEG ABS.
DEG/100 KM
DEG/(100 KM)²
θ*
Gθ*
DGθ*

front-location parameter appropriate to the 1000 mb (or surface) chart, $DG\bar{\theta}^*$. For this purpose, $\bar{\theta}^*$ is derived from the layer thickness and assigned to the logarithmic mean isobaric level, 836 mb. The next subsection focuses attention on the merits and deficiencies of the operational $DG\bar{\theta}^*$ analysis with illustrations for a typical winter day. A statistical evaluation of numerical and manual frontal analyses serves to highlight differences and similarities of the two modes of analysis.

Objective Frontal Analysis for 0000 GMT 6 March 1966

The radiosonde observation time, 0000 GMT 6 March 1966, was selected to illustrate the features of objective frontal analysis. This particular synoptic time was not chosen because of the excellence of the numerical frontal analysis, but rather because of availability of many of the charts, fields, etc. (Figs. 6 to 11) necessary to demonstrate the present status of the analysis using the $DG\theta^*$ scheme.

Fig. 6 shows a typical numerically-produced analysis of the frontal parameter on a polar stereographic projection of the Northern Hemisphere. Because layer temperatures are used and since the operational application is to (conventional) frontal analysis, only isolines of positive $DG\bar{\theta}^*$ are shown in Fig. 6, starting with $5 \times 10^{-2}$ C $(100 \text{ km})^{-2}$. Values of $DG\bar{\theta}^*$ lower than 5 units fall in the noise range. The axes of relative maxima in the field of the elliptically-shaped isolines represent the positions of the warm-side boundaries of the 1000 mb HBZs, hence they may be used by the field meteorologist as a first guess to locate the significant surface fronts. As an example, the numerically-analyzed 1000 mb fronts in the middle and eastern Atlantic area are indicated by the superimposed dashed lines which trace out the $DG\bar{\theta}^*$ axes.

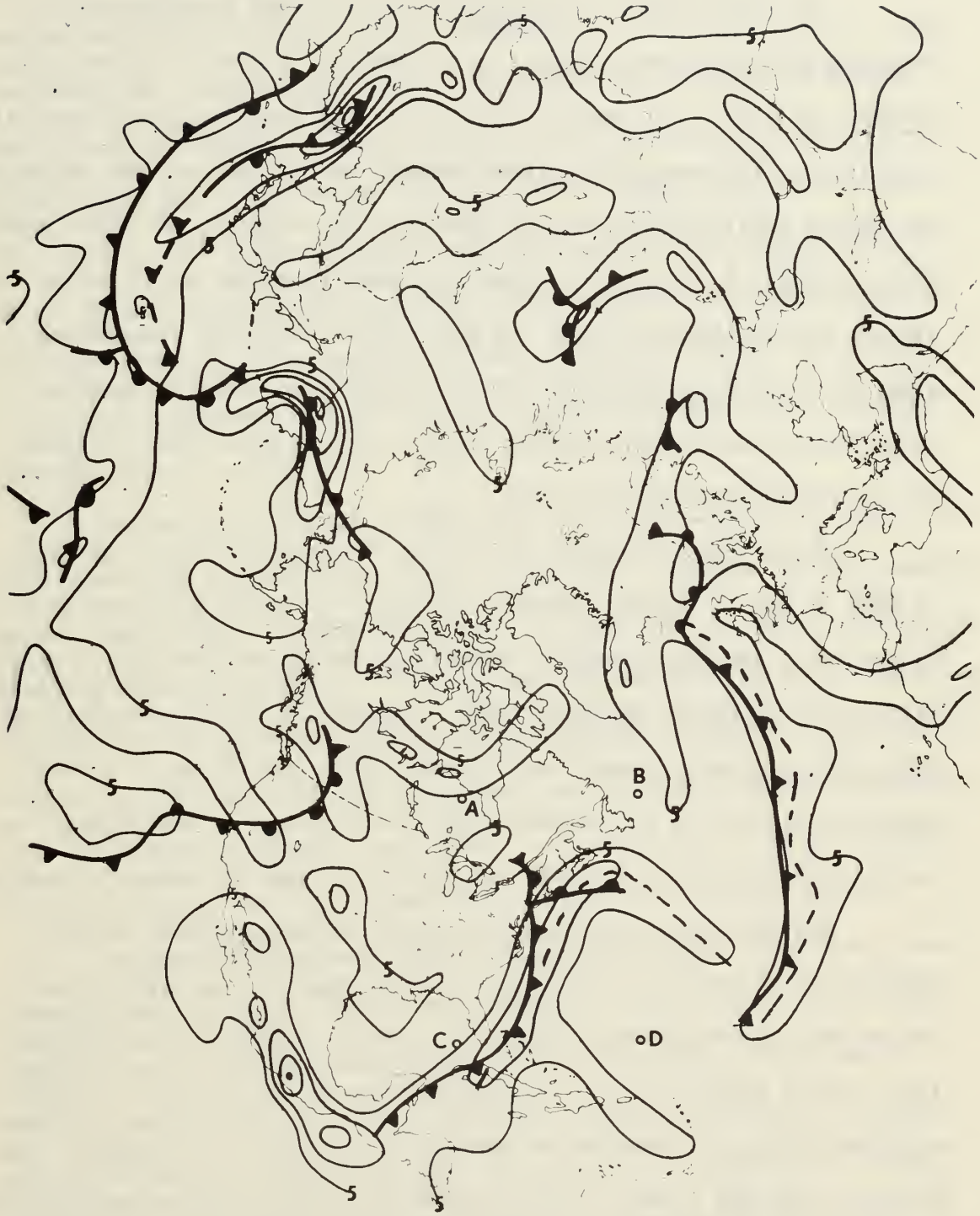


Fig. 6. $DG\bar{\theta}^*$ (1000/700 mb) analysis for 0000 GMT 6 March 1966. Isolines at interval of 20 x $10^{-2}$ C $(100\ km)^{-2}$, starting with +5 units. $DG\bar{\theta}^*$ axes indicated by dashed lines for a section of the Atlantic area. NMC fronts are shown with conventional symbols. Alphabetical designators A, B, C, D refer to Fig. 16.

What constitutes a significant front or HBZ boundary may be determined by the spatial extent of a $DG\bar{\theta}^*$ axis and the attendant magnitudes, as well as by the location, general orientation, and shape of this field. The nearly meridional eastern United States-North Atlantic and nearly zonal western Pacific $DG\bar{\theta}^*$ axes are examples of significant fronts in Fig. 6. Extensive zones with $DG\bar{\theta}^*$ in excess of 25 units signify intense fronts; these are HBZs containing large temperature gradients. Note the northern Pacific--Siberia and western Pacific--China fronts with $DG\bar{\theta}^*$ exceeding 25 units over a large area; maximum values are greater than 65 units.

The orientations, but not necessarily the positions, of axes of $DG\bar{\theta}^*$ in Fig. 6 appear reasonable relative to the fronts usually seen on the daily synoptic analyses emanating from the National Meteorological Center, Suitland, Maryland (NMC). However, air-mass designations (now mostly extinct, anyway) and movement (warm, cold, etc.) are not indicated explicitly in the $DG\bar{\theta}^*$ field; also, stage of development, as the occluded stage, is difficult to interpret from the numerical analysis.

The problem of locating occlusions in the numerical frontal analysis is manifest over the eastern North America--western Atlantic region and the central-western Pacific. Minor bulges in the $DG\bar{\theta}^*$ isolines may be associated with occluded structure but a unique empirical solution for this aspect of the analysis is difficult to program. The occlusion problem relates to the direction in which the virtual potential temperature derivatives are computed (Eqs. [2] and [3]). A typical view of NMC's subjectively-analyzed surface occlusions in relation to the 1000/500 mb thickness lines serves to illustrate the problem well (Fig. 7).

The occluded fronts over the Pacific Ocean west of 180 deg and over the western and eastern United States intersect thickness lines (i.e., mean isotherms) at angles which, in many instances, are as much as 90 deg. Such frontal orientations are not likely to be derived by computations of $DG\bar{\theta}^*$ from Eq. 3, as may be noted in Fig. 6. With reference to Eqs. (2) and (3), if the front-location derivatives could be calculated in the $\vec{n}_t$ rather than in the $\vec{n}_{\theta^*}$ direction the problem associated with the numerical analysis of occlusions would not exist. A later section of this chapter discusses a modification to the $DG\bar{\theta}^*$ model which somewhat alleviates the problem.

The multiplicity and orientation of fronts implied in Fig. 6 has more similarity to the frontal-contour analyses performed by the Canadian Meteorological Service (Anderson et. al., 1955) than by NMC. Lacking an absolute standard, analyses from both weather services have been taken as the best available, especially in the dense-data North American and North Atlantic areas, and, as such, have been used in statistical comparisons with the objective frontal positions. A later section of this chapter presents results from the coevaluation of NMC and objective fronts.

Numerically-analyzed fronts tend to be stronger over land than ocean; fronts near the land-ocean interface of continents (especially eastern continents) are pronounced. Part of the reason for these analysis features is due to the sparsity of data over oceans and areas of rugged terrain. However, it is also true that the relatively large intensity over land is due to the rapidly-varying height and nature of the underlying surface. Use of $\bar{\theta}^*$ vice $\theta^*$ has not eliminated topographic effects on the objectively-derived frontal patterns, as indicated by the

Fig. 7. NMC surface fronts superimposed on the NMC 1000/500 mb thickness pattern for 0000 GMT 6 March 1966. Segments of the 1000 mb objective fronts (from Fig. 8) near the NMC occlusions are shown for the western Pacific and Atlantic Oceans and western United States and Canada (heavy dashed lines).

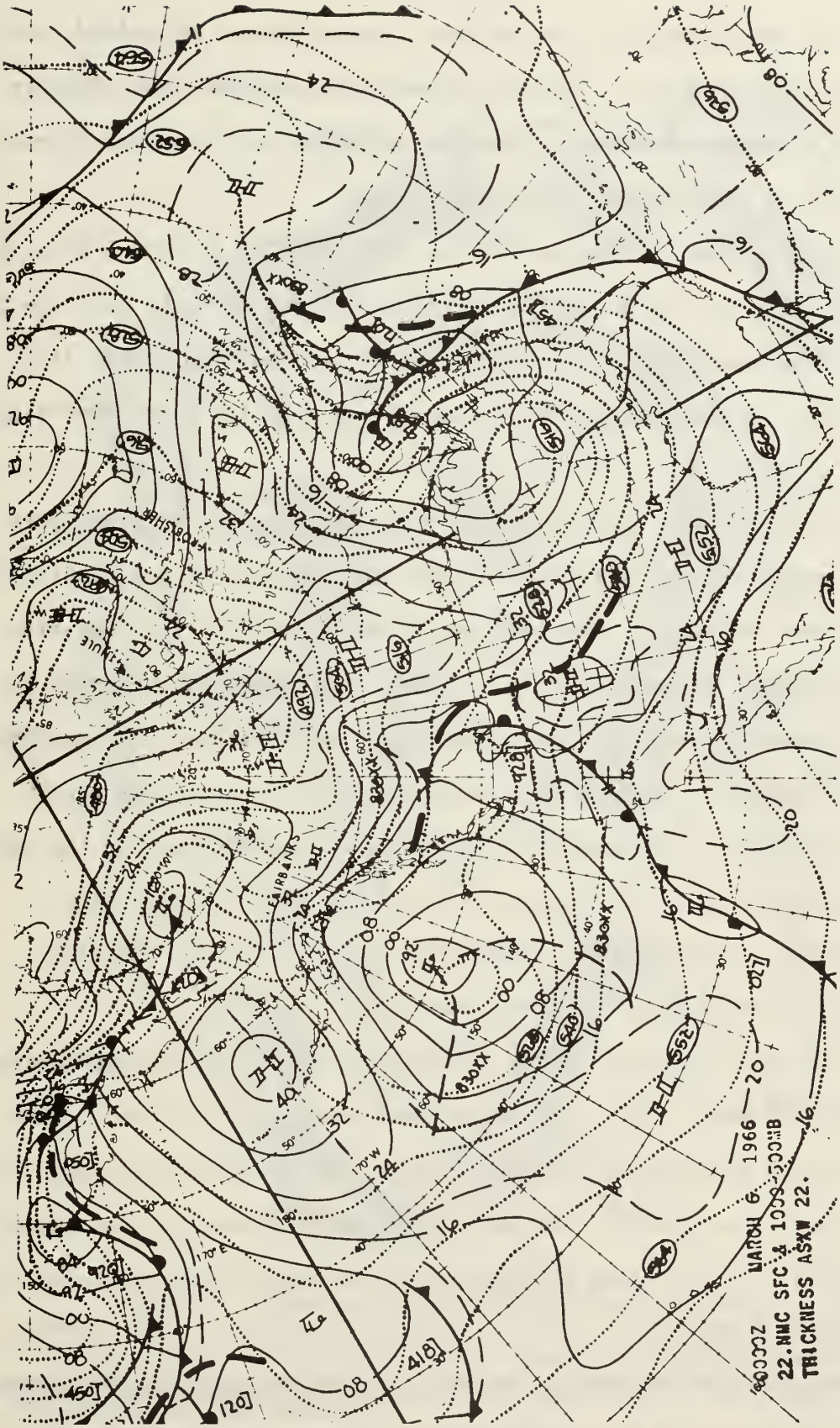
22.NMC SFC & 1000-500MB
THICKNESS ASXN 22.
MARCH 6, 1966 — 20 GMT
FAIRBANKS

analysis in the vicinity of the Rockies, Sierra Madres, Greenland, and Himalayan areas in Fig. 6. Studies of monthly-mean $DG\bar{\theta}^*$ axes (Chapter VIII) and attempts to remove orographic influence and interface effects are germane to this problem (Reed, 1961).

As indicated in Chapter II, limiting the $DG\bar{\theta}^*$ plot to 5 units and greater screens out the noise frequently associated with the very low $DG\bar{\theta}^*$ values in the subbaroclinic regions. Such a scheme also avoids displaying those insignificant zones of hyperbaroclinicity where $DG\bar{\theta}^*$ values are $< +5$ units.

The occurrence of a double frontal structure in NMC's analysis for the western Pacific but only a single HBZ boundary in the numerical analysis and the tendency for $DG\bar{\theta}^*$ positions to occur on the warm-side of NMC positions, as shown both in the west and east Atlantic (Fig. 6) are manifestations of broadening effects and the close proximity of HBZs. Such problems were discussed in connection with the simulation experiments in Chapter II. Grossness of mesh length, peculiarities of the data processing, and the differentiation and interpolation schemes used play a part in explaining the differences in positions of manually-analyzed and numerically-analyzed fronts.

Fig. 8 illustrates FNWC's operational version of the $DG\bar{\theta}^*$ analysis for 0000 GMT 6 March 1966. The operational chart is a function of the limited amount of data received by observation time plus four hours. This fact and the retention of a few small isolated $DG\bar{\theta}^*$ zones in the operational version (areas A and B) account for the minor differences existing between Figs. 6 and 8.

Figs. 9 and 10 show the operational 1000 mb numerically-analyzed fronts superimposed on the sea-level pressure field and the 850 mb

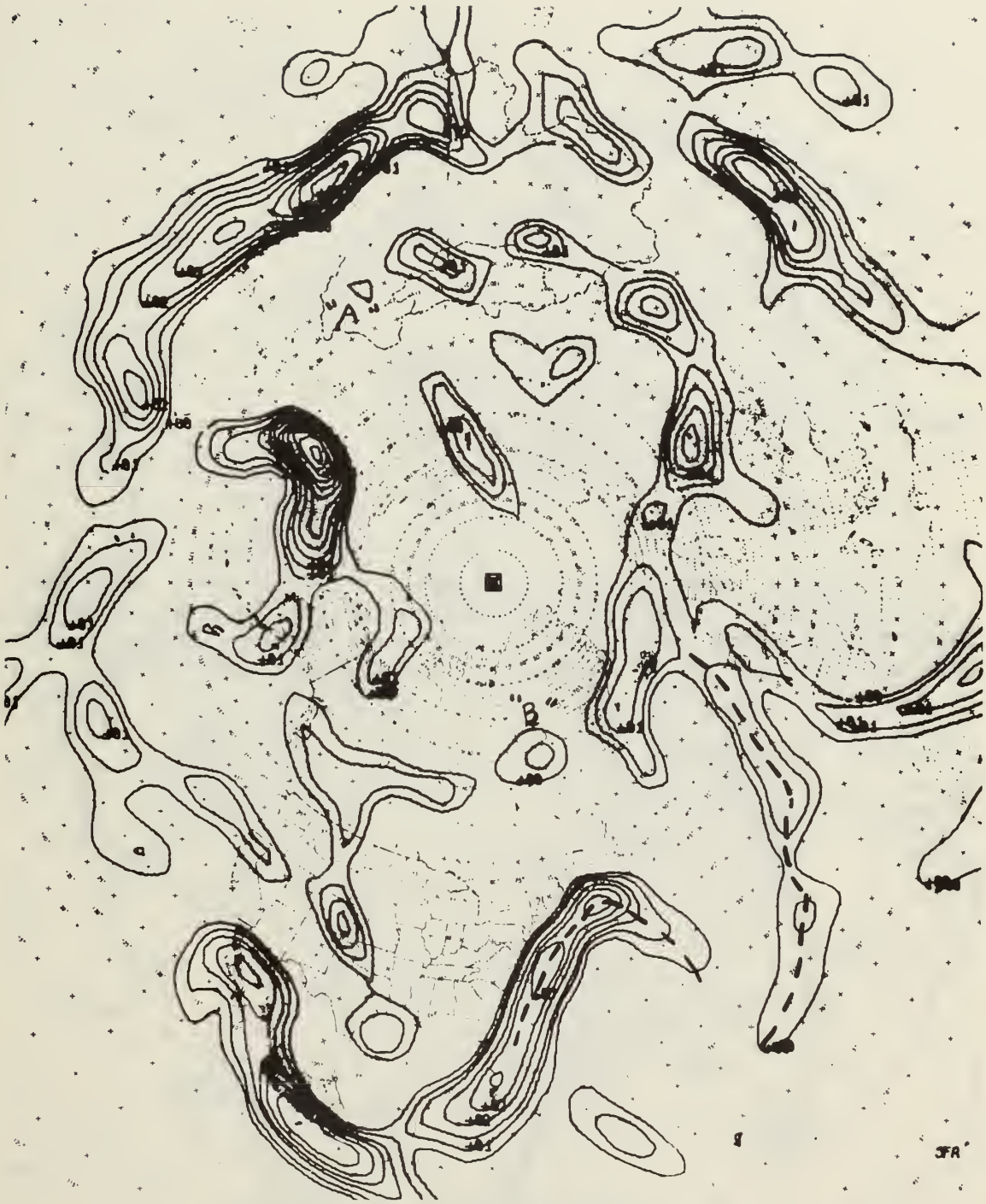


Fig. 8. Operational $DG\bar{\theta}^*$ (1000/700 mb) analysis for 0000 GMT 6 March 1966. Isolines at interval of $5 \times 10^{-2}$ C (100 km)$^{-2}$, starting with the +5 line. $DG\bar{\theta}^*$ axes (dashed lines) are manually positioned for portions of the Atlantic area, similar to Fig. 6. A and B indicate insignificant $DG\bar{\theta}^*$ features.

Fig. 9. FNWC sea-level pressure field, 0000 GMT 6 March 1966. Isobar interval: 4 mb. 1000 mb numerically-analyzed fronts ($D_G\theta^*$ axes) from Fig. 8 (heavy solid lines) with movement characteristics shown for the west and east Atlantic Ocean fronts by conventional symbols.

Fig. 10. FNWC 850 mb isotherm and contour field, 0000 GMT 6 March 1966. Isotherms (thin solid lines) at 5 C interval, contours (thin dashed lines) at 60 met interval. 1000 mb numerically-analyzed fronts ($D_G\theta^*$ axes) from Fig. 8 (heavy solid lines) with movement characteristics shown for the west and east Atlantic Ocean fronts by conventional symbols.

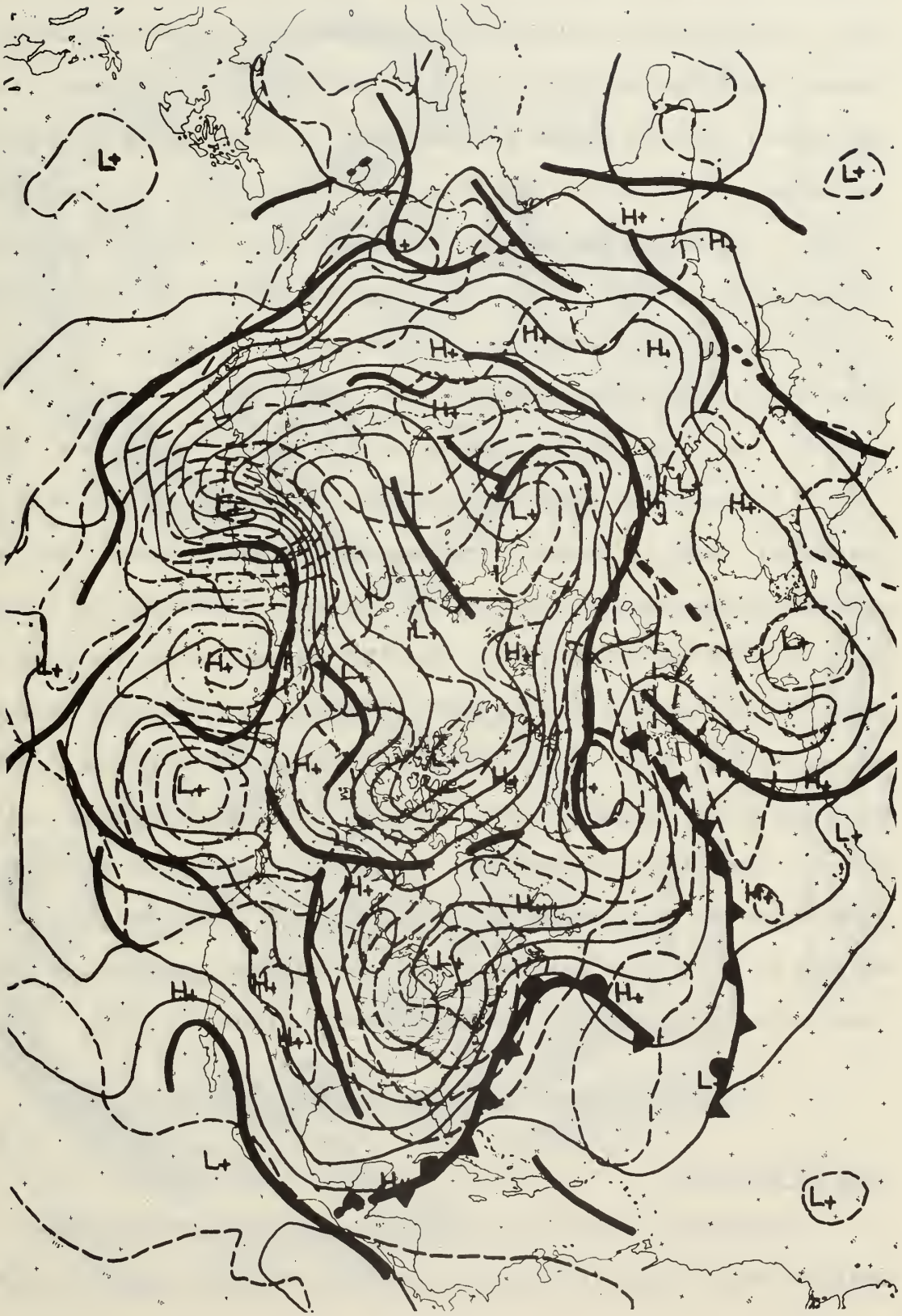

isotherm-contour chart, respectively. The symbols designating warm, cold, and stationary are derived from geostrophic winds at sea-level and thermal conditions at 850 mb. Most of the $DG\bar{\theta}^*$ axes are located in or are close to troughs in the pressure field, giving evidence of internal consistency in the mass structure model used to process the input data at FNWC. The 850 mb isotherm pattern agrees quite well with the position of the objective fronts. There is a distinct tendency for the isotherms to parallel the HBZ boundary except near pressure centers, similar to manually-analyzed fronts (Fig. 7).

Objective Frontal Prognosis for 1200 GMT 7 March 1966

The numerical model described here may be used equally well for objectively locating fronts in the prognostic thermal fields. Fig. 11 shows the operational 36-hour 1000 mb prognosis of $DG\theta^*$ and the verifying chart for 1200 GMT 7 March 1966. The FNWC prognostic model used to generate the isotherms from which $DG\theta^*$ is computed is a modified barotropic scheme (Hughes, 1967). Such a model may be expected to smooth or eliminate the minor thermal waves but leave the more intense and extensive synoptic-scale features intact. It is for this reason that the level ($DG\theta^*$) vice the layer ($DG\bar{\theta}^*$) HBZ analysis is applied to the prognostic thermal fields. It is emphasized that the prognostic frontal positions result from an analysis of prognostic thermal fields.

## Comparison of Subjective and Numerical Frontal Analyses

### 1000 mb Analyses

Comparative statistics on the objectively- and subjectively-analyzed frontal positions serve to quantify the observations on $DG\bar{\theta}^*$

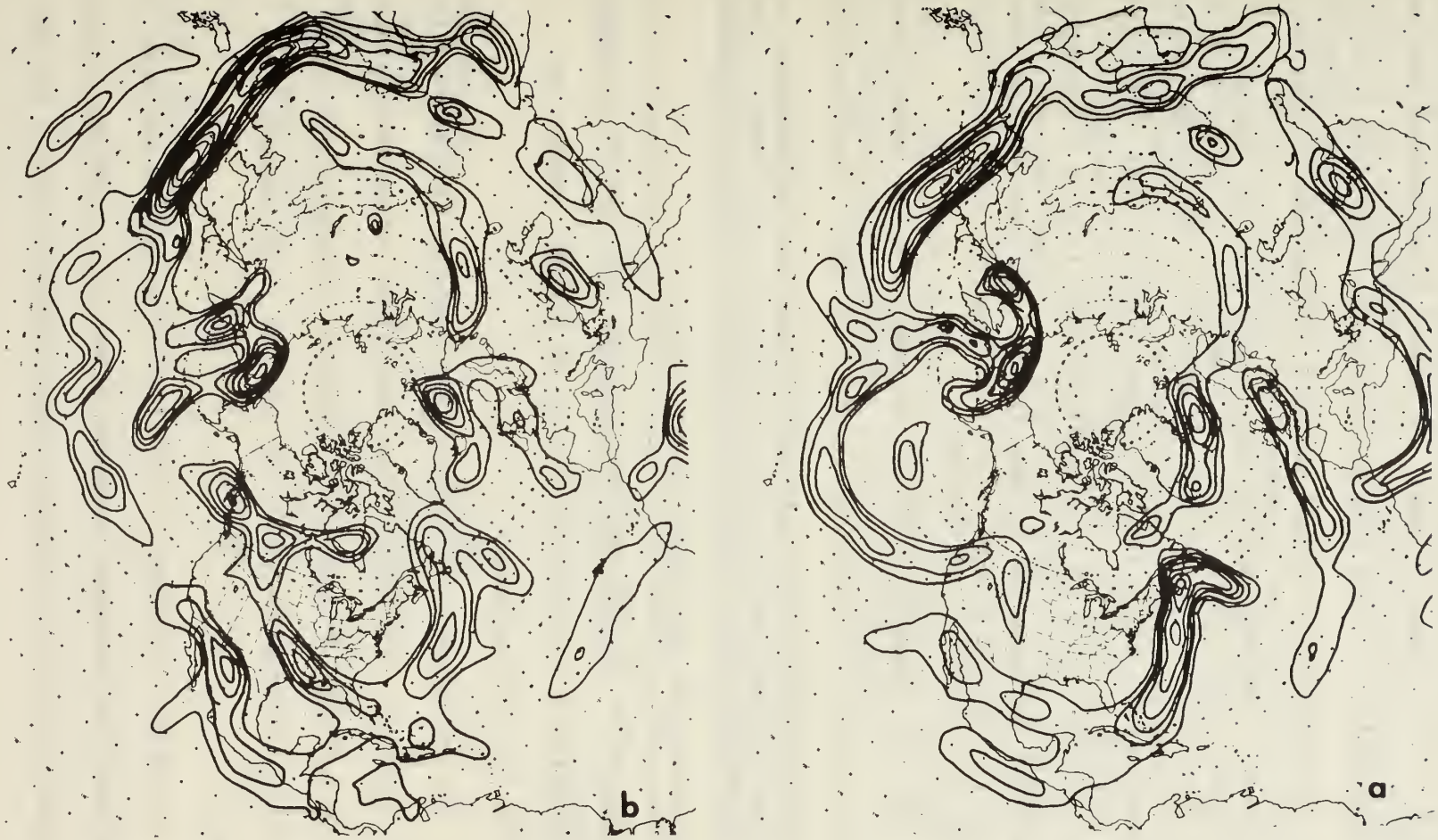


Fig. 11. a. Operational 36-hour prognosis of 1000 mb DG$\theta$* for 1200 GMT 7 March 1966. Interval: $5 \times 10^{-2}$ C $(100 \text{ km})^{-2}$, starting with the +5 isoline.
b. Verifying 1000 mb DG$\theta$* analysis for 1200 GMT 7 March 1966. Interval: $5 \times 10^{-2}$ C $(100 \text{ km})^{-2}$, starting with the +5 isoline.

made earlier in the chapter as well as give direction to the search for modifications to the present program. It should be emphasized that an absolute standard for locating HBZs does not exist, therefore it is necessary to compare manual frontal analyses of high quality with the numerical product. The NMC analyses were chosen for this purpose.

The most extensive evaluation was made for a late summer period of sixteen observations times from 23 August to 6 September 1965 (Table 6). Over 250,000 nautical miles of numerically-located 1000 mb fronts were compared with the analogous NMC surface fronts. The more obvious conclusions from this study are as follows:

1. The two independent frontal analyses have the closest relation over dense-data land and ocean areas, such as the United States and the Atlantic Ocean while the relation is poorest over the Pacific Ocean and North African areas. The 1.2 deg lat difference for Asia is considered anomalously low and not representative of that area.

2. The objective HBZ positions north of 30N, and over eastern portions of continents and western portions of oceans, compare most favorably with the NMC positions.

3. Only 66 percent of the NMC fronts could be associated with the objective fronts. The remainder are occlusions and/or weak fronts in eastern ocean areas. Both of these types are frequently analyzed from time continuity considerations only and are in the process of frontolyzing.

4. A similar percentage of significant objectively-analyzed fronts (72 percent) could be associated with NMC fronts. The remainder represent baroclinic zones over North Africa and other subtropical ocean and land

areas as well as those fixed to orographic features. Following prevalent air mass theory, the subjective analyst hesitates to place stationary fronts on the periphery of desert or mountainous areas, despite the nature of thermal patterns.

A more recent, but quite limited, evaluation for the four synoptic times, 0000 GMT and 1200 GMT, 26 and 27 January 1967, considered approximately 57,000 nautical miles of Northern Hemisphere fronts without regard to classification by region. An average position difference of 2.6 deg lat between NMC surface and objective ($DG\overline{\theta}^*$ model) 1000 mb fronts resulted. Forty-two percent of the numerically-computed fronts were found on the warm-air side of NMC fronts with an equal number on the cold-air side. The remainder were coincident, to within 1/4 deg lat.

Table 6. Statistical relations between numerically-analyzed 1000 mb ($DG\overline{\theta}^*$ model) and manually-analyzed NMC surface fronts for sixteen observation times in the period 23 August to 6 September 1965.

| Sector | Objective Fronts Sampled (n mi) | Average Distance Separating NMC & Objective Fronts (deg lat) |
|---|---|---|
| North America | 49,250 | 1.6 |
| Atlantic | 46,900 | 1.4 |
| Pacific | 46,300 | 2.1 |
| Europe-North Africa | 26,000 | 1.8 |
| Asia | 18,000 | 1.2 |
| Overall average | | 1.7 |

850 mb Analyses

Although, at this point, it is not the intent to discuss vertical consistency of numerically-analyzed fronts (see Chapter V ) it is appropriate to the substance of this chapter to show the 850 mb $DG\theta^*$ version for 0000 GMT 6 March 1966, in order to demonstrate the relative merits of numerical frontal analysis using mandatory level and layer data.

From the conventional synoptic point of view, the 850 mb fronts are expected to be on the cold-air side of their 1000 mb counterparts. But, as noted from a comparison of Figs. 6 and 12, the objective 850 mb fronts are coincident with or are on the warm-air side of the 1000 mb fronts derived from the $DG\bar{\theta}^*$ model. To show that this abnormal situation is not uncommon, the following is offered in evidence. With reference to the evaluation of late January 1967 frontal analyses, described above, the average distance between 850 mb NMC and objectively-located fronts is 2.6 deg lat which is the same distance as that for the NMC surface versus objective 1000 mb. However, only 19,000 nautical miles of front were considered at 850 mb, most of which were over the dense-data North American region. Thus, considering the area sampled, the 850 mb positions of numerically-analyzed and NMC fronts compare less favorably than their counterparts at or near the surface. But, of greater importance is the fact that 86 percent of the 850 mb numerically-located positions were found on the warm side of NMC's 850 mb fronts, with an algebraic average distance of 2.3 deg lat. Such bias relative to NMC did not exist for the objective 1000 mb fronts derived from $\bar{\theta}^*$.

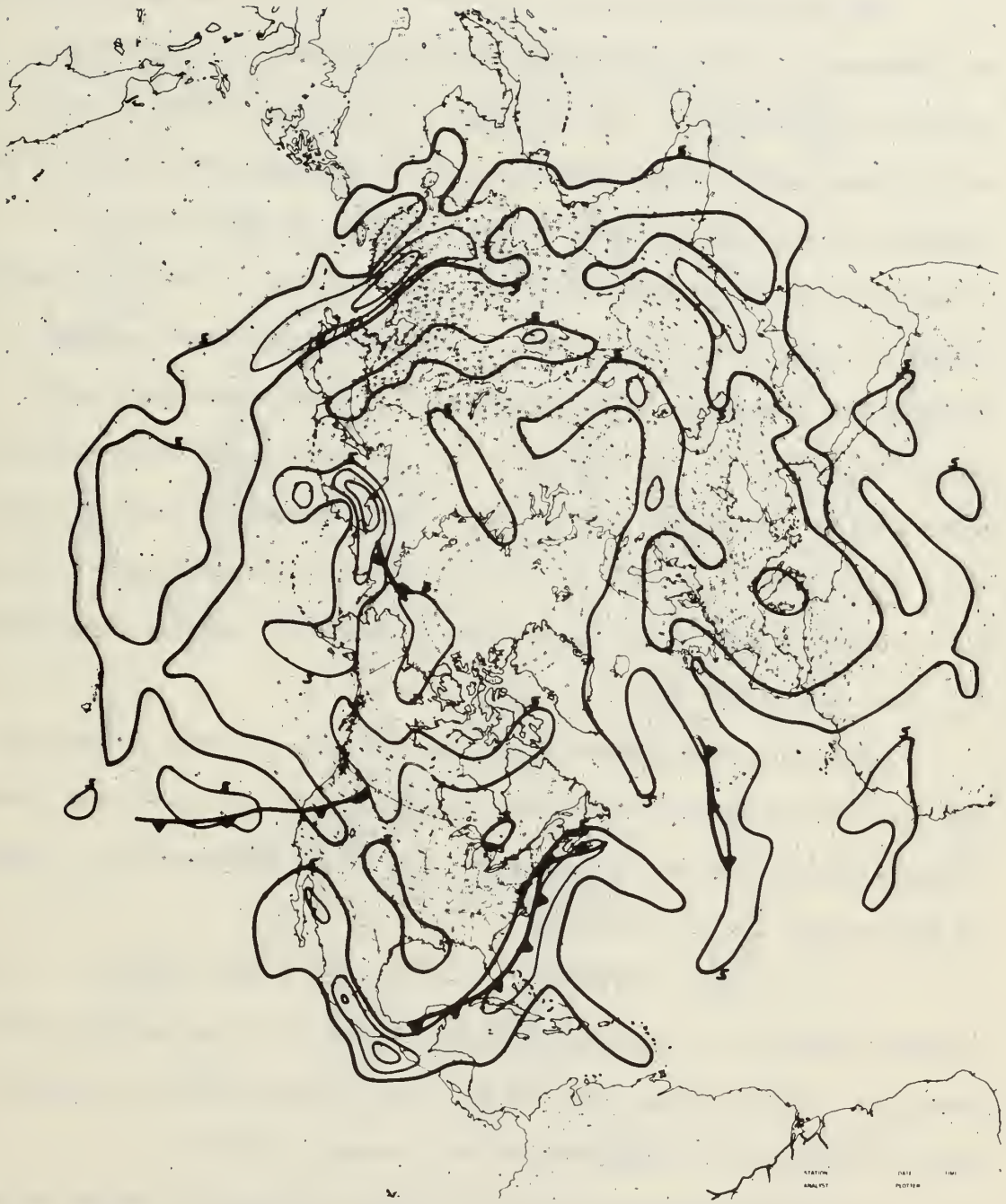

Fig. 12. 850 mb DG$\theta$* analysis for 0000 GMT 6 March 1966. Isolines at interval of 20 x $10^{-2}$ C $(100\ km)^{-2}$, starting with +5 units. The available NMC fronts at 850 mb are shown with conventional symbols.

Modification of $DG\bar{\theta}^*$ to Enhance the Analysis of Occlusions

One of the more obvious omissions in the analyses generated by the $DG\bar{\theta}^*$ model is the conventional occluded structure, as discussed earlier in the chapter. Occlusions are accepted and common to all national and international weather services, except perhaps that of the Canadians, whose working model features troughs of warm air aloft (trowals) as substitutes for the occlusion (Galloway, 1958). The well-developed occlusions on the surface charts of United States weather services are generally associated with a large-amplitude prefrontal tongue of warm air, as may be noted over the western Atlantic--eastern North America region and over the western North Pacific Ocean at 0000 GMT 6 March 1966 (Fig. 7). Such occluded fronts intersect the isotherms at considerable angles and $\vec{n}_{\theta^*}$ becomes a relatively poor approximation to $\vec{n}_l$. (See Eqs. 2 and 3).

The close coincidence of the thermal axis of warm temperature and the conventional occlusion suggests application of the Laplacian operator to temperature in order to locate the "occluded" HBZ boundaries. Using $\bar{\theta}^*$ as the thermal field of interest,

$$-\nabla^2\bar{\theta}^* = -\nabla|\nabla\bar{\theta}^*|\cdot\vec{n}_{\bar{\theta}^*} - |\nabla\bar{\theta}^*|\nabla\cdot\vec{n}_{\bar{\theta}^*} \equiv DG\bar{\theta}^* + GK\bar{\theta}^*. \qquad (11)$$

As noted in Eqs. (5) and (6), the $DG\bar{\theta}^*$ parameter is indicative of the vorticity of the thermal wind due to shear and thus $GK\bar{\theta}^*$ is representative of the curvature component of the thermal vorticity.

Fig. 6 demonstrates the poor relation of manually drawn occlusions to the field of $DG\bar{\theta}^*$. $GK\bar{\theta}^*$ (Fig. 13), which isolates the effect of the curvature term, is not adequate either to depict occlusions or any other frontal phenomena for that matter. The same comment is true for the

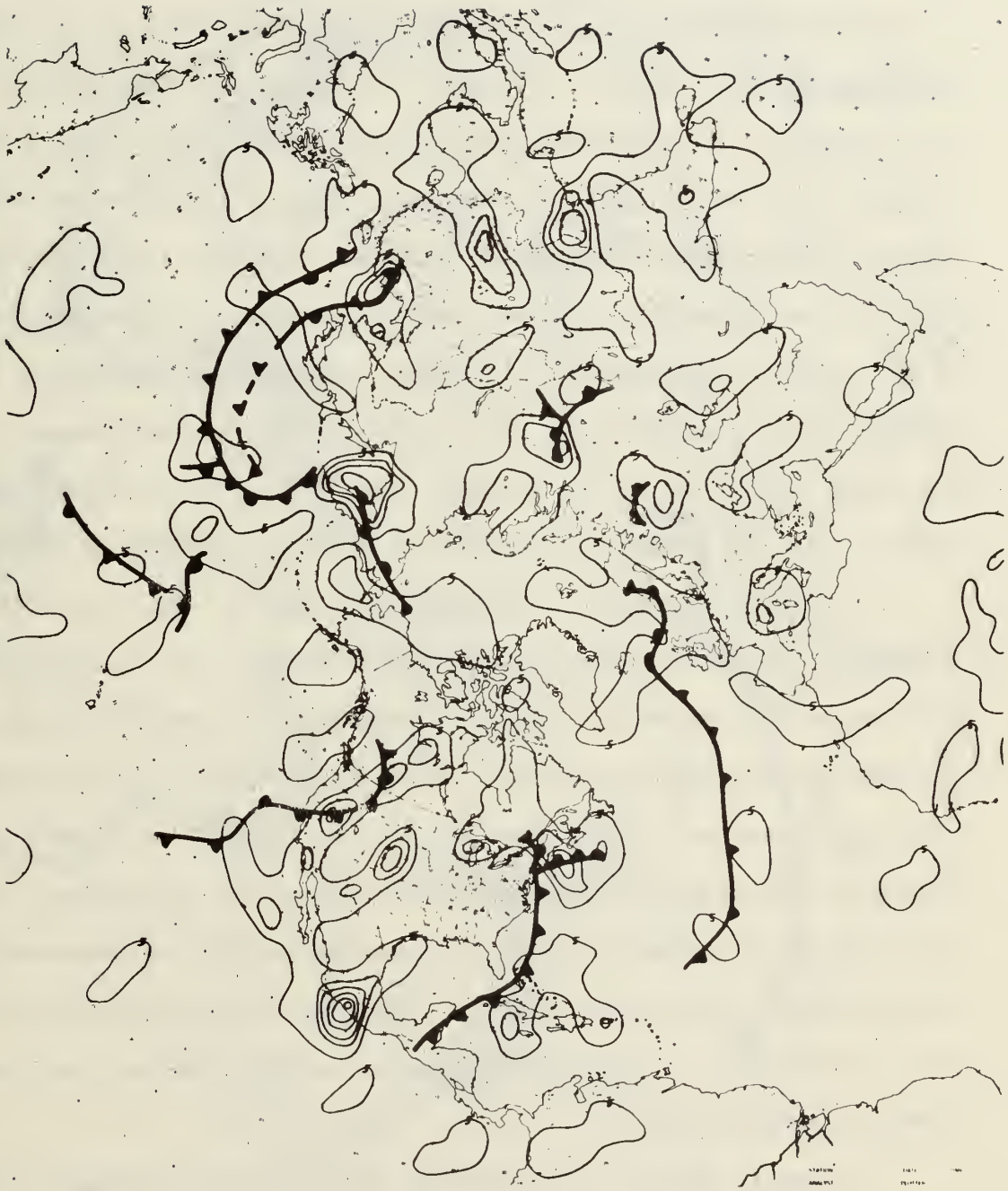

Fig. 13. $GK\bar{\theta}^*$ (1000/700 mb) analysis for 0000 GMT 6 March 1966. Isolines at intervals of 20 x $10^{-2}$ C $(100\ km)^{-2}$, starting with +5 units. NMC fronts are shown with conventional symbols.

Laplacian itself (not shown) since thermal tongues also occur in areas other than the location of conventional-front discontinuities. However, it is productive to combine the curvature and shear terms of Eq. (11) in a selective manner, that is only in the area of negative $DG\bar{\theta}^*$ between the zero values within the HBZ and the adjacent subbaroclinic zone. This version is called Mod $DG\bar{\theta}^*$ and is shown in Fig. 14. Such a procedure preserves the continuity of the non-occluded warm-side boundaries of the HBZs depicted by $DG\bar{\theta}^*$ alone since these occur with positive $DG\bar{\theta}^*$. A blow-up of a section of the numerical frontal analysis over the western Atlantic-eastern United States area in Fig. 14 exemplifies the enhancement of the occlusion analysis by use of Mod $DG\bar{\theta}^*$ (Fig. 15). Note that $DG\bar{\theta}^*$ and Mod $DG\bar{\theta}^*$ are the same except on the cold-air side of zero $DG\bar{\theta}^*$ in the HBZ.

It is of interest to compare Figs. 6 and 14. Note the differences in orientation and structure of the HBZ boundaries that are associated with occlusions, as for example over the extreme eastern and western sections of northern United States as well as northern Russia. Unfortunately, the curvature modification afforded by Mod $DG\bar{\theta}^*$ is not always desirable. An example of this may be noted over the subtropical area of North America, a region frequently associated with low-tropospheric thermal tongues. Here, an already troublesome area for frontal analysis, due to topography and sparse-data problems, suffers further from the curvature modification.

Overall, the major objection to the Laplacian adjustment for occluded structure is that the curvature-vorticity term is not directly related to baroclinicity and hence fictitious temperature gradients are implied. These objections have kept the program from becoming operationally useful.

Fig. 14. $(DG\bar{\theta}^* + GK\bar{\theta}^*)$ for $DG\bar{\theta}^* < 0$, $GK\bar{\theta}^* > 0$, and $|GK\bar{\theta}^*| > |DG\bar{\theta}^*|$: 0000 GMT 6 March 1966. Isolines at intervals of 20 x $10^{-2}$ C $(100\ km)^{-2}$ starting with +5 units. Axis values $\geq$ 15 units: xxxx: NMC fronts shown with conventional symbols.

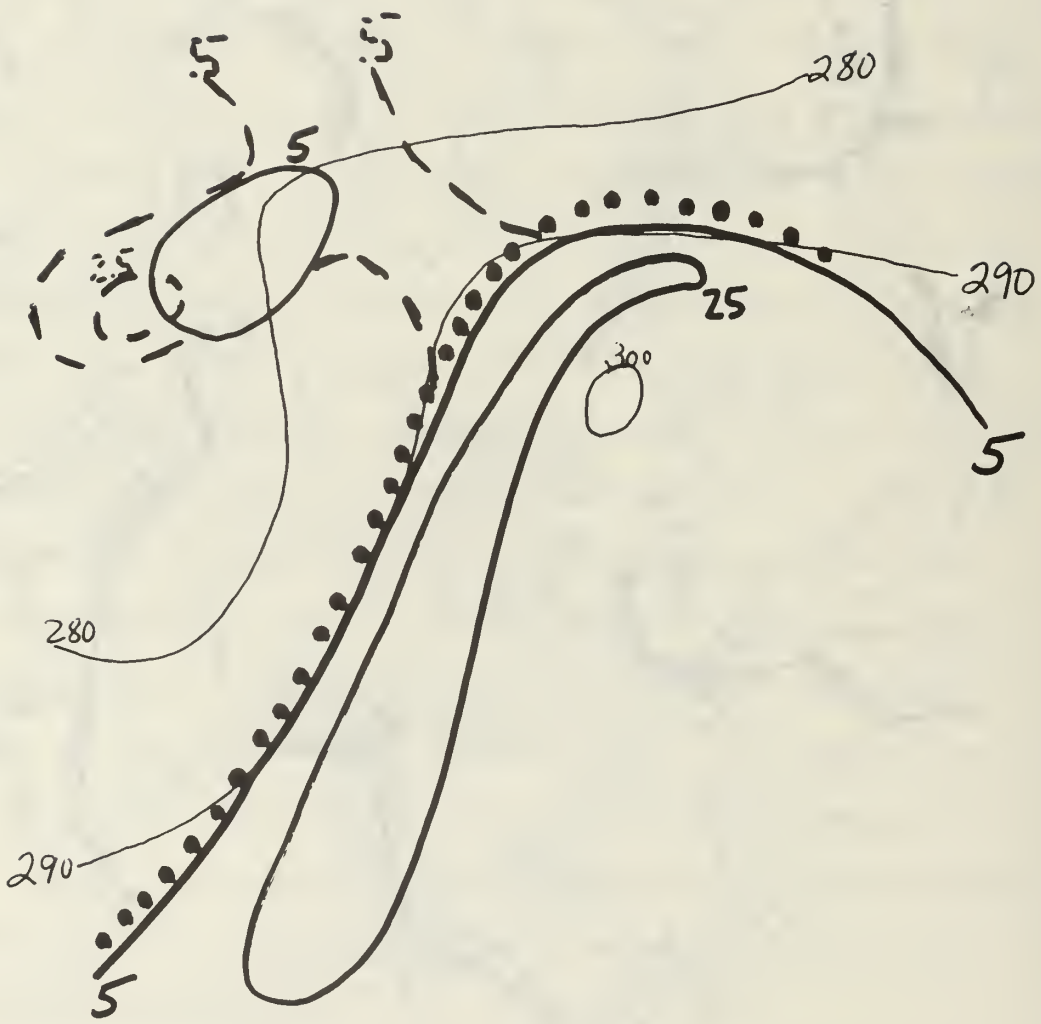


Fig. 15. Modification to the $DG\bar{\theta}^*$ (1000/700 mb) analysis for the case of a frontal occlusion over the western Atlantic--eastern United States area, 0000 GMT 6 March 1966. $\bar{\theta}^*$ in K: light solid lines; major axis of zero $DG\bar{\theta}^*$: dotted line; $DG\bar{\theta}^*$ and mod $DG\bar{\theta}^*$ in $10^{-2}$ C $(100\ km)^{-2}$: heavy solid and dashed lines, respectively.

Some work has been done by Kirk (1965, 1966, and 1967) on incorporating the Laplacian effect into objective frontal analyses. The unqualified favorable appraisal of $\nabla^2 T$ as a front-location parameter, given by Kirk in these references, completely misrepresents the utility of this approach.

## Effect of Mesh-length Variation on $DG\bar{\theta}^*$

In Chapter II the effect of reduction in mesh length on the location and intensity of frontal zones was demonstrated for a limited case involving the modeled N and M temperature profiles. The results there suggest a similar study using real-atmosphere data.

Consistent with both the simulation and operational experiments, the mean virtual potential temperature for the layer 1000/700 mb ($\bar{\theta}^*$) and the synoptic time, 0000 GMT 6 March 1966, were selected for this substudy relating mesh length variation to objective frontal analysis. In particular, the frontal zone chosen for study is that portion of the significant HBZ in the western Atlantic--eastern North American region contained in the area identified by corners ABCD in Fig. 6. The subject HBZ is considered as moderate (M) in terms of the symbolic profiles in Chapter II (Fig. 3); the average baroclinicity is 1.6C $(100\ km)^{-1}$ through the frontal zone. Starting with the full mesh grid-point values of $\bar{\theta}^*$, the temperature data were numerically interpolated to the .75, .5, and .25 mesh intersections using Bessel's central difference formula. Subsequently, the fields of $G\bar{\theta}^*$ and $DG\bar{\theta}^*$ were produced for each of the new grids in a manner consistent with that described earlier in the Chapter.

Fig. 16 illustrates the important aspects of the $DG\bar{\theta}^*$ analysis on the full, half, and quarter mesh grids. Results for the three-quarter

Fig. 16. $DG\bar{\theta}^*$ analysis as a function of mesh length for area identified by corners ABCD in Fig. 6, 0000 GMT 6 March 1966. Positive and negative axes of $DG\bar{\theta}^*$: from full mesh (heavy solid lines), half mesh (heavy, long dashed lines), and quarter mesh (heavy short dashed lines). $DG\bar{\theta}^*$ isolines intersecting positive (negative) axes, starting with +.35 (-.25) x $10^{-2}$ C $(100\ km)^{-2}$ at intervals of 10 units: from full mesh (light solid lines), half mesh (light dashed lines), and quarter mesh (dotted lines). $\bar{\theta}^*$ isolines (K) indicated by edges of shaded areas.

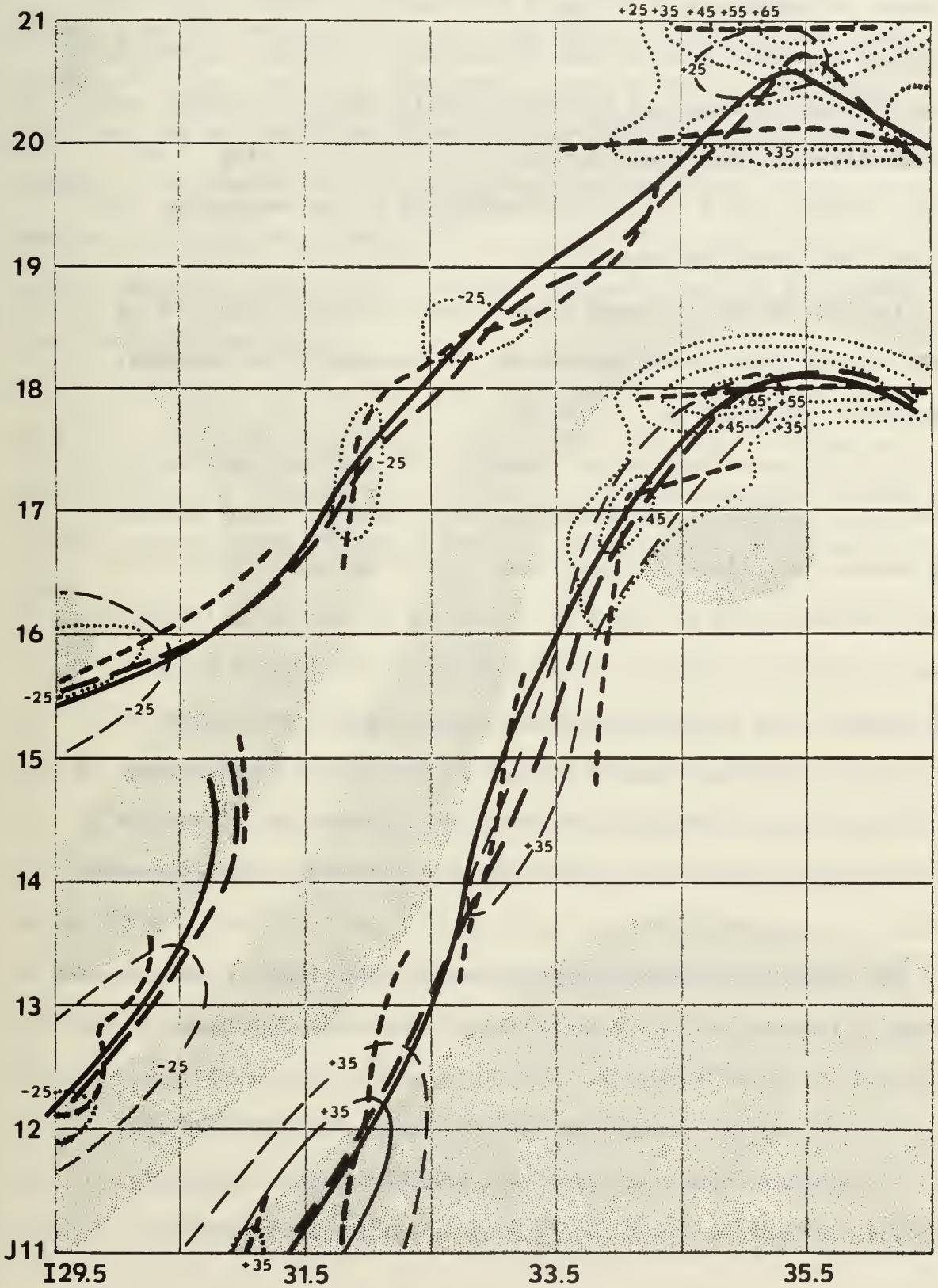
21
20
19
18
17
16
15
14
13
12
J11
I29.5
31.5
33.5
35.5
+25 +35 +45 +55 +65
+25
+35
-25
-25
-25
+65
+55
+45
+35
+45
-25
-25
+35
-25
+35
+35
+35

mesh were intermediate to those for the full and half mesh and are not shown here. A background of full-grid $\bar{\theta}^*$ (shaded) is shown to point out an important departure from the modeled profiles in Chapter II, namely, that the warm air is much less barotropic and the cold air somewhat more baroclinic than the counterpart sections in the M profile (Fig. 3 and Table 1). However, at J < 15 similar conditions in the modeled and real-atmosphere temperatures do prevail.

Analysis of the positions of warm- and cold-side boundaries of the HBZs and the frontal-zone intensities, as implied by the numerical $DG\bar{\theta}^*$ analysis, indicates the following:

1. Full versus half mesh: Overall, both full and half mesh patterns are similar in position and extent of the HBZ. Clear evidence of the positive correlation of mesh size and frontal-zone width is confined to the area below J14 where the latter is reduced up to 10 percent (40 kms) in the half- compared to full-mesh case. Poleward of J14 the half-mesh HBZ widths show both increases and decreases compared to full mesh, varying in amount from near zero to 25 percent. A large segment of the northern section shows both the warm- and cold-side HBZ boundaries displaced toward the warm air in the half-mesh compared to the full-mesh analysis.

The reduction from full- to half-mesh relates well to the increase of intensity values, both along the warm- and cold-side boundaries of the HBZ, as expected from Chapter II.

2. Full or half mesh versus quarter mesh: Fracturing of HBZ boundaries is very evident. In addition, the HBZ intensity does not uniformly increase from the .5 to .25 grid. Apparently, grid-size

reduction much below .5 is inconsistent with portraying synoptic-scale fronts from data originally fitted to the 380 km full-mesh grid. With an initial gross temperature resolution, the reduction to .25 of the full mesh (95 km) highlights mesoscale-like variations in the derivative fields. Such detail, partly derived from numerical-finite differencing and interpolation procedures, may be considered noise here since the data at full mesh, as a function of the mass structure model, do not contain such thermal resolution.

It should be noted that some error in the relative positioning and magnitude of the numerically-analyzed fronts in Fig. 16 is due to the difficulty of locating the axes with an accuracy excelling .2 mesh length, even with the reasonably small analysis interval of 10 units of $D\bar{G}\bar{\theta}^*$.

## Summary

In summary, the results using real-atmosphere data are in general, but not specific, agreement with the simulated data experiment in Chapter II. It is evident that the resolution of the temperature data input to the $D\bar{G}\bar{\theta}^*$ program must be enhanced before reductions in grid-size much below 380 km can be effective in specifying the true width and intensity of frontal zones. Numerically-processed and analyzed thermal data, of the type utilized here, presently do not contain the detail inherent in data extracted from high quality subjective analyses.

In order to focus attention on the problem of appropriate scale and resolution for acceptable numerical frontal analysis, the next chapter considers procedures for increasing the detail of the baroclinicity

data used in the $DG\bar{\theta}^*$ computation. Highly resolved data, containing information on the mesoscale structure of the atmosphere, is readily extractable from vertical soundings of the atmosphere.

## CHAPTER IV

## EXPERIMENTS TO ENHANCE THE RESOLUTION OF BAROCLINICITY

Most of the deficiencies of the operational $DG\bar{\theta}^*$ model are due to the poor resolution of the temperature and baroclinicity fields from which $DG\bar{\theta}^*$ is computed. Frontal phenomenon, by its nature, tends toward a meso-scale structure while numerically-processed observations describe, at best, the synoptic-scale features. Therefore, some experimental effort was devoted to the problem of enhancing the resolution of HBZ analysis to a degree commensurate with the entity being analyzed.

Modifications to $DG\bar{\theta}^*$, such as Mod $DG\bar{\theta}^*$ in the last chapter, may improve the meteorological consistency of the present operational frontal model, but its merits cannot exceed the amount or scale of the information content inherent in the data tuned to a mesh size of 381 km. Thus, it is logical to look to the highly resolved significant-level radiosonde data for improving the HBZ analysis. One of the more promising experiments using detailed sounding data has its foundation in the analytical development which follows:

$$\theta = f\ (n_\theta, p), \tag{12}$$

where $\theta$ is potential temperature; p is pressure; and $n_\theta$, defined by $\vec{n}_\theta = \nabla\theta/|\nabla\theta|$, represents an axis oriented in a direction perpendicular to an isentrope on an isobaric surface. Therefore,

$$d\theta = \frac{\partial\theta}{\partial n_\theta}\,\delta n_\theta + \frac{\partial\theta}{\partial p}\,\delta p\,. \tag{13}$$

Along an isentropic surface, $d\theta = 0$, and from Eq. 13

$$G\theta \equiv \frac{\partial\theta}{\partial n_\theta} = - \frac{\partial\theta}{\partial p} \frac{\delta p}{\delta n_\theta} . \tag{14}$$

Similar to Eq. (3),

$$DG\theta \equiv - \nabla G\theta \cdot \vec{n}_\theta = - \frac{\partial^2 \theta}{\partial n_\theta^2} . \tag{15}$$

Computation of $G\theta$ and $DG\theta$

The scheme proposed here involves a unique computation of $G\theta$ from the two factors, $-\partial\theta/\partial p$ and $\delta p/\delta n_\theta$. This approach represents a considerable deviation from that used to obtain $G\theta^*$ as a function of $\theta^*$, since $G\theta$ is not derived directly from a field of $\theta$. However, $DG\theta$ is computed from $G\theta$, similar to $DG\theta^*$ from $G\theta^*$.

The Computation of $\partial\theta/\partial p$

The derivative, $\partial\theta/\partial p$, is determined for a mandatory pressure surface by a quadratic fit of potential temperature data at the mandatory level and the first significant levels above and below. Plotted soundings on a thermodynamic chart give the impression of a sequence of layers, each linear in the logarithmic pressure ordinate, with separating first-order thermal discontinuities. In reality, the discontinuities bounding these significant layers are manufactured by criteria used for processing, coding, and plotting the observed data (Danielsen, 1959). Therefore, fitting a continuous curve to the transmitted sounding for the purpose of obtaining $\partial\theta/\partial p$ is reasonable as well as necessary. Also, using a quadratic rather than a linear fit of temperature data agrees with the nature of the sounding in pressure and temperature coordinates and adequately handles the situations in which the mandatory level is also a significant level.

The mandatory-level values of $\partial\theta/\partial p$ may be obtained through the solution for constants a, b, and c in the system of three simultaneous linear equations

$$\begin{aligned} \theta_u &= a + b\,p_u + cp_u^2 \\ \theta_m &= a + b\,p_m + cp_m^2 \\ \theta_\ell &= a + b\,p_\ell + cp_\ell^2, \end{aligned} \tag{16}$$

and from

$$\left(\frac{\partial\theta}{\partial p}\right)_m = b + 2cp_m, \tag{17}$$

where $u(\ell)$ is the significant level geometrically above (below) the mandatory pressure level, m. The $\theta$s in Eq. (16) are computed from sounding values of pressure and temperature by

$$\frac{\theta}{T} = \left(\frac{1000}{p}\right)^{\frac{R_d}{c_p}} \tag{18}$$

In order to keep the program as simple as possible in the initial feasibility experiment for computing G$\theta$, temperatures to the nearest whole deg C (accurate to .5C) were employed in computing $\partial\theta/\partial p$. This approach was partly dictated by the state of the hemispheric preprocessed radiosonde data made available by FNWC[1].

Significant layers of shallow depth (i.e., less than 10 mb) were not considered at this point in the experiment partly due to the gross temperature resolution and also because such layers may contribute intolerable error in the $\partial\theta/\partial p$ computation. Further, as an example of the inconsequence of a thin layer, consider a stable significant layer near

---

[1] Since the data input to FNWC's data-processing system excludes significant level information, it was necessary to write a complex program to couple significant and mandatory level data at the preprocessed stage. The program was written by Lieutenant R. C. Schiffner, Department of Meteorology and Oceanography, Naval Postgraduate School, Monterey, California.

700 mb of 10 mb thickness (approximately 400 feet) and 100 miles in horizontal width. The slope of this layer, $\delta z/\delta n$, is 1/1320. Horizontally wider and vertically thinner stable layers result in still smaller slopes and concomitant negligible baroclinicities along the pressure surface. Thus, HBZs of such dimensions may be profitably omitted from the frontal analysis, at least in this first attempt at computing $G\theta$.

The Computation of $\delta p/\delta n$

Unlike $\partial\theta/\partial p$, the computation of the slope of the isentropic surface, $\delta p/\delta n_\theta$, at each station was accomplished within the framework of FNWC's data processing and analysis system. Thus, $\theta^*$ was substituted for $\theta$ in Eq. (14). Available to the project were FNWC's numerically-computed fields of pressure for each $\theta^*$ surface at 2.5C intervals. From these fields, slopes of the isentropic surfaces, $|(\delta p/\delta n)\ \vec{n}_p| = \delta p/\delta n_p$, were computed by manual means. Here, $\vec{n}_p$ is the unit vector normal to isobars on the isentropic surface. However, $|(\delta p/\delta n)\ \vec{n}_{\theta^*}| = \delta p/\delta n_{\theta^*}$, the form of the slope factor in Eq. (14), represents only that component of $\delta p/\delta n_p$ which lies in the direction of $\nabla\theta^*$ on the isobaric surface. Since the angles between the vectors $\vec{n}_p$ and $\vec{n}_{\theta^*}$ were found to be < 15 deg for nearly all of the radiosonde data used, the difference in the two quantities is negligible (i.e., generally < 3.5 percent in this particular experiment). In fact, overestimating $\delta p/\delta n_{\theta^*}$ by using $\delta p/\delta n_p$ in Eq. (14) is considered desirable in view of the smoothing inherent in the numerically-processed products. Moreover, $\delta p/\delta n_{\theta^*}$ was computed for that isentropic surface whose magnitude is divisible by 2.5 and greater than $\theta^*$ at the mandatory level for which the

computations are being made. For example, $\delta p/\delta n_{\theta*}$, for a station with $\theta*$ = 301K at 850 mb, was computed at the $\theta*$ surface of 302.5K. Undoubtedly some fiction was introduced into the computed $G\theta$ by this simplified and hybrid combination of $\partial\theta/\partial p$ and $\delta p/\delta n_{\theta*}$. However, in the realm of a feasibility study such lack of homogeneity and detail may be tolerated, and, overall, may be desirable as will be discussed in a later section.

Although the ultimate goal is to improve upon the operational $DG\theta*$ model for frontal analyses, the emphasis here is on its predecessor, the baroclinicity, whose properties largely determine the validity and usefulness of the HBZ analysis. Thus, the discussion at hand will concentrate on the enhancement of the field of baroclinicity as generated by the introduction of the vertical resolution inherent in significant-level radiosonde data.

The gross scheme just outlined for computing $G\theta$ and its attendant field of $DG\theta$ will be symbolized as $G\theta'$ and $DG\theta'$ to distinguish it from subsequent experiments which more closely approximate the true resolution of $G\theta$ and $DG\theta$. The test date is the same one used to exemplify the $G\theta*$ and $DG\theta*$ computations, namely 0000 GMT 6 March 1966.

## $G\theta'$ and its Comparison to $G\theta*$

In order to establish continuity with the discussion in Chapter III and present a base to which $G\theta'$ may be compared, the numerically-analyzed 850 mb $G\theta*$ for 0000 GMT 6 March 1966 (Fig. 17a) is discussed first. The analysis area is confined to North America and the middle and high latitude portions of the adjacent ocean areas from Europe to 180 deg long. The positive $DG\theta*$ axes closely parallel baroclinicity


Fig. 17. 850 mb, 0000 GMT 6 March 1966.

a. $G\theta^*$: interval 1 C $(100\ km)^{-1}$, starting with 1 unit. $G\theta^*$ axes: heavy dashed lines; $G\theta'$ axes: light dashed lines; $DG\theta^*$ axes $> 5 \times 10^{-2}$ C $(100\ km)^{-2}$: xxx; areas where $G\theta^* < 1$ C $(100\ km)^{-1}$: shaded.

b. $G\theta'$, subjectively analyzed: interval as in a; $G\theta'$ axes: heavy dashed lines. Areas where $G\theta' < 1$ C $(100\ km)^{-1}$: shaded.

magnitudes of 1C (100 km)$^{-1}$, being on the weaker- (stronger-) gradient side for the less (more) intense HBZs. An example of the former (latter) may be noted in the middle (western) North Atlantic area. Baroclinic regions in which $\theta^*$ gradients are less than 1C (100 km)$^{-1}$ are of little interest but such gradients do occur along the DG$\theta^*$ axes. This is especially true for low-latitude ocean areas. Note the North Atlantic region south of 30N. The halfwidth of HBZ zones may be noted on Fig. 17a by the transverse distance from the DG$\theta^*$ to G$\theta^*$ axes. Average magnitude of the halfwidth is 2.5 deg lat.

Fig. 17b shows the numerically computed G$\theta'$ field, manually-analyzed in this version. About 40 percent of the North American area shows G$\theta'$ less than 1C (100 km)$^{-1}$ in the same area. Seven radiosonde stations yield G$\theta'$ values greater than 3C (100 km)$^{-1}$, with an absolute magnitude of 8.1C (100 km)$^{-1}$ in southwest Canada, while only two G$\theta^*$ grid-point values exceed three units of baroclinicity.

Table 7 statistically indicates the increased focus of baroclinicity using the significant-level radiosonde data from 118 stations in the area of analysis on Fig. 17b. The table shows the number of stations in each of nine categories of $\Delta G\theta = G\theta' - G\theta^*$. The category "-.19 to +.19" may be considered as $\Delta G\theta \approx 0$. HBZs are arbitrarily defined as the areas having G$\theta'$ values $\geq$ 1C (100 km)$^{-1}$. For such areas, G$\theta' > G\theta^*$ in the vast majority of cases (85 percent), while in subbaroclinic regions (SBZ), where G$\theta' <$ 1C (100 km)$^{-1}$, G$\theta' <$ G$\theta^*$ almost without exception (98 percent). This attests to the greater range of G$\theta'$ relative to G$\theta^*$, and especially to the reduction of baroclinicity in the subbaroclinic areas on the G$\theta'$ chart. Stated another way, the relative barotropic areas are more barotropic

while the relative baroclinic areas are more baroclinic in the $G\theta'$ as compared to the $G\theta^*$ fields.

Table 7. 850 mb $\Delta G\theta$ (= $G\theta'$ - $G\theta^*$), 0000 GMT 6 March 1966, summarized for 118 radiosonde stations (North America and adjacent ocean areas). HBZ = stations where $G\theta' \geq 1C\ (100\ km)^{-1}$; SBZ = stations where $G\theta' < 1C\ (100\ km)^{-1}$. Stations with absolute instability omitted.

| $\Delta G\theta$ (C [100 km]$^{-1}$) | Number of radiosonde stations | |
|---|---|---|
| | HBZ | SBZ |
| $\geq +2.00$ | 4 | - |
| +1.00 to +1.99 | 5 | - |
| +.60 to +.99 | 5 | 1 |
| +.20 to +.59 | 14 | 0 |
| -.19 to +.19 | 13 | 10 |
| -.20 to -.59 | 4 | 20 |
| -.60 to -.99 | 1 | 13 |
| -1.00 to -1.99 | 0 | 26 |
| $\leq -2.00$ | 0 | 2 |

The major axes have similar orientation on both the $G\theta^*$ and $G\theta'$ charts, but those on the latter are generally displaced to the cold side of their counterparts on the former. Note the situation over eastern United States and the adjacent Atlantic and the zone running northwest-southeast from Alaska to central United States. These relations between $G\theta'$ and $G\theta^*$ (Fig. 12 and Table 7), suggest that the nature of the $G\theta'$ computations reduces the broadening effect as compared to $G\theta^*$. However,

an extra impetus to this effect may be due to the manner in which the slopes of isentropic surfaces ($\delta p/\delta n_{\theta*}$) were computed. That is, using the "higher $\theta$* divisible by 2.5K" for computing $\delta p/\delta n_{\theta*}$ has the effect of moving the hyperbaroclinic zones toward the cold air from their true positions.

It is also noted that detail along the G$\theta$' axes (eastern United States and southwest Canada) is greater than that of G$\theta$*. Secondary HBZs are both more evident and intense on the G$\theta$' analysis as seen on Fig. 17b over east central United States and southeast Canada. The mountainous regions are problem areas on both the G$\theta$* and G$\theta$' models; the two analyses differ markedly here. However, occluded structure, as shown by NMC over northwest United States and southwest Canada (Fig. 12), is indicated weakly with reasonable orientation in the G$\theta$' but not in the G$\theta$* fields.

There still remain many problems in obtaining a suitable field of baroclinicity at any level, especially at low tropospheric levels. In the present experiment, the G$\theta$' computation becomes invalid for the dry adiabatic case, that is for $\partial\theta/\partial p = 0$ and $\delta p/\delta n_{\theta*} = \infty$. Also, the present mode of computing G$\theta$' is unrealistic for the occasional case of superadiabatic conditions ($\partial\theta/\partial p$ positive) in the observed sounding since this stability condition cannot exist in the numerically-processed data from which the $\delta p/\delta n_{\theta*}$ values were generated. Four such superadiabatic values occurred over the North American area for the synoptic time under experiment. This frequency would be greater, except that for such anomalous cases temperatures to the nearest .2C (vice 1C) were used in computing $\partial\theta/\partial p$. Teletype data transmissions were the source of such detailed temperature data.

DG$\theta$' and its
Comparison to DG$\theta$*

To advance the experiment to the point of obtaining a DG$\theta$' field for comparison to its counterpart, DG$\theta$*, the G$\theta$' data were objectively analyzed. Several G$\theta$' guess fields were considered. Even over a dense data area like the United States, a "flat" guess, as G$\theta$' = 0, yields a numerical G$\theta$' analysis with a tendency for circular isolines due to localized points of large baroclinicity. Some improvement in shaping the field to elliptical rather than circular isolines is achieved by using the well-behaved G$\theta$* field as first guess to the G$\theta$' analysis. Using this method, Fig. 18 shows a manual trace of the resulting 850 mb objectively-analyzed G$\theta$' field. The reduction of resolution in G$\theta$'-objective compared to G$\theta$'-subjective (Fig. 17b) is obvious. Also, differences in the positions of the axes of the two fields give a further measure of the role of objective analysis in misplacing the associated HBZ boundaries, a subject which came under discussion in Chapter II.

The quantity DG$\theta$' ($\equiv -\nabla G\theta' \cdot n_{\theta^*}$) was computed next. The $\theta$* field was used to generate the directional second derivative since a suitable numerical analysis of $\theta$' was not readily available.

Fig. 19 shows the DG$\theta$* and DG$\theta$' numerical analyses, similar to Fig. 17 for G$\theta$* and G$\theta$'. In general, the comments concerning the baroclinicity fields carry over to the interpretation of Fig. 19. Due to the close proximity of G$\theta$' baroclinic zones over the southeastern United States, the nearly meridional DG$\theta$' axis along the east coast is disrupted. This is an undesirable feature in view of the conventional-front positions for this time.

Also note that the axis of maximum baroclinicity in the G$\theta$' and G$\theta$* fields do not necessarily lie along their zero-isoline counterparts in the DG$\theta$' and DG$\theta$* patterns, respectively, as expected from the discussion in Chapter III. The phenomenon is of significance only for complex HBZ structures which occur near the edges of dense data areas or in mountainous regions. The detailed G$\theta$', DG$\theta$' analyses are more susceptible than G$\theta$*, DG$\theta$* to this numerical problem, as noted over Mexico and the adjacent Gulf of Mexico (Fig. 19).

Fig. 20 gives a measure of the positions of the HBZ boundaries from the DG$\theta$' and DG$\theta$* models relative to subjectively-analyzed 850 mb NMC and Canadian fronts. DG$\theta$' excels in detail and in apparently reducing HBZ broadening by placing fronts on the cold-air side of the DG$\theta$* positions. However, the DG$\theta$* fronts compare very favorably with the hand-analyzed versions in the matter of spatial continuity, especially over the western Atlantic Ocean.

700 mb data and fields were handled in the same way as 850 mb and the results show similar merits and deficiencies. The vertical consistency of objective fronts from DG$\theta$' excels that from DG$\theta$*, as noted in Fig. 21. Improper frontal slopes (i.e., 700 mb positions on the warm-air side of 850 mb positions) are more prevalent in the DG$\theta$* than in the DG$\theta$' patterns. The vertical consistency of DG$\theta$* fronts is illustrated and discussed further in Chapter V.

Before advancing the G$\theta$ experiment (Eqs. 12-18) in order to obtain a greater measure of accuracy and resolution in the baroclinicity fields, it is to be emphasized that the difference in detail between the G$\theta$' and G$\theta$* fields is derived from the computation of $\partial\theta/\partial p$ from significant-level

Fig. 18. 850 mb $G\theta'$, 0000 GMT 6 March 1966, objectively analyzed. Interval: 1 C $(100\ km)^{-1}$. Axes: heavy dashed lines. Subjectively-analyzed $G\theta'$ axis, from Fig. 17b shown as light dashed lines.

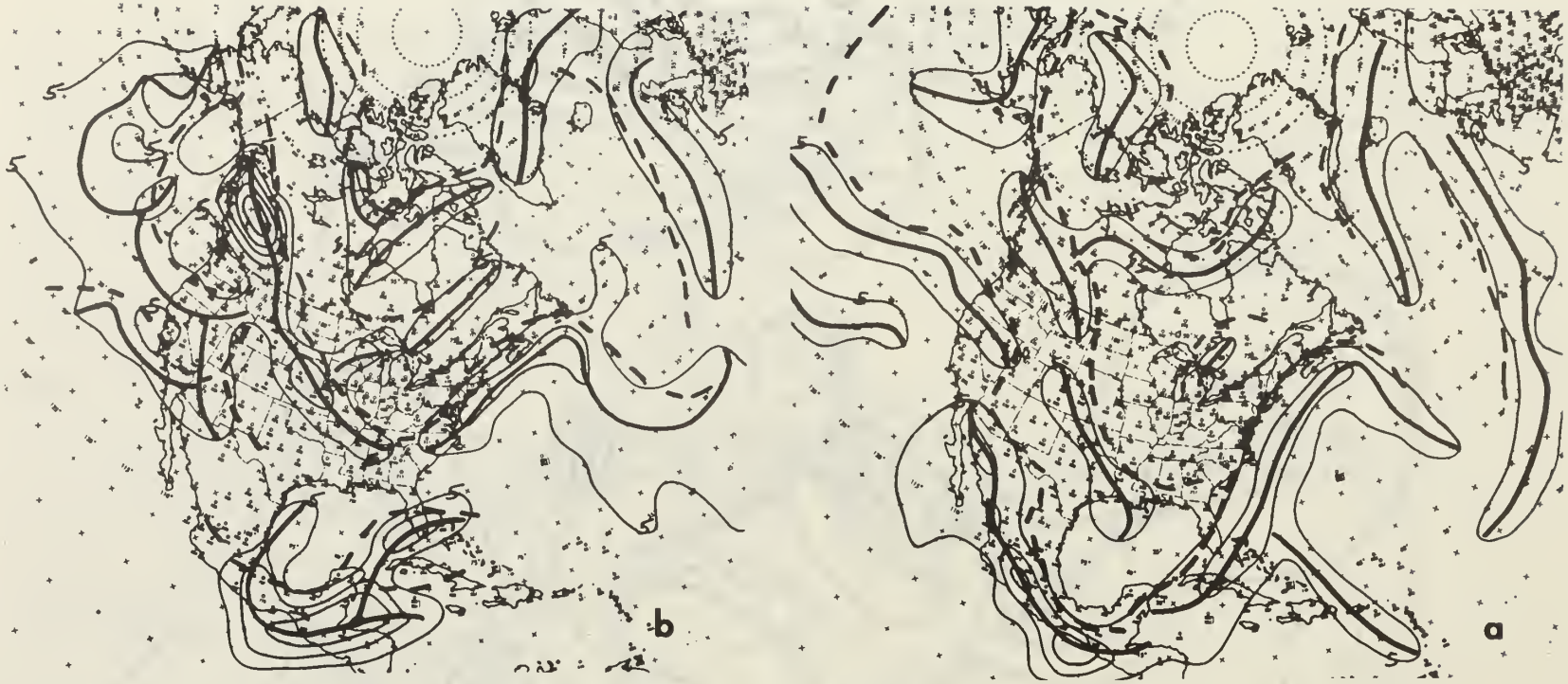


Fig. 19. 850 mb, 0000 GMT 6 March 1966.
a. $DG\theta^*$: interval $20 \times 10^{-2}$ C $(100\ km)^{-2}$, starting with 5 units. $DG\theta^*$ axes: solid lines. $G\theta^*$ axes from Fig. 17a: dashed lines.
b. $DG\theta'$: interval as in a. $DG\theta'$ axes: solid lines. $G\theta'$ axes from Fig. 18: dashed lines.

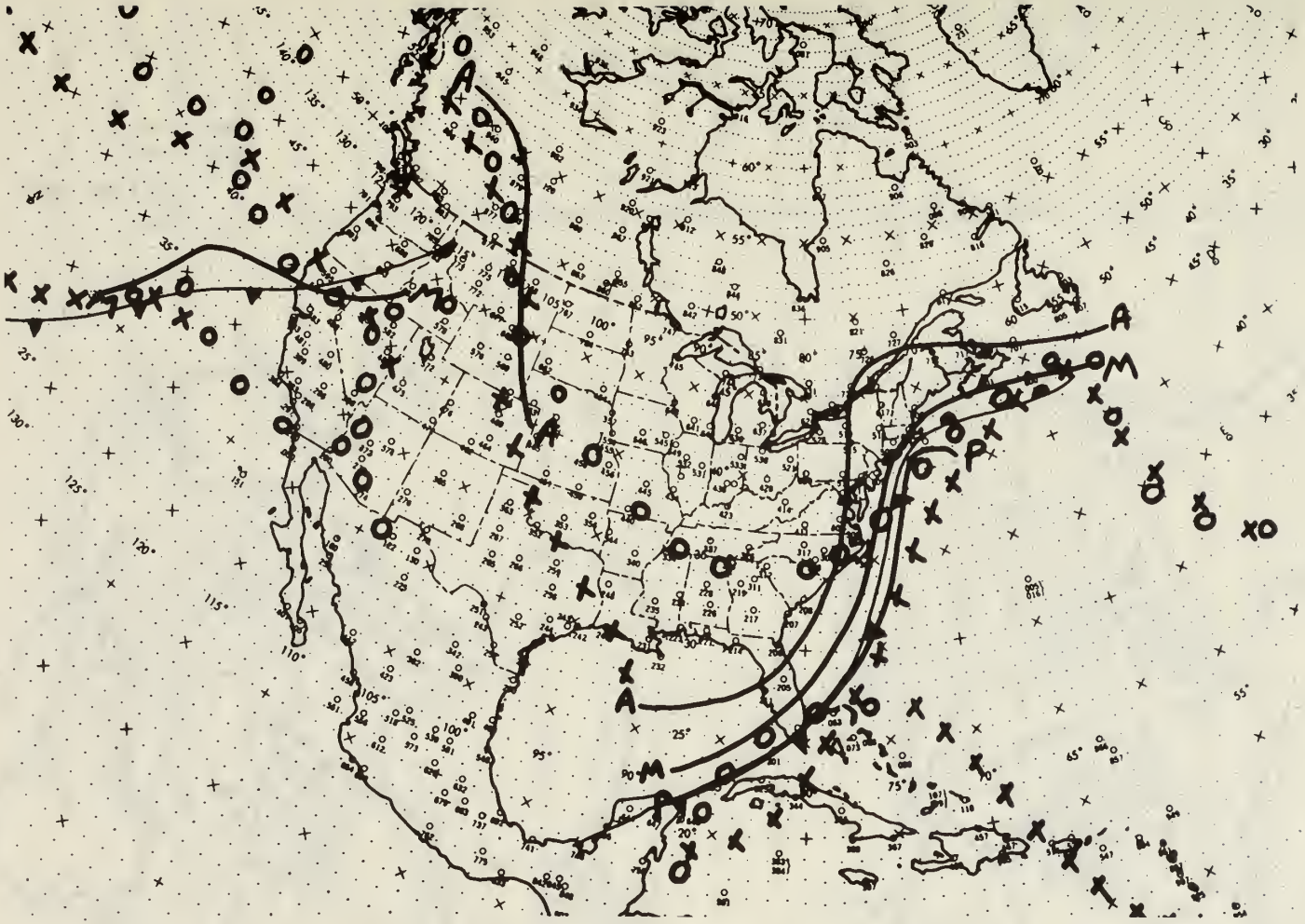

Fig. 20. 850 mb fronts, 0000 GMT 6 March 1966. NMC: conventional symbols; CAO, Canada: light solid lines (A = arctic, M = maritime, P = polar); DGθ*: xxxx; DGθ': oooo.

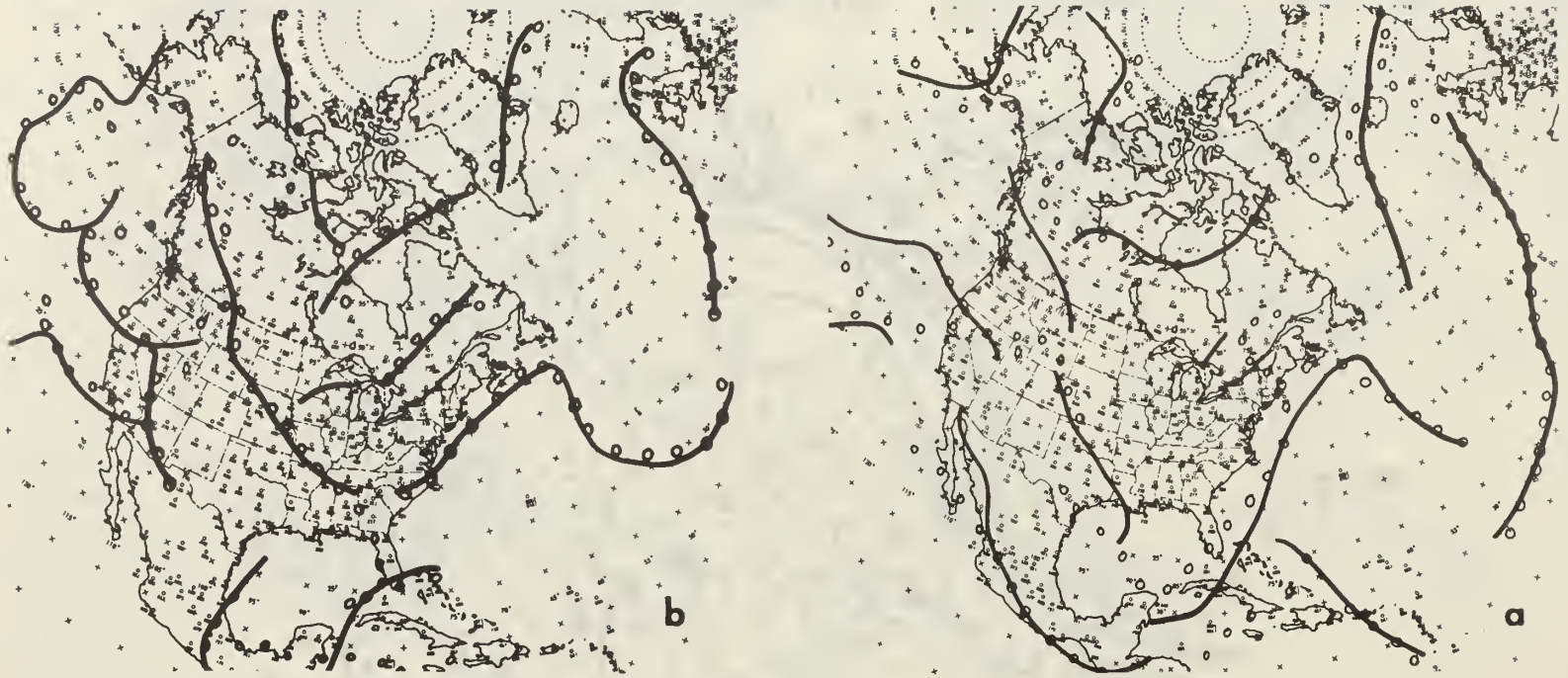


Fig. 21. HBZ boundaries (warm-air side only), 0000 GMT 6 March 1966: 850 mb (——), 700 mb (000).

a. DGθ*

b. DGθ'

radiosonde date (Eq. 14). The influence of the $\theta^*$ field is retained by substituting $\delta p/\delta n_{\theta^*}$ for $\delta p/\delta n_{\theta}$ in Eq. (14) and $\vec{n}_{\theta^*}$ for $\vec{n}_{\theta}$ in Eq. (15).

Recomputation of $G\theta$ with Certain Approximations Removed

The previous section may be regarded as a successful feasibility experiment in obtaining a field of baroclinicity whose detailed structure excels that of $G\theta^*$ due to the vertical resolution involved in the computation of $\partial\theta/\partial p$. Utility of the derived $G\theta'$ and $DG\theta'$ is evident even though (1) error-prone unchecked real-time radiosonde transmissions were used to obtain $\partial\theta/\partial p$, (2) temperatures from such soundings were rounded to the nearest whole degree Centigrade, and (3) $\delta p/\delta n_{\theta^*}$, at the mandatory level, was computed from numerically-processed data at a $\theta^*$ surface whose value exceeded that at 850 mb by as much as 2.4C.

Before proceeding to an extension of this experiment involving the enhancement of baroclinicity resolution by an increase in data density, it is well to remove several of the gross approximations inherent in the computations to this point. For this purpose, the data for 850 mb, 0000 GMT 6 March 1966, were further manipulated. Due to the basic importance of $G\theta$ to the frontal parameter, $DG\theta$, only the former is in focus here. Concentration of effort is on the dense-data areas of the United States, Canada, and the surrounding ocean areas.

For this second and improved approximation to $G\theta$ (hereafter symbolized as $G\theta'_c$) checked radiosonde data were used. The National Weather Records Center, Asheville, North Carolina (NWRC, 1966) recomputes most soundings using both machine and manual processing. Among other things, the radiosonde data, as originally recorded, are checked for

proper evaluation and inconsistencies of mandatory-level data as evidenced by analyzed charts; also, derived height, temperature, moisture, and wind data are recomputed for 50 mb intervals as well as the significant levels.[1] Such checking often results in soundings differing considerably from the transmitted version in both significant and mandatory temperature information. And, of course, both checked and transmitted soundings differ from the original recording and any systematic smoothing of same (Danielsen, 1959).

In view of the increased accuracy of the checked data compared to the transmitted soundings, the arbitrarily imposed accuracy of 1C in temperature and the 10 mb criterion for significant layers were removed. The following criteria were substituted in computing the baroclinicity parameter, $G\theta'_c$. To compute $\partial\theta/\partial p$ at 850 mb, temperature data were recorded to the nearest .1C from 850 mb and the first significant levels above and below 850 mb. If such significant levels extended more than 50 mb beyond the 850 mb level, then the 800 mb and 900 mb level data were used to formulate $\partial\theta/\partial p$.

Use of the FNWC processed-data fields was maintained for computing the slope of the isentropic surfaces in Eq. (14). However, the slopes at each station were obtained from a more exacting differentiation scheme made available by Meteorology International (Holl, 1966). As noted in Chapters II and III, the derivatives used in the DGΘ* program were computed from the Lagrangian five-point differentiation formula for centered differences (Eq. [8]), which does not use the datum at the grid point of

[1] The elaborate set of computerized checking procedures, called the Significant-Level Punched Card Audit, was made available to the writer by the NWRC.

computation. In Meteorology International's program, derivatives are computed from a 16-point 4 x 4 array of grid-point data with the computation point at its centrum. The program is a scheme which minimizes smoothing of the gradient values and weights heavily the influence of the immediate surrounding grid points as compared to the Lagrangian computations employed in the DG$\theta$* model. Further, for each radiosonde station, $\delta p/\delta n_{\theta*}$ was interpolated for the 850 mb $\theta$*, accurate to .1C.

A subjective analysis of the 850 mb $G\theta^{*\prime}_{c}$ data is shown in Fig. 22. The pattern should be compared with those of $G\theta'$ and $G\theta^*$ in Fig. 17. In comparison with $G\theta'$, $G\theta'_c$ shows only a slight (about 10 percent) reduction in the subbaroclinic area but the stations having baroclinicity magnitudes $\geq$ 3C (100 km)$^{-1}$ have increased to twelve in number. These figures agree in principle with a sampling of data from those radiosonde stations for which there exists both $G\theta'$ and $G\theta'_c$ values; namely, 63 percent of the HBZ baroclinicities have increased while only 36 percent of the SBZ values have decreased from $G\theta'$ to $G\theta'_c$. The absolute high magnitude of $G\theta'_c$ is 21.30 C (100 km)$^{-1}$ at station 879 in southwest Canada, thus increasing considerably the range of $G\theta'_c$ relative to $G\theta'$.

Similar to $G\theta'$ versus $G\theta^*$ (Table 7), $G\theta'_c$ gives more focus or resolution than $G\theta^*$ (Table 8) with 82 percent of the HBZ values increasing and 89 percent of the SBZ values decreasing from the $G\theta^*$ to the $G\theta'_c$ computations. It is to be noted that there is a 25 percent increase in comparative data points in Table 8 over that in Table 7.

There are some important differences in the patterns of $G\theta'$ and $G\theta'_c$. The most significant of these occur over the southwest and southeast

Fig. 22. 850 mb $G\theta'_c$, 0000 GMT 6 March 1966. Interval: geometric, with r = 2; units: C $(100\ km)^{-1}$. $G\theta'_c$ axes: heavy dashed lines. $G\theta'$ axes (from Fig. 17): light dashed lines. U plotted at stations for which $\partial\theta/\partial p$ is positive.

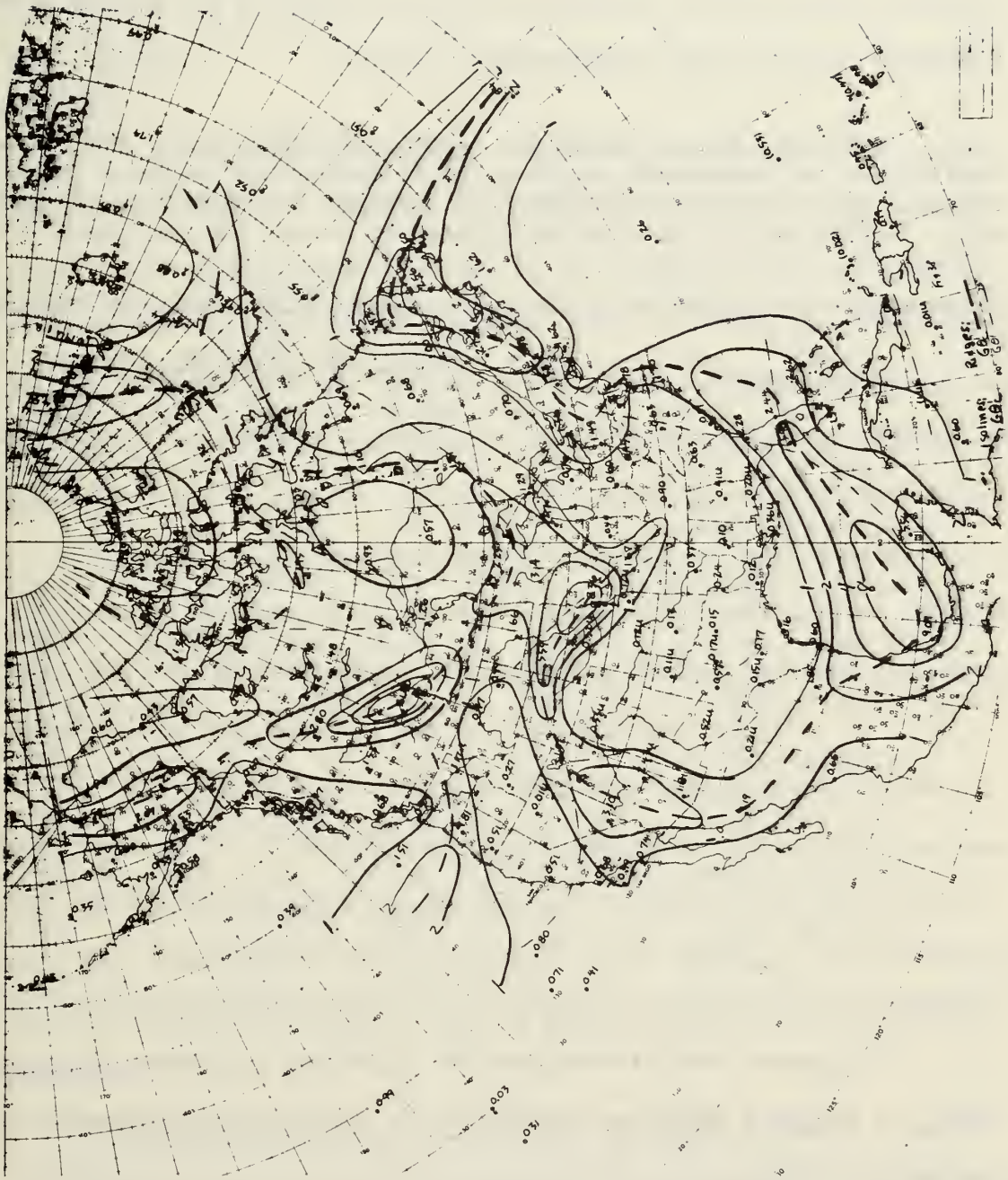

United States, the former associated with orographic effects, the latter with a synoptic-scale frontal structure whose complexity is exemplified by the Canadian analysis in Fig. 20. Repositioning of the axis of maximum baroclinicity in eastern and central Canada is also apparent. There can be little question from Fig. 22 that the accuracy and resolution of the radiosonde data are important factors in locating the axes of baroclinicity and hence the hyperbaroclinic zones.

Table 8. 850 mb $\Delta G\theta'(= G\theta'_c - G\theta^*)$, 0000 GMT 6 March 1966, summarized for 147 radiosonde stations (North America and adjacent ocean areas). HBZ = stations where $G\theta'_c \geq 1C\ (100\ km)^{-1}$; SBZ = stations where $G\theta'_c < 1C\ (100\ km)^{-1}$. Stations with absolute instability omitted.

| $\Delta G\theta'$ (C [100 km]$^{-1}$) | Number of radiosonde stations | |
|---|---|---|
| | HBZ | SBZ |
| $\geq +2.00$ | 9 | - |
| +1.00 to +1.99 | 6 | - |
| +.60 to +.99 | 9 | 0 |
| +.20 to +.59 | 17 | 5 |
| -.19 to +.19 | 16 | 34 |
| -.20 to -.59 | 7 | 23 |
| -.60 to -.99 | 1 | 6 |
| -1.00 to -1.99 | 1 | 12 |
| $\leq -2.00$ | 0 | 1 |

In general, $G\theta'_c$ differs from $G\theta'$ by virtue of greater accuracy and detail in computed $\partial\theta/\partial p$ and a reduction of smoothing and increase in accuracy of $\delta p/\delta n_{\theta^*}$.

Many problems still remain. Nine radiosonde stations, labeled "U" on Fig. 22, indicate absolute instability in the layer within 50 mb of 850 mb. Thus $\delta p/\delta n_{\theta*}$, as derived from FNWC's mass structure model, is in error at these stations. A potentially greater problem, which encompasses the absolute instability difficulty, is the validity of $\delta p/\delta n_{\theta*}$ in combination with $\partial\theta/\partial p$.

## Cross-section Analyses

A cross-section analysis, extending from station 78367 (Guantanamo Bay, Cuba) to 72655 (St. Cloud, Minnesota) is used as another means of exemplifying the relation of baroclinicity from numerically-processed and checked radiosonde data. Fig. 23 shows the former, with $\theta*$ data plotted at 50 mb intervals, while Fig. 24 shows the latter, with $\theta$ computed from NWRC's Northern Hemisphere data tabulations (1966) using Eq. (18). In the case of station 78367, significant-level data were taken from the real-time transmitted sounding, as checked data were not available. The mixture of checked and unchecked data is justified for this station since mandatory level data on the two versions are nearly identical, a fact not true for all radiosonde stations.

The subject cross-sections, oriented approximately in the direction of $\nabla\theta*$ at 850 mb, are quite interesting for several reasons. The sections intersect a complex frontal structure over the Florida area (see Figs. 20 and 22), extend from a near maximum to a near minimum in 850 mb temperatures (Fig. 10), and pass through a relatively dense data area.

Contrary to the expectation that $\theta*$ should exceed $\theta$, nearly 40 percent of the area from the surface to 600 mb shows $\theta > \theta*$, in some

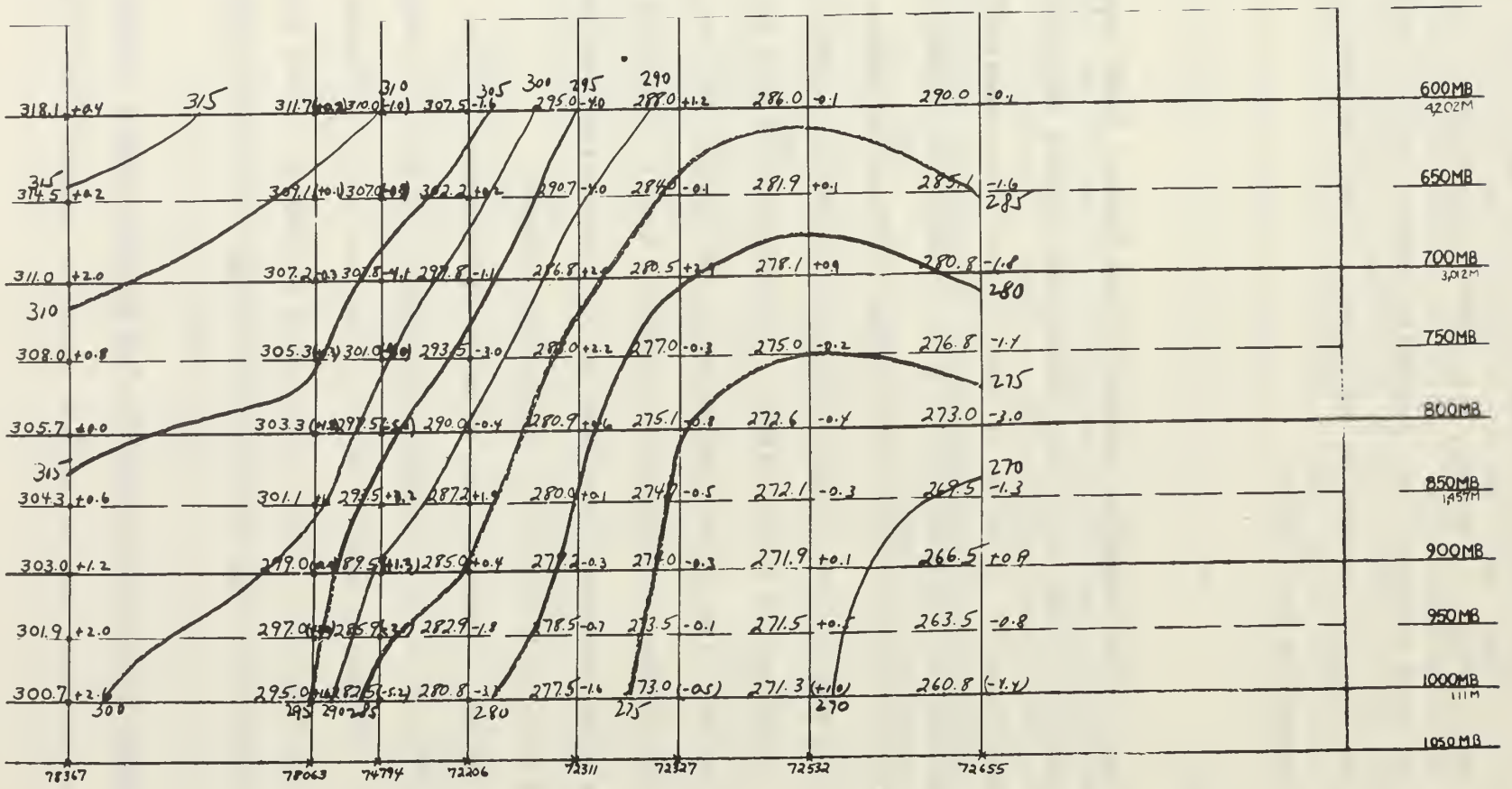


Fig. 23. Vertical cross-section from 78367 to 72655 at 0000 GMT 6 March 1966. θ* (K) plotted to left, computed from reconstructed soundings of FNWC numerically-processed mandatory level data. Isoline interval: 5 K. θ* - θ (K) plotted to right; (θ* - θ) indicates values estimated from analysis.

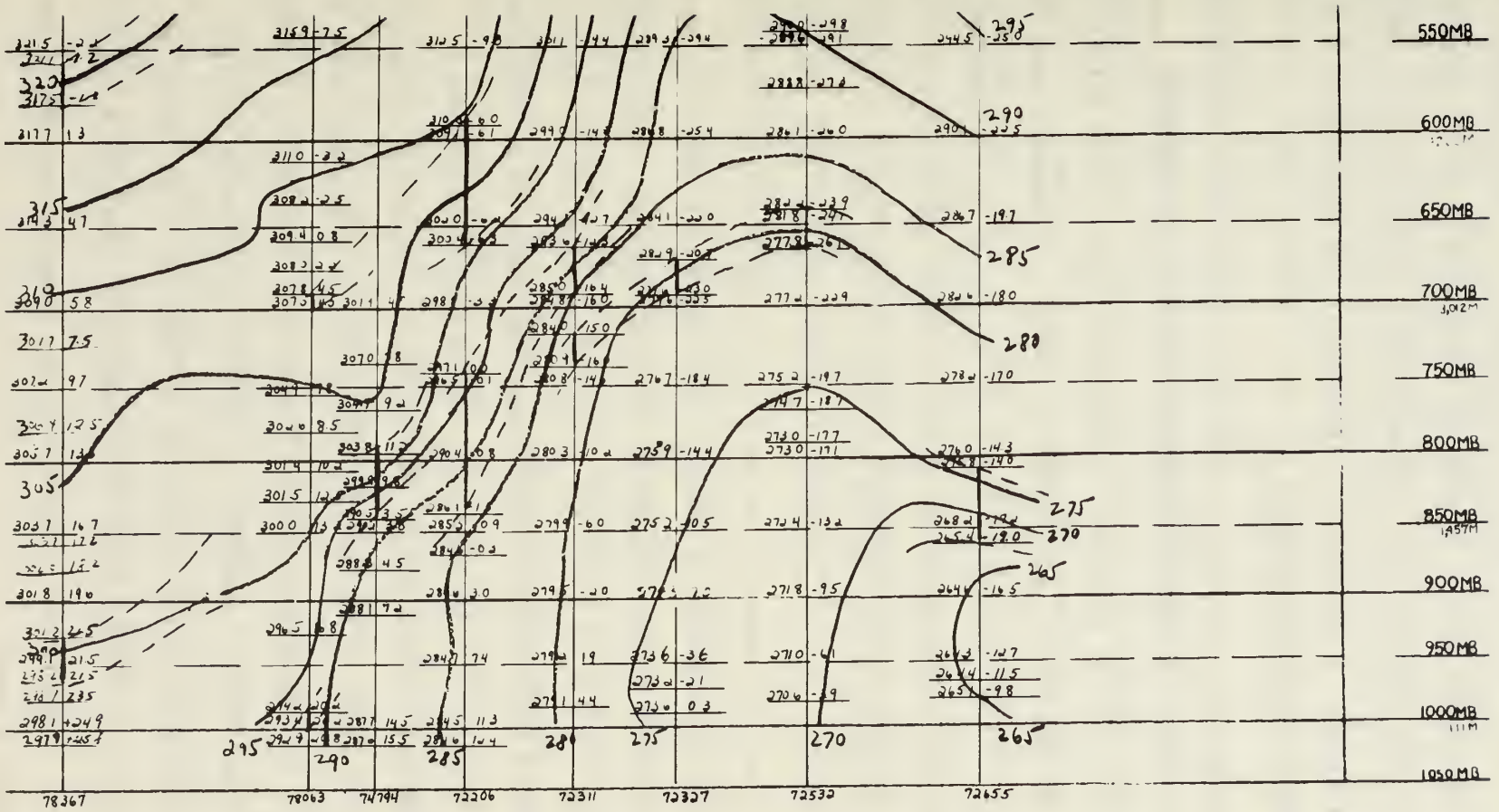


Fig. 24. Vertical cross-section from 78367 to 72655, 0000 GMT 6 March 1966. θ (K) plotted to left, and T (C) plotted to right, computed from checked radiosonde data (except 72367). θ isoline interval: 5 K. Stable layer ($-\partial T/\partial z < 0$) boundaries: dashed lines.

cases (station 74794, at 1000 mb) by as much as 5C. The situation is similar at the 850 mb level. Generally, $\theta^*$ exceeds $\theta$ in the relatively warm, moist areas adjacent to the frontal zones, while in other areas $\theta$ is greater than $\theta^*$. To assist in this analysis the quantity $\theta^* - \theta$ is plotted at 50 mb intervals in Fig. 23.

Although the major axis of warm and cold air have similar locations on the two versions, detail on stability (from station 78367 at lower levels to 72327 at 650 mb) and positions of the minor thermal axes differ markedly in pattern (as 900-650 mb, from 78367 to 72206). It appears that isentropic slopes on the numerical version are excessive in stable areas (which would lead to excessive $G\theta_c'$ values in HBZs) and deficient in or near actual unstable areas (leading to deficient $G\theta_c'$ values in subbaroclinic and unstable layers), relative to slopes derived from the checked radiosonde data. The former is to be noted in the vicinity of the sloping stable layer(s) equatorward of station 72311 while the latter is obvious at the near-surface levels throughout the cross section. The situation at low levels (notably at 72327 and 72655) also serves as an example of the inability of the numerical-data-processing scheme to specify the location of absolutely unstable layers in the actual atmosphere.

Broadening effects due to the numerical processing of data are quite obvious in Fig. 23 within and either side of the major zones of hyperstability and hyperbaroclinicity, especially from 850 mb to 700 mb between 78063 and 72311. However, the reverse is somewhat true geometrically below 900 mb from just south of 78063 to 74794, where $\theta^*$ exceeds $\theta$ (moisture effect) while $\theta^*$ is generally less than $\theta$ north of 78063. This is a propitious circumstance for locating the HBZ in the numerical field of data.

It is of interest to seek further quantitative comparison of the isentropic slope values since the mass-structure version of this factor, $\delta p/\delta n_{\theta *}$, is retained in computing $G\theta'_c$. Table 9 shows the calculated 850 mb slopes at each station as derived from the two cross-sections as well as those $\delta p/\delta n_{\theta *}$ generated from the numerically-processed data fields and used to compute $G\theta'_c$ in Fig. 22.

Measurements of $\delta p/\delta n$ and Baroclinicity--850 mb point slopes of isentropic surfaces from the cross sections of analyzed processed data (Fig. 23) and checked radiosonde data (Fig. 24), and average slopes used in computing $G\theta'$ (Fig. 17b) and $G\theta'_c$ (Fig. 22), are compared for the six stations from 78063 to 72532 in Table 9. The range of isentropic slopes is greatest from the point slope computations made from the cross-sections. Beyond that, clear cut differences do not exist between the various values of $\delta p/\delta n$.

The $\delta p/\delta n$ values may be combined with $\partial\theta/\partial p$ computed from the checked data to produce the baroclinicities, $G\theta$, shown in Table 9. The pattern of $G\theta$s associated with the isentropic point slope measurements from the cross-section in Fig. 24 agree with the complex doublet of HBZs between stations 72206 and 78367. Such is not indicated in the other versions of $G\theta$ in Table 9. Somewhat disturbing is the relative maximum of $G\theta$ in the vicinity of 72327 for all four $G\theta$s. Since this feature is largely due to the steep isentropic slope, the $G\theta$ version which reduces its significance is most desirable. Overall, as expected, real data vice processed data and point-slope vice average-slope calculations yield a $G\theta$ picture closest to the mesoscale nature of HBZs.

Table 9. 850 mb $\delta p/\delta n$ (mb[100 km]$^{-1}$) 0000 GMT 6 March 1966: Computations of point and average values for stations 78063 to 72532 in cross-sections of Figs. 23 and 24. $G\theta^*s$ (C[100 km]$^{-1}$) computed from tabular values of $\delta p/\delta n$ and $\partial\theta/\partial p$ computed from checked radiosonde data.

| Station | Point slope from cross-section | | Average slope numerically computed from | |
|---|---|---|---|---|
| | Checked data (Fig. 24) | Processed data (Fig. 23) | Met. Intl. Program | Lagrangian 5-point formula |
| | | $\delta p/\delta n$ | | |
| 78063 | 48.5 | 28.5 | 41.0 | 28.0 |
| 74794 | 21.0 | 44.0 | 49.0 | -- |
| 72206 | 27.0 | 62.0 | 45.0 | 35.0 |
| 72311 | 104.0 | 90.0 | 75.0 | 52.0 |
| 72327 | 64.0 | 150.0 | 60.0 | 72.0 |
| 72532 | 36.0 | 25.5 | 36.0 | 20.0 |
| | | $G\theta$ | | |
| 78063 | 3.1 | 1.8 | 2.6 | 1.8 |
| 74794 | 1.0 | 2.2 | 2.4 | -- |
| 72206 | 1.4 | 3.2 | 2.3 | 1.8 |
| 72311 | 0.9 | 0.8 | 0.6 | 0.4 |
| 72327 | 1.0 | 2.2 | 0.9 | 1.1 |
| 72532 | 0.4 | 0.3 | 0.4 | 0.2 |

The resolution of baroclinicity is advanced one more step in the next section where the detail and accuracy of the analysis is increased by a scheme of extrapolating significant-layer $G\theta$ data to the 850 mb level at points between the locations of radiosonde stations.

## Gθ Extrapolations

The increased resolution of the field of $G\theta'_c$, as compared to $G\theta'$, is due to the computation scheme and nature of the data; the data density is essentially the same for both. The average distance between radiosonde stations is close to 5 deg lat over dense data areas and much larger than this over ocean areas, thus limiting the enhancement of detail in the analysis of baroclinicity for any Gθ computation scheme. A partial solution to the data problem is made possible by an extrapolation technique which has its basis in the thermodynamics and synoptics of the vertical structure of HBZs. It is well recognized that a hyperbaroclinic zone of significance is generally associated with a relatively stable layer of air in which $\partial\theta/\partial p$ is negative and large. Vertical cross-sections, oriented approximately along $\nabla\theta$ on an isobaric surface, show such layers extending over atmospheric depths of several thousand feet and distances of hundreds of miles with boundaries identified by an isentrope or a small range of isentropes (Saucier, 1955). That stability and, consequently, baroclinicity have considerable uniformity in a particular stable layer may be seen from the cross section previously discussed (Fig. 24).

Based on this general background, selected layers above and below a mandatory pressure surface have been examined for stability ($\partial\theta/\partial p$) and isentropic slope ($\delta p/\delta n$) for the purpose of extrapolating baroclinicity data to the mandatory level at locations between the radiosonde stations. In this way, the vertically-resolved temperature data contribute further to the detail of the baroclinicity analysis. The specifics of the extrapolation procedure finally adopted are outlined below. Application is made to the 850 mb level, 0000 GMT 6 March 1966.

$\partial\theta/\partial p$--Extrapolations are derived from radiosonde data between 700 and 950 mb only. $\partial\theta/\partial p$ is computed at 900, 800, and 750 mb, using a quadratic fit of checked radiosonde temperature data. For each of the three levels, data points are selected for the level and 50 mb below and above unless an intervening significant level is available. For example, to compute $\partial\theta/\partial p$ at 900 mb, $\theta$s at 950, 900, and 850 mb are used if significant levels are absent between 950 and 850 mb. If significant levels existed at 920 and 855 mb, then data at the 920, 900, and 855 mb levels are used in the $\partial\theta/\partial p$ computation. Such a procedure obtains three extrapolations for each radiosonde station (unless station pressure $<$ 950 mb) and controls the layer from which the extrapolations are derived (i.e., from approximately 2500 feet below to 5000 feet above 850 mb). Due to the complexity of localized stable layers near the ground, the use of data in the low troposphere below the 850 mb level must be limited. A less arbitrary system could set the lower-level limit at 50 mb above the earth's surface, vice a fixed 950 mb, thereby handling data in mountain and flat areas in similar fashion.

$\delta\rho/\delta n$--Similar to the previous application of Eq. (14), this parameter is computed as $\delta p/\delta n_{\theta *}$ at 900, 800, and 750 mb.

$G\theta''_c$--The product of $\partial\theta/\partial p$ and $\delta p/\delta n_{\theta *}$ is symbolized as $G\theta''_c$ for the cases of data computed at $P \gtrless 850$ mb. The computed $G\theta''_c$ values are extrapolated to 850 mb along the $\theta *$ surface intersecting the point of computation at pressure level P (i.e., 900, 800, and 750 mb) and in a direction along the 850 mb $\nabla\theta *$.

It is to be noted that the system adopted here extrapolates baroclinicity to 850 mb rather than simply extrapolating stability,

$\partial\theta/\partial p$, along the isentropic surface. One reason is that the accuracy of $G\theta''_c$, using a $\delta p/\delta n_{\theta*}$ computed at $P \gtrless 850$ mb for the known position of the radiosonde station, is better than that obtained from use of $\delta p/\delta n_{\theta*}$ at an estimated position of $\theta*$ at 850 mb.

A considerable amount of manual manipulation of data was necessary in the extrapolation phase of the project since this aspect was handled as a feasibility study. Although $\partial\theta/\partial p$ was numerically computed at $P \gtrless 850$ mb from checked radiosonde data, the $\theta*$ appropriate to the $\delta p/\delta n_{\theta*}$ computation was determined manually from P, $\theta*$ soundings reconstructed from numerical grid prints of P ($\theta*$) at 2.5K intervals. Accuracy of interpolated $\theta*$ is considered to be $\pm$ .3K. For values of $\theta*$ at 900, 800, and 750 mb, the isentropic slopes were interpolated.

## Analysis of Combined $G\theta'_c$ and $G\theta''_c$ Data

Fig. 25 represents an analysis of the combined baroclinicity extrapolations from 900, 800, and 750 mb to 850 mb and the $G\theta'_c$ computations at 850 mb, the latter analyzed in Fig. 22. The extrapolations are plotted to the nearest .1 C $(100 \text{ km})^{-1}$ to distinguish them from the 850 mb data plotted to the nearest .01 C $(100 \text{ km})^{-1}$. Since the atmosphere is constrained to be statically stable in the numerically-processed data (Chapter III) used for $\delta p/\delta n_{\theta*}$, the 900 (800 and 750) mb extrapolations always appear on the cold-air (warm-air) side of each radiosonde station. For a few stations, as 72365, 72485, and 72576, extrapolation data only exist since station pressures are less than 850 mb. The extrapolation data are particularly helpful in areas where the algebraic sign of 850 mb $\partial\theta/\partial p$ is positive (absolute instability cases, plotted as U), as for stations 72232 and 72374.

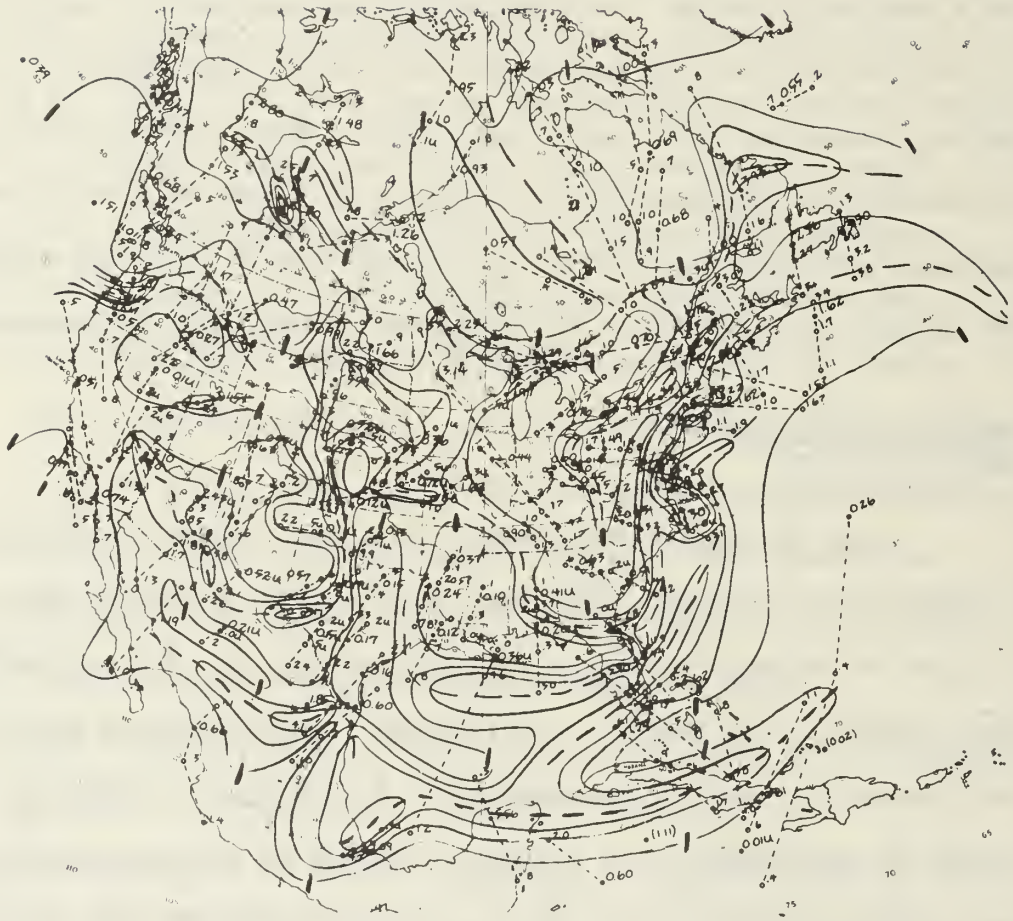

Fig. 25. 850 mb $G\theta'_c$ and $G\theta''_c$ extrapolations, 0000 GMT 6 March 1966. Analysis interval: geometric, with r = 2; units: C $(100\ km)^{-1}$. Axes: dashed lines. 850 mb $G\theta'_c$ data (radiosonde-station circles shaded) plotted to nearest .01; extrapolation data, $G\theta''_c$, (location circles not shaded) plotted to nearest .1. U indicates $\partial\theta/\partial p$ is positive; 850 mb and extrapolated data for each station connected by light dashed line.

Slopes of the isentropic surfaces ($\delta p/\delta n_{\theta^*}$) are indicated by the distances of the $G\theta''_c$ extrapolations from the parent radiosonde station. These distances correlate inversely with the magnitude of $G\theta''_c$. As an example, compare extrapolations for 78016 and 72206; the latter (former) indicates nearly vertical (horizontal) isentropes and relatively high (low) baroclinicities. Validity of a baroclinicity computation decreases with increasing distance from the radiosonde station (i.e., decreasing isentropic slope).

Extrapolations were not plotted for stations where the $\theta^*$ surface at $P \gtrless 850$ mb could not be located at the 850 mb level or where $\nabla\theta^*$ at 850 mb changed by 180 degrees between the station and its associated extrapolation point. For example, this situation occurred at 72867 (76255) for the 900 (750) mb extrapolation. A $\theta^*$ of 268.0K (309.8K) did not exist at 850 mb. For this study all the extrapolations (except those indicated with a question mark) were held to be valid and used in the analysis. The resulting mesoscale detail in Fig. 25 may be questioned. Perhaps those extrapolation points separated from the parent radiosonde station by a baroclinicity axis should be given minimal weight in the analysis. The same approach may be appropriate for data associated with nearly horizontal isentropic surfaces and isolated points of excessive high and low $G\theta''_c$ values. Subjective computations and use of the hybrid mixture of $\theta^*$ and $\theta$ information very likely inflates the baroclinicity magnitudes in the relatively stable layers but deflates these values in the layers with instability, as noted from a discussion of Figs. 23 and 24.

In general, the number of baroclinicity axes from $G\theta''_c$ and $G\theta'_c$ data combined have doubled compared to $G\theta'_c$ alone. This relation between the two fields is much like that occurring in a comparison of flight and radiosonde data for the purpose of locating the jet-stream axis. Each synoptic-scale jet axis may be reconstructed into a multiple number of splinter axes by increased resolution of the observational data.

Although the analyses over the eastern United States-western North Atlantic region appears complicated it is similar in interpretation to the detailed Canadian CAO frontal analysis shown in Fig. 20. For instance, the CAO analysis shows 850 mb arctic, maritime, and polar fronts distinguishable over the Florida Peninsula. These frontal entities are in much the same position on Fig. 25. For the remainder of eastern North America, the comparison in number of CAO and numerical HBZs is good, but the positions of these zones differ.

The profiles of 850 mb baroclinicity between stations 78367 and 72655 on Figs. 24 and 25 are quite comparable, except near 78367. A complex system of hyperbaroclinicity between stations 78063 and 72206 is found on both charts as is the axis of maximal values near 72655. Station 72532 presents a problem in correctly extrapolating data to the 850 mb level since an isentropic minimum occurs in the layer 800-700 mb very close to this station.

Over mountain areas the analysis from $G\theta'_c$ and $G\theta''_c$ combined differs sharply from that of $G\theta'_c$ or $G\theta^*$ alone. In fact, differences between any two of the manually or numerically generated baroclinicity analyses are maximized over such areas. A satisfactory solution to meaningful patterns over these regions has yet to be achieved.

## Summary

The various experiments to enhance the resolution of baroclinicity for the purpose of HBZ analysis suggest the following:

1. There is considerable baroclinicity detail inherent in the vertically-resolved significant-level radiosonde data. Such mesoscale detail cannot be retrieved from numerically-processed mandatory-level data alone.

2. Since significant-level radiosonde data (transmitted or checked) are of a meso-microscale nature, the baroclinicity values derived from them may not be compatible with the horizontally-projected synoptic-scale fields of other meteorological parameters. However, numerically tuning the baroclinicity field by use of smoothers and filters can solve this problem to any desirable degree.

3. The numerical methods and grids in current operational use for processing and analyzing meteorological data are not appropriate to the scale of baroclinicity shown in Fig. 25. For this reason, the development described in this chapter must be regarded as a second-generation model for the purpose of analyzing hyperbaroclinicity.

Next, attention is returned to the mode of HBZ analysis feasible for present-day field operations, which is described as the DG$\theta$* model in Chapter III. Considerable insight on synoptic-scale structure and behavior of fronts may be gained from a diagnosis of this model in varying space and time frames and in relation to other meteorological parameters. Thus, Chapter V concentrates on the four-dimensional continuity of HBZs, as illustrated by case studies from winter and summer periods. Chapter VI relates the HBZ analyses to weather satellite

observations of cloud and vertical motion; and, Chapter VII demonstrates the properties of time-averaged intensity and location of HBZs for a selected 30-day period in both winter and summer.

Together, the next three chapters give the synoptic meteorologist a four-dimensional view of frontal analysis not heretofore obtainable from the standard manual analysis of surface fronts only.

# CHAPTER V

## THE DGθ* MODEL: CASE STUDIES OF THE SPACE AND TIME CONTINUITY OF HYPERBAROCLINIC ZONES

### A Summer-Season Case Study

The summer-season day of 20 August 1965, with emphasis on the 0000 GMT synoptic time, was selected primarily for a study of the space continuity of the tropospheric DGθ* fields. Analyses at 1000, 850, 700, and 500 mb were considered in the substudy.

#### DGθ* Analyses at 1000, 850, 700, and 500 mb

The DGθ* operational model developed in this treatise explicitly indicates boundaries and implicitly the intensities of HBZs. In general, most meteorologists are familiar with the synoptic-scale boundaries and their vertical-plane slopes from an air-mass point of view. For instance, it is well known that, in the low-troposphere, frontal zones slope toward cold air with increasing height, with slopes generally steepest at the lowest levels. In the middle troposphere, these zones of hyperbaroclinicity become more horizontal and diffuse. However, not much is known of the intensity of HBZs, since, normally, the parameter is not displayed in a quantitative fashion on the daily operational charts.

It is the purpose of this case study to diagnose the numerically-computed boundaries of HBZs as generated from the processed virtual potential temperatures (θ*) and to relate these analyses to the previous

discussion concerning the effect of numerical processing on the location and intensity of HBZs (Chapter II).

Figs. 26-30 illustrate the DGθ* fields and related phenomena for 0000 GMT 20 August 1965. Isolines on these figures represent a manual trace of selected positive- and negative-valued lines of the numerically-produced front-location parameter.

In order to focus attention on the HBZs with spatial significance and continuity, certain criteria involving intensity and pattern were established before locating the axes in the DGθ* fields. The major criteria are as follows. (1) Analysis is limited to the area poleward of 15N. (2) Closed isolines are not drawn around single grid-point values, whatever the magnitude of DGθ*. (3) The positive and negative axes are drawn only for segments along which both associated axes are well defined; DGθ* must exceed 10 units at one or more grid points along one of the axes. (4) Axes are drawn only where DGθ* magnitudes exceed 5 units. However, such axes are connected through a DGθ* area of less than 5 units magnitude (but greater than zero) where the interval of separation is less than 2 mesh lengths, and the associated positive or negative axis is continuous using the 5-units criterion. See DGθ* analysis over northern United States on Fig. 26. (5) Axes associated with areas of circular DGθ* isolines are not drawn. See Kamchatka, northern Russia, and the southeast China coastal areas in Fig. 26. Such areas generally signify cut-off pools of cold air or complex isotherm patterns. (6) Unless a HBZ is associated with at least one grid-point Gθ* value in excess of 1 C $(100\ km)^{-1}$ the DGθ* positive and negative axes are not shown. Such is the case for many ocean and low-latitude HBZs. (7) Furthermore, axes obeying the criteria in (1) to (6) are also required to be approximately parallel although the

transverse distance separating the HBZ boundaries is of no particular limitation.

Establishing criteria of this character has as its purpose an objective separation of the significant from the insignificant synoptic-scale HBZs. This selective screening may be also accomplished on an operational basis. Frontal zones weaker than those in focus here are considered as noise; the complex zones omitted by application of criteria (1) to (7) generally involve undesirable fiction due to the numerical processing in combination with grid size and/or scale of the thermal feature.

1000 mb (Fig. 26)--The HBZs at 1000 mbs show less horizontal continuity and have more complex structure than their free-atmosphere counterparts. Features existing at 1000 mb but not found at successively higher levels, as over mountainous terrain , are of little real consequence. In general, oceanic positive and negative axes are particularly sporadic, especially so over the Pacific Ocean. The $DG\theta^*$ intensities are greatest over land. The pronounced HBZ over western North America, a persistent summer feature, is a function of the differential large scale heating either side of the land-sea interface, with some contribution from the regional trade wind inversion (Neiburger et al., 1961). Occlusions over land and ocean areas are poorly indicated as expected from discussions in Chapters II and III.

850 mb (Fig. 27)--Smoothing and reduction of segmented HBZs are evident when compared to 1000 mb. Intensity of baroclinicity change at the cold boundaries of the HBZs appears less than at warm boundaries for the non-stationary frontal zones over east continents-west oceans, as

Fig. 26. DGθ*, 1000 mb, 0000 GMT 20 August 1965. Interval: 10 x $10^{-2}$ C $(100\ km)^{-2}$, starting with the 5 isoline. + (-) DGθ* isolines: solid (dashed) lines. Warm-air (cold-air) boundaries of HBZs: heavy solid (dashed) lines.

Fig. 27. DGθ*, 850 mb, 0000 GMT 20 August 1965. Interval: 10 x $10^{-2}$ C $(100\ km)^{-2}$, starting with the 5 isoline. + (-) DGθ* isolines: solid (dashed) lines. Warm-air (cold-air) boundaries of HBZs: heavy solid (dashed) lines.

expected from the analysis in Chapter II. The quasi-stationary pattern due to differential heating over western North America is still evident at 850 mb.

700 mb (Fig. 28)--More extensive and continuous fronts prevail at 700 mb compared to lower levels. Reorientation of baroclinicity on the North American west coast indicates the surface-induced thermal structure does not exist at this level. HBZ boundary values generally show an increase from lower levels, especially over ocean areas.

500 mb (Fig. 29)--Operational use of frontal zones at levels geometrically above 700 mb is practically non-existent due to the concentration on low-level air-mass structure. However, 500 mb frontal phenomena do exist, as evident from Fig. 29. This level shows latitudinally extensive and intense HBZs which take on the appearance of spiraling hemispheric-scale jet axes (Riehl, Alaka, Jordan, and Renard, 1954). Many of these zones do not have apparent counterparts at the lower levels. Previous authors have noted a similar relation between the synoptic-scale HBZs of the lower and upper troposphere, as well as the relative importance of the latter to movement and development of tropospheric weather systems (Sanders, 1967).

## Vertical Continuity of HBZ Boundaries

The positions of the warm-side boundaries of the HBZs at the five levels, 1000, 850, 700, 500, and 300 mb, have been included here to emphasize the status of vertical continuity in the operational $DG\theta^*$ model (Fig. 30). The frontal contours that lie over the eastern United States, Canada, the northern Atlantic, and northwestern Europe areas are internally consistent.

Fig. 28. DGθ*, 700 mb, 0000 GMT 20 August 1965. Interval: 10 x $10^{-2}$ C $(100\ km)^{-2}$, starting with the 5 isoline. + (-) DGθ* isolines: solid (dashed) lines. Warm-air (cold-air) boundaries of HBZs: heavy solid (dashed) lines.

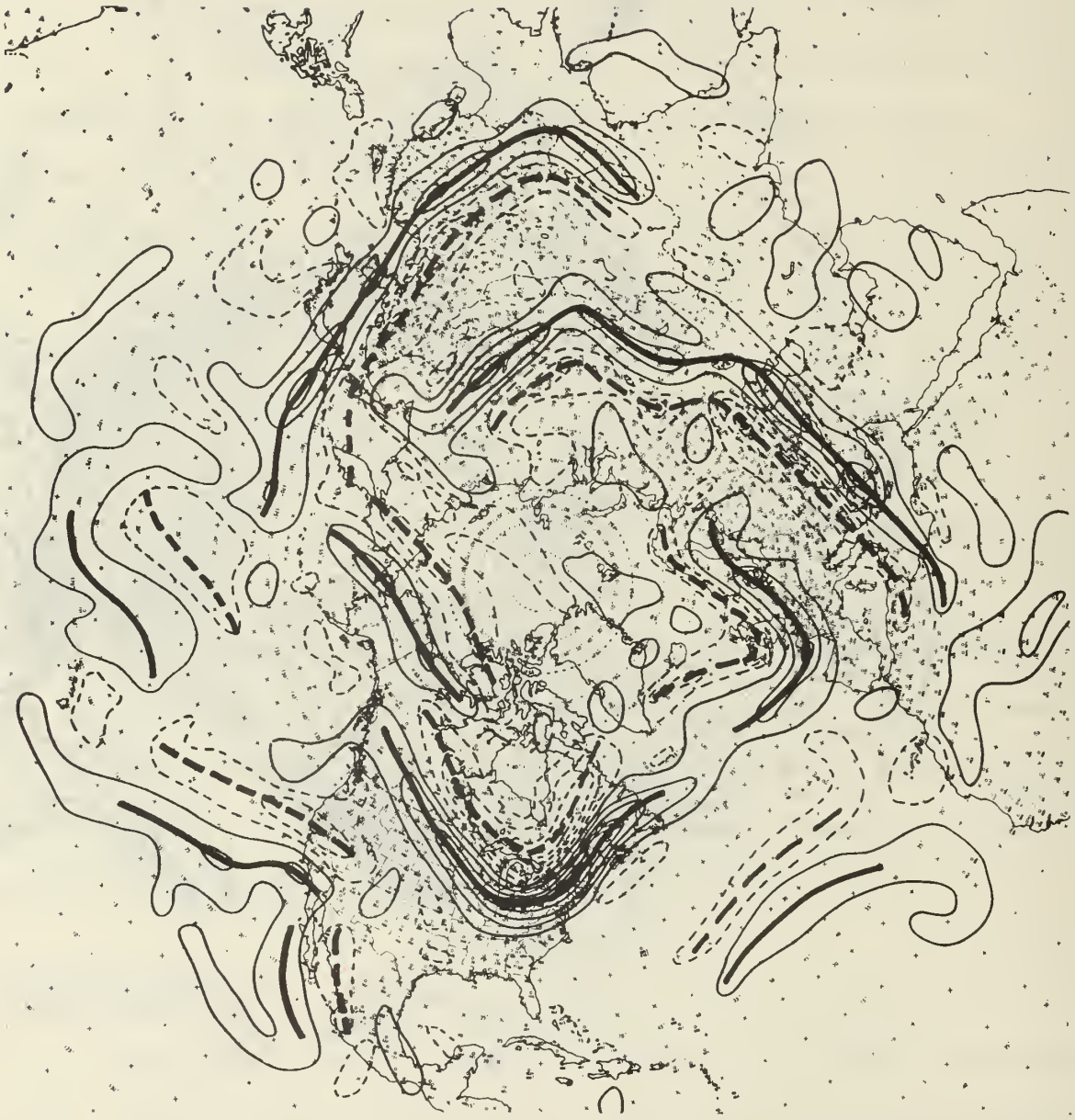

Fig. 29. DGΘ*, 500 mb, 0000 GMT 20 August 1965. Interval: 10 x $10^{-2}$ C $(100\ km)^{-2}$, starting with the 5 isoline. + (-) DGΘ* isolines: solid (dashed) lines. Warm-air (cold-air) boundaries of HRZs: heavy solid (dashed) lines.

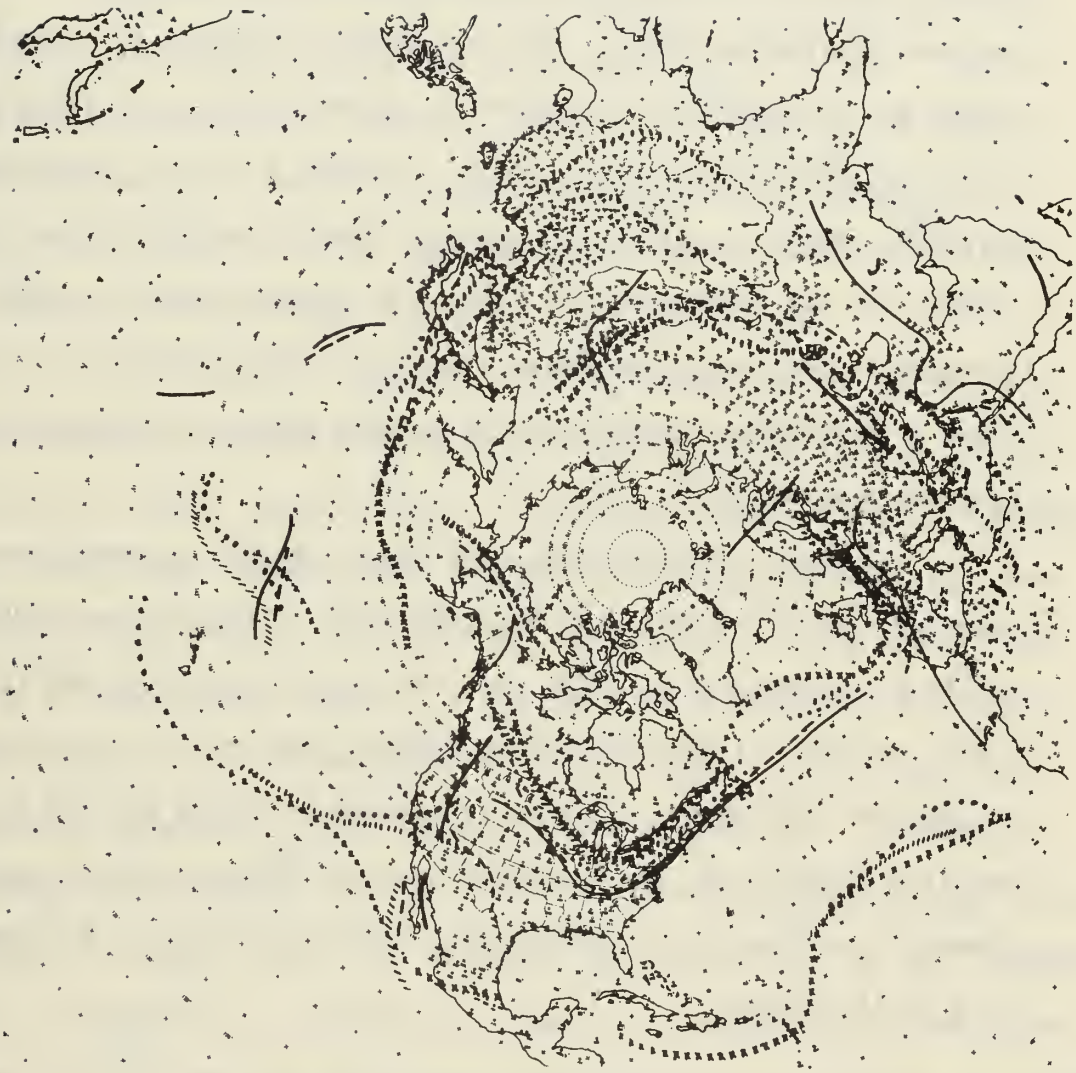

Fig. 30. Vertical continuity of positive DGΘ* axes, 0000 GMT 20 August 1965. 1000 mb: ——; 850 mb: ---; 700 mb: ···; 500 mb: ///: 300 mb: xxx.

Thus, slopes appear most logical for those frontal zones which are not tied to orographic features and where data are ample. Removal of 1000 mb fronts would result in further improvement in vertical consistency, particularly over Asia. The weak low-level fronts over oceans have poorest spatial continuity, as manifested by HBZs tilting toward warm air with increasing height. With reference to Chapter II, improper slopes may be expected for HBZs which intensify with increasing height, since the relative broadening effect increases with the frontal-zone strength. However, distinctly separate upper-troposphere fronts may account for the seemingly poor continuity between upper and lower troposphere over the ocean areas. Moreover, the liklihood of tropopause intersections with the 300 mb surface further complicates the continuity shown in Fig. 30.

Although not shown here, the front-location parameter was computed from the objectively-analyzed field of unprocessed observed dry-bulb temperatures at 1000, 850, 700, and 500 mb, 0000 GMT 20 August 1965. Maximum differences existed between DG$\theta$* and the dry-bulb version at 1000 mb. Negligible differences existed at 500 mb and 700 mb. It was also evident that the smoothing inherent in numerically-processed $\theta$* somewhat compensates for the potentially greater range of $\theta$* compared to $\theta$ at all levels.

## A Winter-Season Case Study

This section considers vertical consistency and time continuity of numerical frontal analysis for the winter period 1200 GMT 25 January to 0000 GMT 28 January 1967. As before, 1000, 850, 700, and 500 mb levels are subjected to the diagnosis. In this case the area is limited

to the North American section of the Northern Hemisphere equatorward of 55N latitude, in order that conclusions be drawn from evidence in dense-data areas only.

HBZ Boundaries in
Vertical Cross Section

The medium of presentation used here is largely that of the vertical cross section depicting HBZ boundaries in the layer 1000 to 500 mb, as derived from mandatory pressure-level analyses of $\theta^*$ and $DG\theta^*$ information. For this series, consideration was given only to those HBZs marked by six or more grid-point values of $DG\theta^* \geq 5 \times 10^{-2}$ C $(100 \text{ km})^{-2}$, at least one of which $\geq 15$ units.

Fig. 31 shows a schematic 1000 mb frontal contour as an aid in identifying the locations of the cross-section groups in Figs. 32-34. Nineteen vertical cross sections, intersecting areas adjacent to developing frontal-wave cyclones over central and eastern United States, were selected for analysis. The sections are categorized into groups; each group is homogeneous relative to the position of the apex of a frontal-wave cyclone and the movement of the surface front. Both cold- and warm-side boundaries of the HBZs are shown in each case. Boundaries tilting to the left (i.e., toward cold air) with increasing height have positive or normal slope. $\theta^*$ values at HBZ boundaries, for each mandatory level considered, are also shown. Some of the quantitative conclusions which may be drawn from this sample of nineteen cross sections are shown in Table 10 and discussed in the following paragraphs.

HBZ Width--Sawyer (1955), interpreting British flight data taken at levels ranging from 1,600 to 20,000 feet, indicates that the widths of

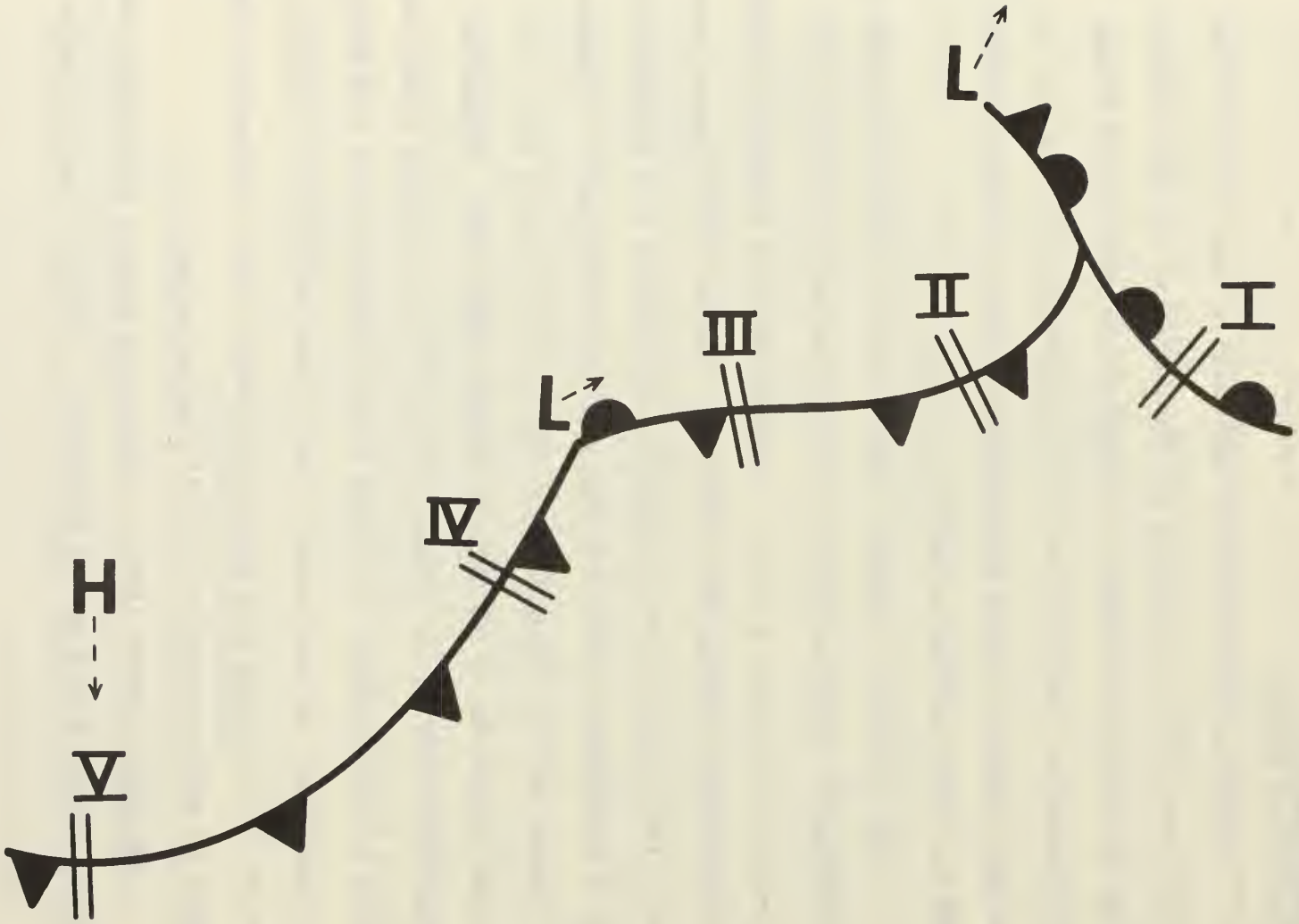


Fig. 31. Schematic 1000 mb frontal contour with associated locations of cross-section groups in Figs. 32, 33, and 34.

frontal zones average 115 n mi, with a contrast of 5 C (i.e., 2.5 C [deg lat]$^{-1}$), closely matching the N profile in Fig. 3. However, if radiosonde data are used to determine the air-mass contrasts for the same times as the twenty observation flights then the average width becomes 525 n mi, with a contrast of 8 C (i.e.,.9 C [deg lat]$^{-1}$), similar to the W profile. Expressed as a range, Sawyer's frontal-zone widths vary from 50 to 225 n mi. More recently, Danielsen has shown analyses of frontal zones over the western United States, derived partly from middle- and high-troposphere flight data in support of Project Springfield (Danielsen, 1964). Baroclinicity magnitudes computed from Danielsen's selectively-sampled stable zones above 2,000 feet fall in the range 12 C (80 n mi)$^{-1}$ (i.e., 9 C [deg lat]$^{-1}$) to 1.5 C (40 n mi)$^{-1}$ (i.e., 2.2 C [deg lat]$^{-1}$). Such flight-data values generally exceed those of the hypothetical profiles of Fig. 3, which were designed to be typical of baroclinicities diagnosed from a constant-pressure analysis of radiosonde data, as indicated below.

The numerically-analyzed HBZ widths in the January 1967 cross sections average close to 400 n mi, increasing slightly with increasing height. Average HBZ intensity decreases with increasing height from 3.5 C (deg lat)$^{-1}$ at 1000 mb to 1.6 C (deg lat)$^{-1}$ at 500 mb, thus ranging from the N to M profiles in Fig. 3. As expected, most of the associated $D_{G\theta}^{*}$ values at both the warm-side and cold-side boundaries of the HBZs also decrease with increasing height, specifically in 77 percent of the cases up to 700 mb. Such vertical gradients of baroclinicity in the low troposphere agree with the generally-held concept of frontal zones over continental areas.

Fig. 32. Vertical cross sections showing profiles of HBZ boundaries, with associated $\theta^*$ (K) values at mandatory levels. Normal distance between boundaries, $\Delta n$ (deg lat).

Group I (2 sections): Location: approximately 5 deg lat east of occluded wave apex.
Movement: geostrophically as a warm front, actually as a very slow-moving cold front.

Group II (4 sections): Location: approximately 5 deg lat west of occluded wave apex.
Movement: slow-moving cold front.

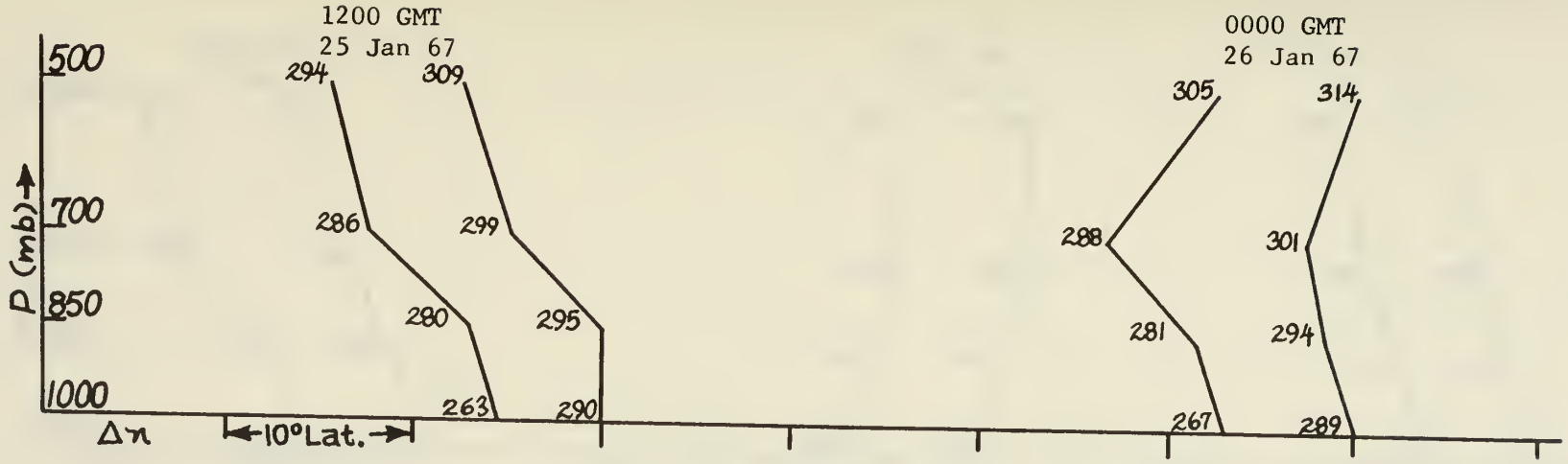


Group I

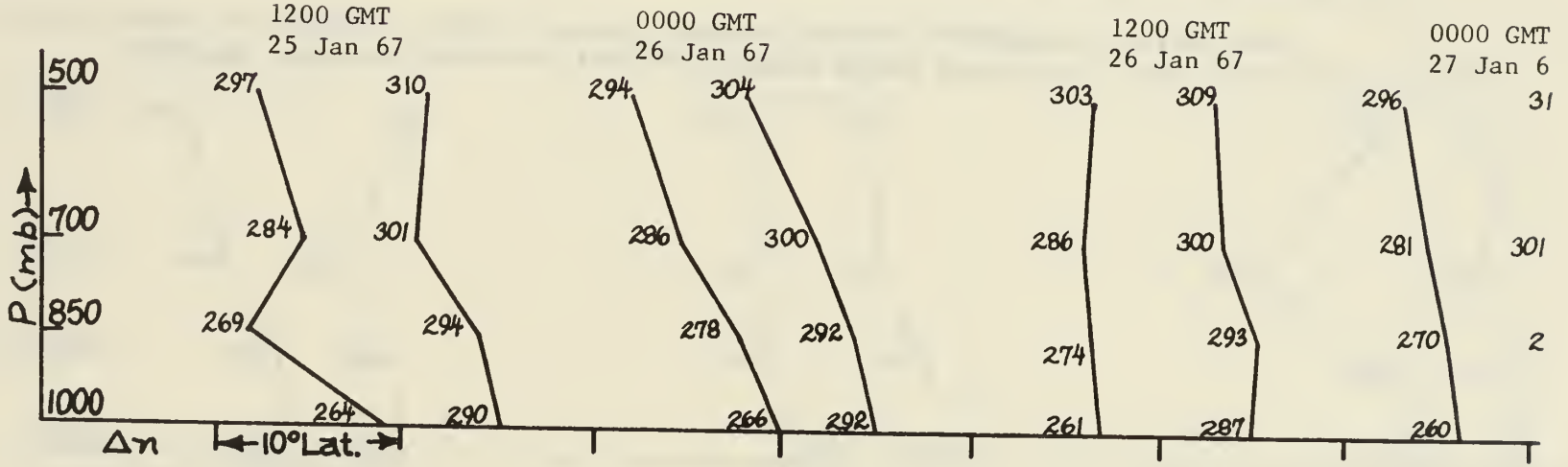


Group II

Fig. 33. Vertical cross sections of profiles of HBZ boundaries, with associated $\theta^*$ (K) values at mandatory levels. Normal distance between boundaries, $\Delta n$ (deg lat).

Group III (6 sections): Location: approximately 5 deg lat east of developing frontal-wave cyclone.
Movement: cold front through 0000 GMT 27 January 1966; warm front thereafter.

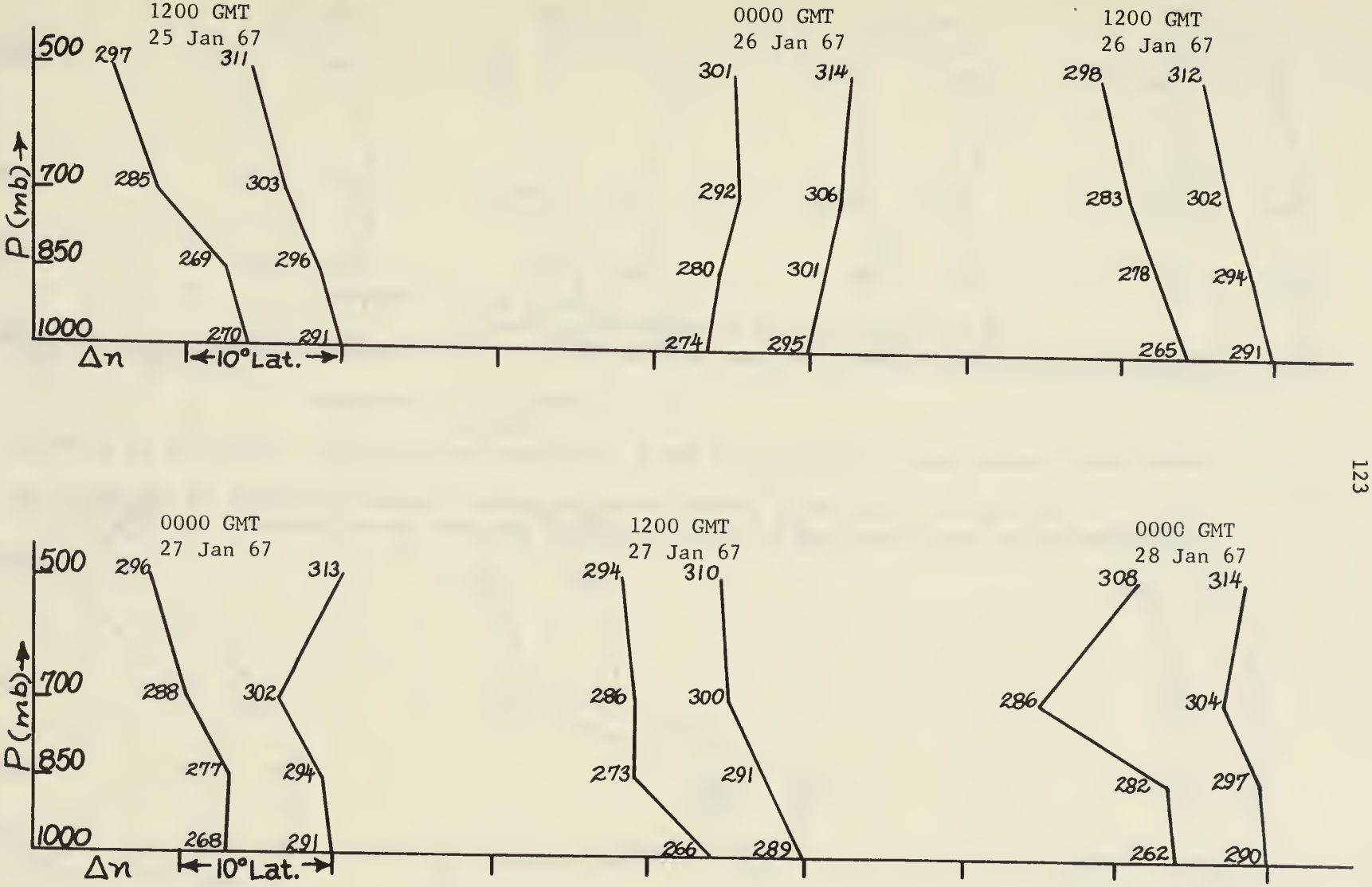
1200 GMT
25 Jan 67
0000 GMT
26 Jan 67
1200 GMT
26 Jan 67
0000 GMT
27 Jan 67
1200 GMT
27 Jan 67
0000 GMT
28 Jan 67
500
700
850
1000
P (mb)
Δn
10° Lat.
297
311
285
303
269
296
270
291
301
314
292
306
280
301
274
295
298
312
283
302
278
294
265
291
296
313
288
302
277
294
268
291
294
310
286
300
273
291
266
289
308
314
286
304
282
297
262
290

Group III

Fig. 34. Vertical cross sections showing profiles of HBZ boundaries, with associated $\theta^*$ (K) values at mandatory levels. Normal distance between boundaries, $\Delta n$ (deg lat).

| | | |
|---|---|---|
| Group IV (4 sections): | Location: | approximately 5 deg lat upstream of developing frontal-wave cyclone. |
| | Movement: | cold front. |
| Group V (3 sections): | Location: | immediately west of low-level cold-air injection and about 15 deg lat upstream of sections in Group IV. |
| | Movement: | cold front. |

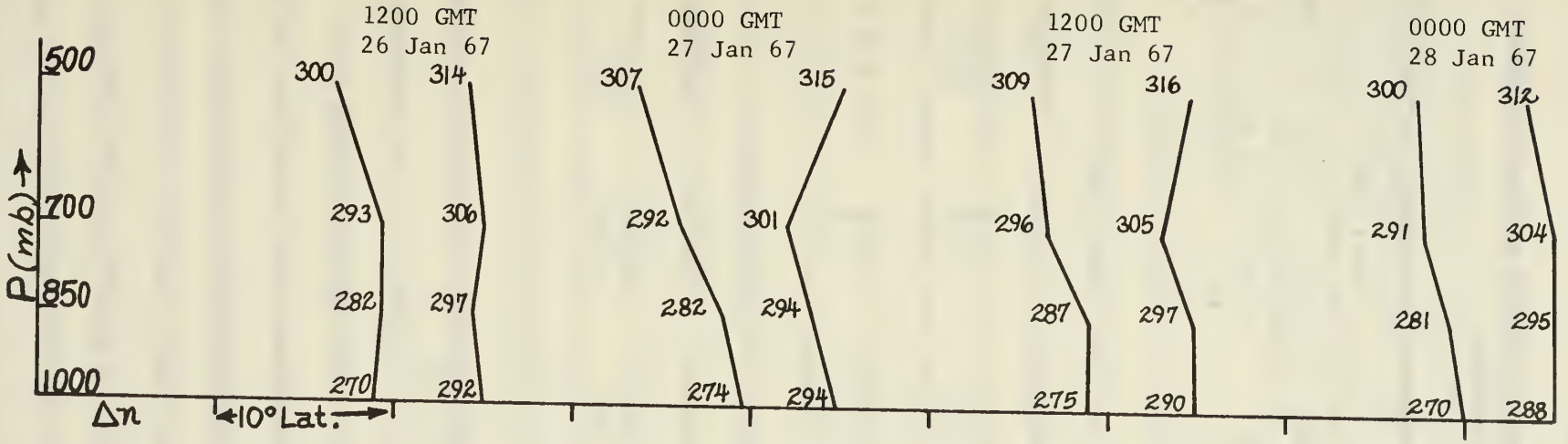


Group IV



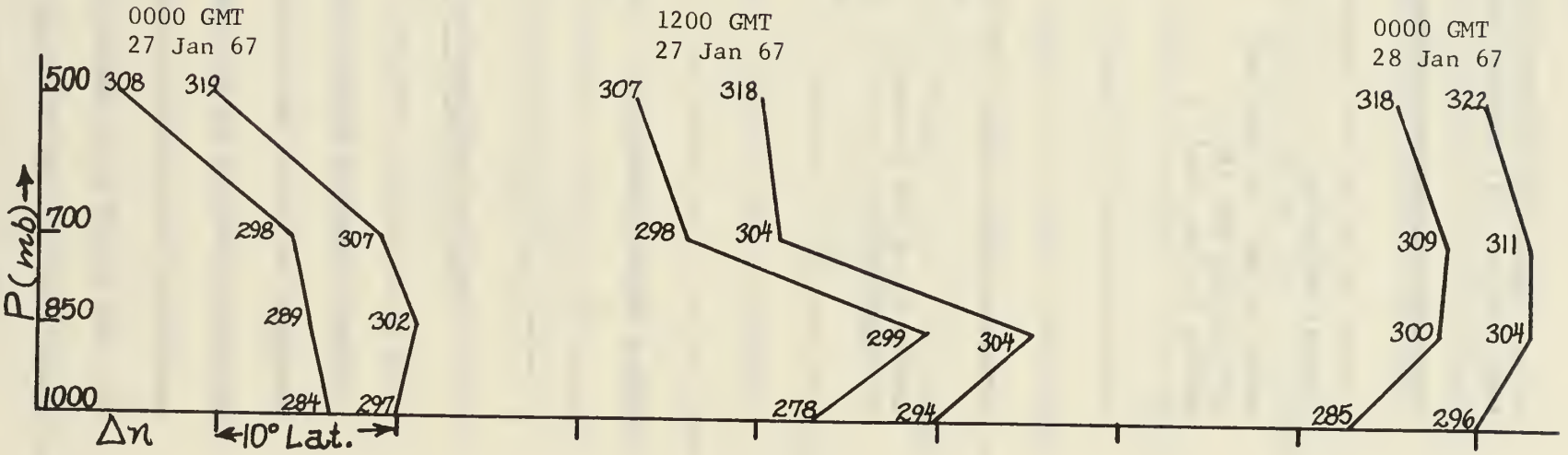


Group V

Table 10. Statistics for the numerically-analyzed HBZs in Figs. 32-34. All numbers represent averages.

| Frontal Parameter | | <-----Level (mb)-----> 1000 | 850 | 700 | 500 |
|---|---|---|---|---|---|
| width of HBZ, $\Delta n$ (deg lat) | | 6.2 | 6.6 | 6.8 | 7.6 |
| $\Delta\theta^*$ through HBZ (C) | | 22 | 16 | 13 | 12 |
| $\Delta\theta^*/\Delta n$ (C [deg lat]$^{-1}$) | | 3.5 | 2.4 | 1.9 | 1.6 |
| | | <-----Layer (mb)-----> 1000/850 | 850/700 | 700/500 | |
| $\Delta\theta^*$ along HBZ boundary (C) | K: | 11.5 | 9.6 | 11.6 | |
| | W: | 5.0 | 6.8 | 10.0 | |
| $\Delta\theta^*/\Delta Z$ along HBZ boundary (C [1000 ft]$^{-1}$) | K: | 2.3 | 1.9 | 1.5 | |
| | W: | 1.0 | 1.4 | 1.3 | |
| | | <-----Layer (mb)-----> 1000/850 | 850/700 | 1000/700 | |
| Slope of HBZ boundary | K: | 1/55 | 1/175 | 1/115 | |
| | W: | 1/15 | 1/164 | 1/90 | |

Thermal Character of HBZ Boundaries--HBZ boundaries are known to show an associated increase of potential temperature with increasing height. O'Connor (United States Navy, 1952) observed rather small changes, as 298 to 302 K along the wintertime polar front from sea level to 500 mb, respectively. However, the Canadians indicate larger changes are likely along frontal zones (Godson, 1950), as 296 to 312 K in winter and 305 to 323 K in summer along the polar front from 850 to 500 mb, respectively. The $\theta^*$ values used here steadily and consistently increase

in magnitude along the HBZ boundaries at a rate which averages close to 1.3 C (1000 ft)$^{-1}$ from 850 to 500 mb, and hence are quite compatible with the Canadian values. The less conservative nature of the cold boundaries is borne out by the higher average rate of $\Delta\theta^*/\Delta Z$ compared to that of the warm boundaries in the layer 1000 to 700 mb (i.e., 2.1 versus 1.2 C [1000 ft]$^{-1}$).

Frontal Slope--The frontal-zone slopes are greater at low levels and for the warm-side boundary of HBZs, as expected from conventional notions of fronts. However, the slopes appear more erratic than those which would be expected from manually-drawn fronts; negative slopes (i.e., HBZs sloping toward warm air with increasing height) occur in 20 percent of the cases. In the layer below the 700 mb level, such behavior is partly due to the poor numerical resolution inherent in the mass structure model for the layer 775 to 1000 mb (Chapter III) and the predominance of steeply-sloping cold fronts in the sample considered here. In the layer above the 700 mb level, the picture may be further complicated by fronts which are rooted in the high troposphere and have position and intensity not intimately associated with the low-level phenomena (Fig. 35). A similar feature was evident in the DG$\theta^*$ analyses for the summer-season case study.

Time Continuity--The cross-sections of HBZ-boundary profiles shown in Figs. 32-34 are graphed in such a way as to aid in analyzing time continuity. Table 11 presents information on two time-continuity parameters derived from changes of the warm (w)- and cold (k)-side boundaries of the HBZs in the layers 1000/850 mb and 850/700 mb.

1. The percentage of time that the algebraic sign of the 12-hour slope change is the same for the w and k boundaries of the HBZ.

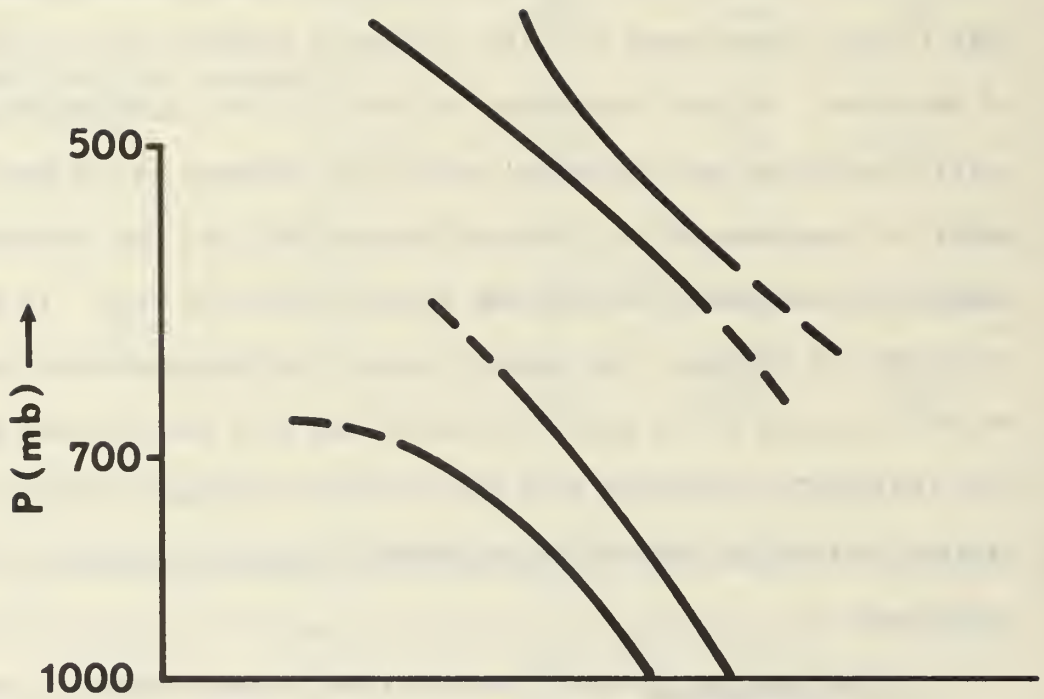


Fig. 35. Schematic profiles of HBZ boundaries for coexisting low- and high-troposphere frontal zones (Endlich & McLean, 1957).

Table 11. Time-continuity statistics for numerically-analyzed HBZs in Figs. 32-34. Column a--Algebraic signs of 12-hour slope change same for w- and k-side boundaries of HBZ. Column b--Algebraic signs of 12-hour change in HBZ width and slope of positive and negative DGθ* axes differ.

| Cross section group | Average frequency (percent) | | |
|---|---|---|---|
| | a | b | |
| | | + axis | -axis |
| I | 100 | 67 | 67 |
| II | 50 | 67 | 100 |
| III | 50 | 33 | 33 |
| IV | 90 | 64 | 53 |
| V | 100 | 70 | 33 |
| VI | 100 | 50 | 50 |

2. The percentage of time that the algebraic signs of the 12-hour change in HBZ width and slope of each of the DGθ* axes differ.

The internal consistency of the numerical product is shown by the fact that over 80 percent of the time slope changes in the positive and associated negative axes of the DGθ* field are similar in algebraic sign. There is no apparent pattern in the changes of slope and width of HBZs. In other words, as the frontal-zone boundaries steepened or became more horizontal with time the HBZ widths may either increase or decrease.

The relation of 12-hour changes in HBZ width and magnitude of DGθ* is quite conclusive in the case of increasing HBZ widths, since 73 and 87 percent of the DGθ* values along the associated positive and negative axes, respectively, decreased during the same period. However, the

situation for decreasing HBZ width is more nebulous with an average of only 46 percent of the changes in $|DG\theta^*|$ being positive for both axes. Thus, the weakening HBZs (using zone width as an indicator) correlate well with changes in the magnitude of $DG\theta^*$, but the cases of intensifying HBZs are indefinite in this respect. This situation is not unexpected as a consequence of poor resolution in the numerically-processed data (Chapter II).

The final figure of this chapter (Fig. 36) depicts a two-day time continuity (0000 GMT 26 January to 1200 GMT 27 January 1967) of 850 mb numerically-analyzed frontal positions. Only those frontal phenomena over the ample-data United States area are in focus here. The aim is one of illustration, not statistical comparison. The time continuity of the HBZ warm-side boundaries appears logical in the area east of the Rocky Mountains. However, behavior over the mountainous southwest United States is erratic. Further, the absence of occluded structure is to be noted.

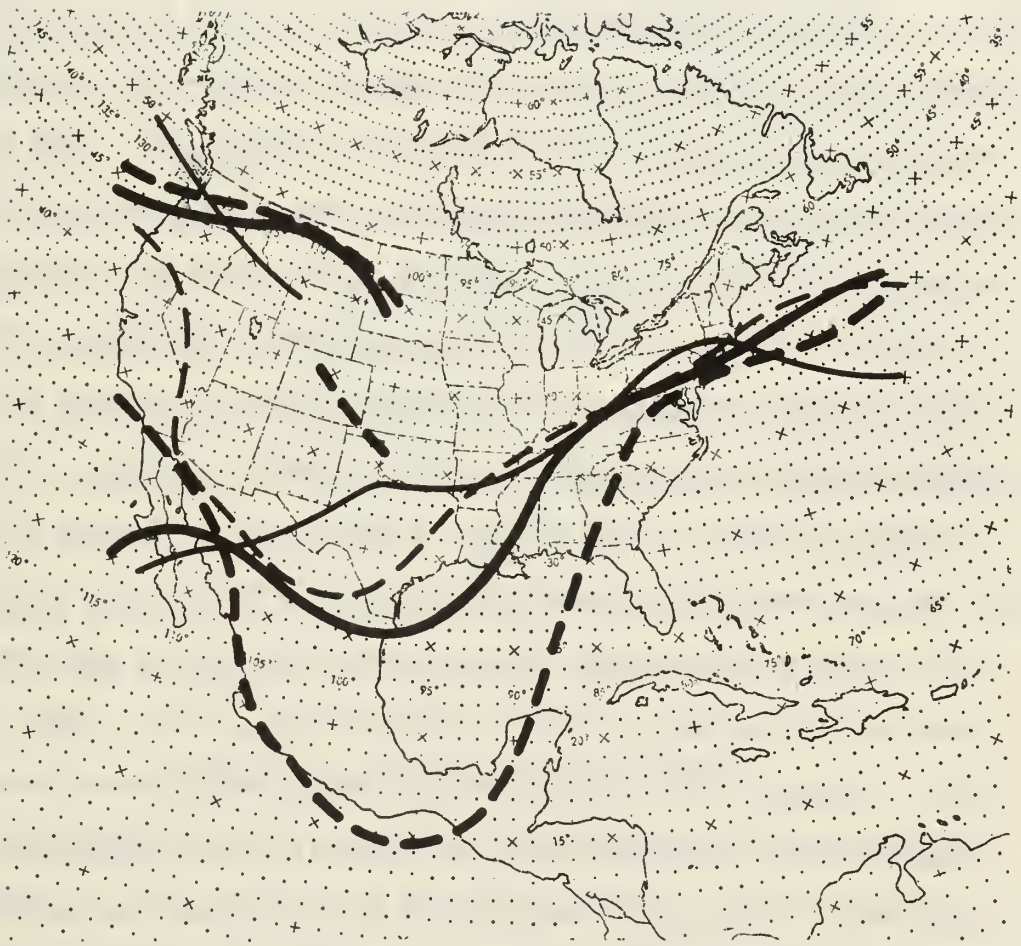

Fig. 36. Time continuity of 850 mb numerically-analyzed fronts (i.e., warm-side boundaries of HBZs): 0000 GMT 26 January 1967 (thin solid lines); 1200 GMT 26 January 1967 (thin dashed lines); 0000 GMT 27 January 1967 (heavy solid lines); 1200 GMT 27 January 1967 (heavy dashed lines).

# CHAPTER VI

## THE DGθ* MODEL:
## A CASE STUDY OF HYPERBAROCLINIC ZONES
## IN RELATION TO CLOUD AND VERTICAL MOTION

The hyperbaroclinic zones of major interest to the field meteorologist are those migratory transition regions of the middle latitudes separating cold polar from warm tropical air. Such zones are invariably associated with synoptic-scale cloud and vertical motion patterns which have a common signature in the large-scale sense but vary in small-scale details mostly due to geographic influences. The clouds are the visible manifestation of saturation due to relative moisture content and the time-integrated effect of vertical motion. The intensity and shape of the vertical motion field is largely a function of the two baroclinicity-dependent parameters which may be described as the vertical rate of change of vorticity advection and the horizontal Laplacian of thickness advection (Krishnamurti, et al., 1966; Sanders, 1963). However, a one to one correspondence between baroclinicity and cloud patterns or baroclinicity and vertical motion patterns does not exist due to the diverse combinations of the thermal and vorticity forcing functions. Nevertheless, the relation of cloud to hyperbaroclinicity has been modeled for use in synoptic analysis and forecasting, starting with the Norwegian concept of polar front-phenomena in the 1920s

(Petterssen 1956a,b) and more recently by those observant meteorologists attempting to exploit the operational uses of the weather satellite (Boucher and Newcomb, 1962; Anderson et al., 1966).

Fig. 37 qualitatively implies a cloud-HBZ relation widely held by the current-day field meteorologist. Though certainly less ideal than the early-century concepts, the model must be described as a heavily-smoothed version of the real atmosphere. The extensive cloud masses and bands made up of cirriform, stratiform, and cumuliform clouds near the cloud-mass vortex, in the warm sector, and especially adjacent to and within the frontal zone, are indicators of significant tropospheric vertical ascent. For other areas, especially the closed-cellular and cloud-free regions, the vertical motion is likely to be negative over at least part of the troposphere.

Until the existence of a model to quantitatively specify the location and intensity of frontal zones, an objective comparison between hyperbaroclinicity, vertical motion, and cloud has not been possible. The research described below concerned itself with such a substudy, with emphasis on the relation of satellite-observed cloud to the HBZ.

## Selection of Period and Area of Study

An eleven-day winter period, 7-17 December 1966, was chosen to investigate the relationships of satellite-observed clouds and FNWC's vertical motion fields[1] (Hughes, 1967) to the HBZs derived from the

---

[1] FNWC calculates vertical motion from a diagnostic $\omega$ equation in the form $\nabla^2(\sigma\omega)+(pf\eta/R)(\partial^2\omega/\partial p^2) = \nabla^2(g/f\ J[D,T])-J(T,\eta) - J(D,g/f\ [\nabla^2 T])$, where $\sigma$ is a stability parameter, J is the Jacobian, D is the isobaric-height deviation from the United States Standard Atmosphere, $\eta$ is absolute vorticity, and other symbols are standard.

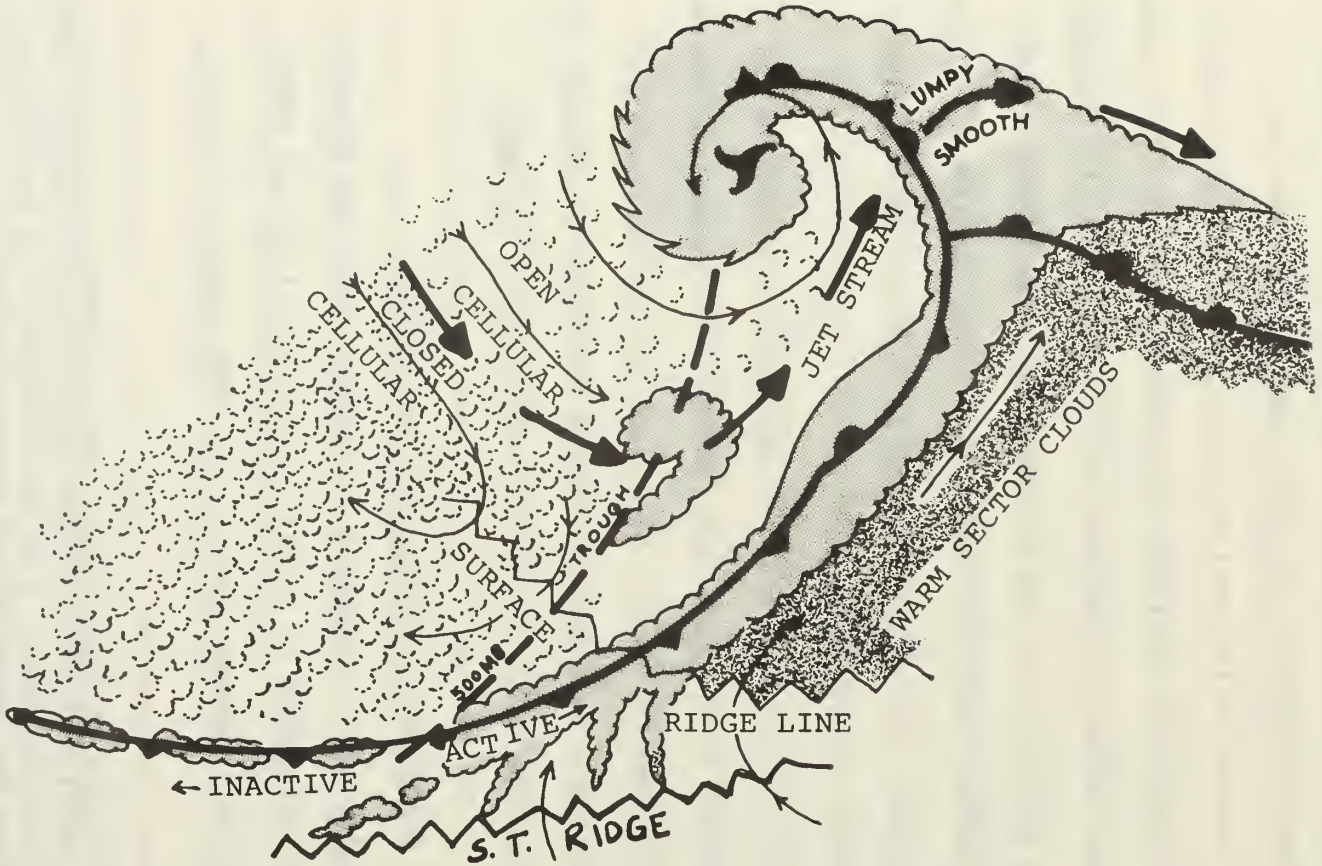


Fig. 37. Schematic illustration of idealized satellite-observed cloud masses and bands in relation to an occluded surface front. Surface flow, ; warm-air boundary of the HBZ, ; 500 mb jet axis, ; and 500 mb trough, (after Anderson, et. al., 1966).

$DG\bar{\theta}^*$ model using the $\bar{\theta}^*$ appropriate to the layer 1000/700 mb. The weather satellite information used in the study consisted of NMC-analyzed nephanalyses of the AVCS-type ESSA III observations. In order to consider a significantly large area while at the same time maintaining reasonable concurrency of cloud and HBZ analyses, only the nephanalyses within four hours of the 0000 GMT and 1200 GMT times were utilized.

Use of the satellite-observation periods of 2000 to 0400 GMT and 0800 to 1600 GMT determined two major geographical areas of study. The time interval centered at 0000 GMT gave coverage over most of the North Pacific Ocean plus a portion of North America west of 95W, while the second interval gave coverage of the eastern North Atlantic Ocean east of 55W, Europe, and western Asia to 90E. Since the seasonally-imposed northern limit to the daylight satellite view is close to 60N and since the numerical frontal analysis is not too reliable at latitudes less than 15N due to sparse data, the south and north boundaries of the areas of study were chosen accordingly.

The December 1966 weather situation was characterized by abnormally strong zonal flow over much of the Northern Hemisphere with mean troughs near both coasts of North America (Dickson, 1967). In the North Pacific area a series of frontal-wave cyclones moved through the latitude band 40-55N, recurving northeast into the Gulf of Alaska. In the North Atlantic region, the major storm track was confined to polar latitudes north of 60N due to the presence of a relatively strong, stationary subtropical high in the middle latitudes. Because of the blocking situation, only the trailing portions of fronts crossed

into the North Atlantic area of study. Over the Eurasian continent, the weather in the early part of the period was dominated by a high pressure cell over Siberia and weak frontal lows in the Mediterranean. In the last half of the period the weather was generated mainly by low cells in the North Sea and over the northern part of the continent with frontal activity across Europe extending southward to the Mediterranean.

In the illustrations and cloud statistics which follow only cloud amounts are considered. That is, no attempt was made, on the basis of the nephanalyses, to make any distinction between high, middle, and low cloud types. An exception to this procedure occurred for the cases of cloud bands or masses composed entirely of cirriform cloud. Such clouds were considered to have no direct relation to the low-troposphere HBZs and were not included in the statistics. With reference to standard satellite meteorology terminology, the cloud amount covered, C, indicates > 80 percent cloud cover while mostly covered, MCO, specifies 50-80 percent sky coverage.

## Patterns of Vertical Motion and Cloud in Relation to the Numerically-Analyzed Fronts

Some notion of the empirical relations between the numerically-analyzed 1000 mb front, satellite-observed clouds, and 850 mb vertical motion may be obtained by viewing a 3-day sequence (15-17 December 1966) for the North Pacific area (Figs. 38-40). The area is not necessarily the most desirable for such a demonstration due to sparsity of data, but the wide expanse of uniform surface aids in generating patterns of a more universal nature.

Cloud banding appears to be well-related to the 1000 mb fronts in orientation. However, as expected, the colocation is not as ideal as that of the model in Fig. 37. The low-latitude fronts are associated with long-trailing cloud bands extending from middle latitudes into the subtropics. Many of the HBZ boundaries are within the area covered by cloud masses which include bands not evident to the cloud analyst. It is to be noted that not every $D\bar{G\theta}^*$ axis is simply related to a cloud mass or band nor does every such cloud entity correspond to a synoptic-scale HBZ. The vast majority of $D\bar{G\theta}^*$ maxima $\geq 15 \times 10^{-2}$ $(100 \text{ km})^{-2}$ are found in the covered and mostly covered areas.

The relation of vertical motion to HBZs is more difficult to analyze. As discussed earlier, a given pattern of vertical motion is related more clearly to cloud than to the zones of hyperbaroclinicity. However, major areas of 850 mb vertical motion[2] (i.e. centers $\geq 1.0$ cm $\text{sec}^{-1}$) are somewhat related to HBZs, with 60 percent of the centers of ascent located within such zones and most of the remainder in the adjacent warm-air subbaroclinic zone, similar to models suggested by Sanders (1963) and Todson (1964). The orientations of low-latitude vertical motion patterns do not appear to be closely associated with either the cloud bands or $D\bar{G\theta}^*$ axes. A part of the problem of interpretation here is due to lack of radiosonde data in the area.

In summary, the illustrations shown here do not suggest an unqualified set of usable relations between HBZs, vertical motions,

---

[2]This area was contained within the 1 cm $\text{sec}^{-1}$ isoline for 500 mb vertical motion more than 95 percent of the time. Patterns at the two levels were very similar; only the magnitude differed.

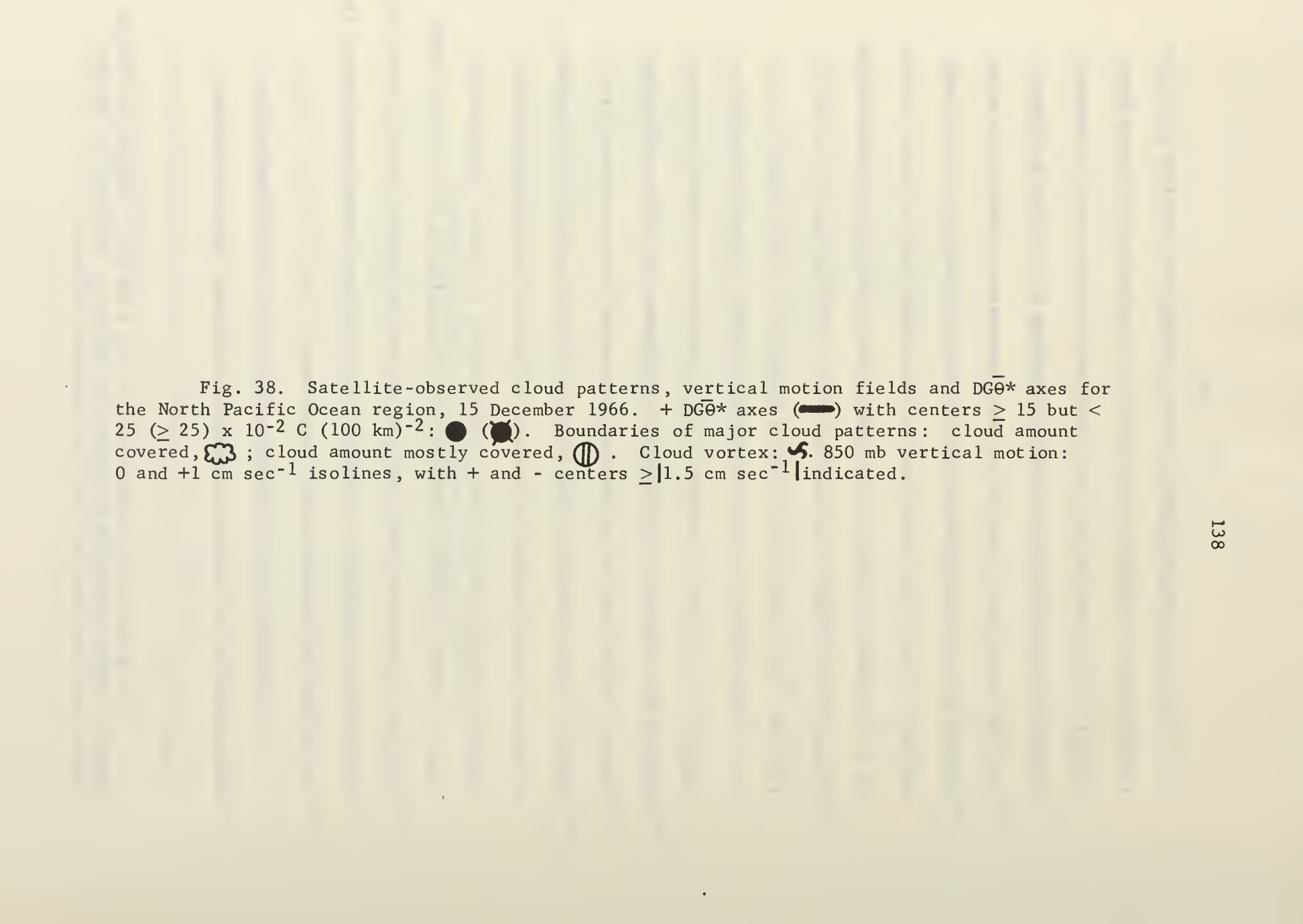

Fig. 38. Satellite-observed cloud patterns, vertical motion fields and $DG\bar{\theta}^*$ axes for the North Pacific Ocean region, 15 December 1966. + $DG\bar{\theta}^*$ axes (▬) with centers $\geq$ 15 but < 25 ($\geq$ 25) x $10^{-2}$ C (100 km)$^{-2}$: ● (✱). Boundaries of major cloud patterns: cloud amount covered, ☁ ; cloud amount mostly covered, ▥ . Cloud vortex: ⟆. 850 mb vertical motion: 0 and +1 cm sec$^{-1}$ isolines, with + and - centers $\geq$ |1.5 cm sec$^{-1}$| indicated.

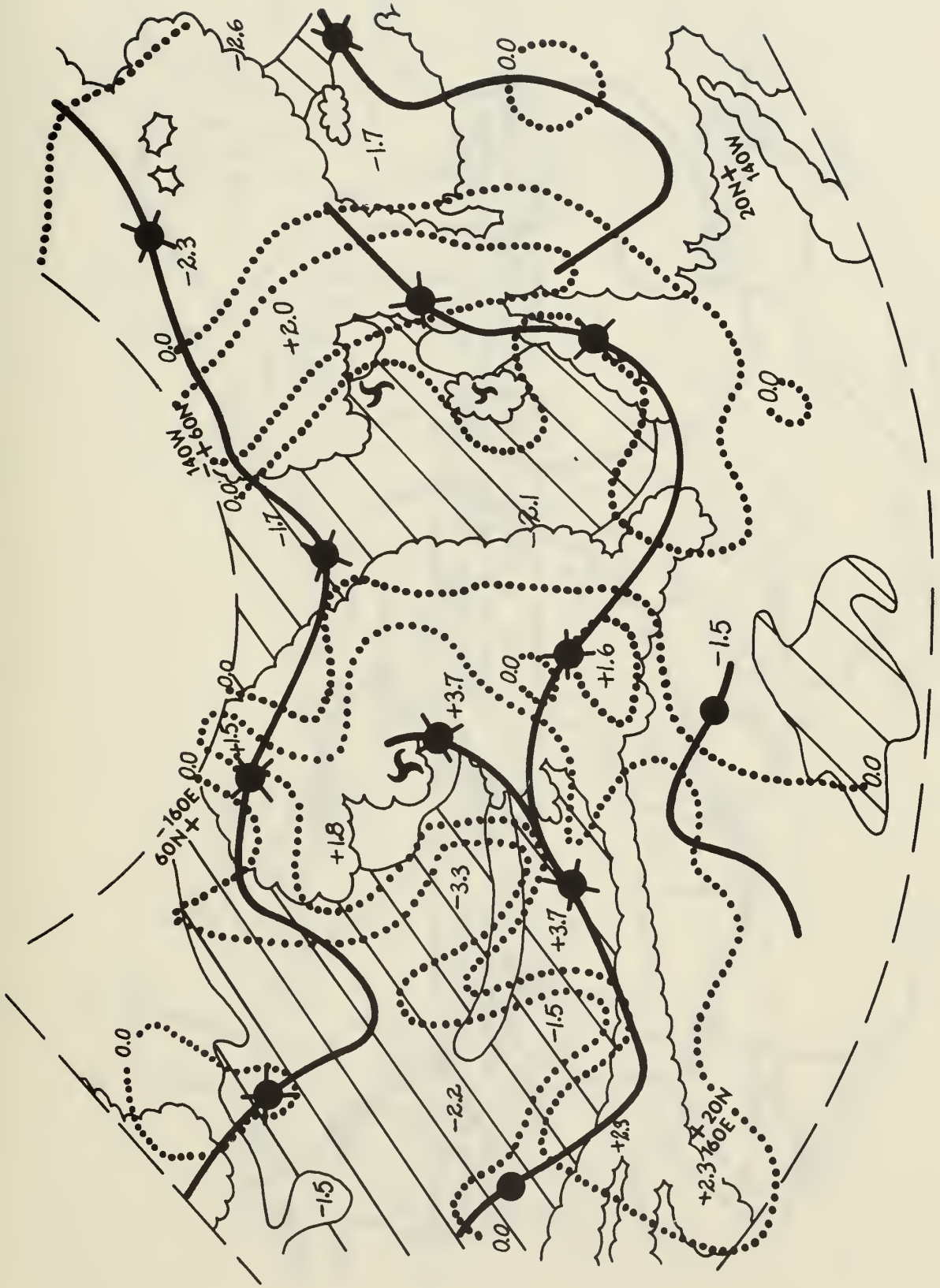
-2.6
-2.3
-1.1
0.0
20N+ 140W
+2.0
0.0
140W 60N+
-1.7
0.0
-2.1
0.0
+1.5
0.0
60N+ 160E
+1.8
+3.7
0.0
+1.6
-1.5
-3.3
+3.7
-1.5
-2.2
+2.3
0.0
-1.5
0.0
+2.3 160E 20N+

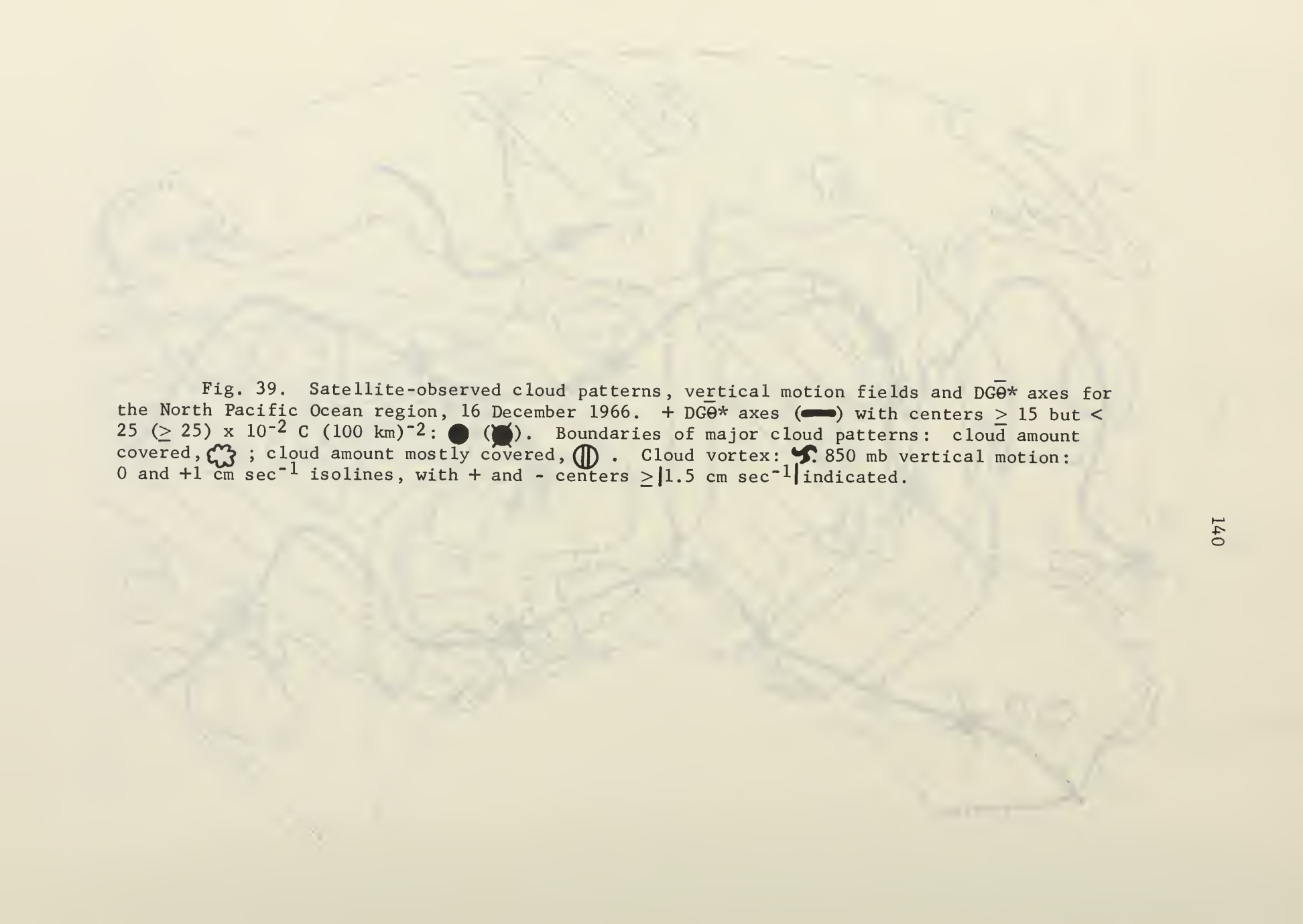

Fig. 39. Satellite-observed cloud patterns, vertical motion fields and $DG\bar{\theta}^*$ axes for the North Pacific Ocean region, 16 December 1966. + $DG\bar{\theta}^*$ axes (▬) with centers $\geq 15$ but $< 25$ ($\geq 25$) x $10^{-2}$ C $(100\ km)^{-2}$: ● (✱). Boundaries of major cloud patterns: cloud amount covered, ; cloud amount mostly covered, . Cloud vortex: . 850 mb vertical motion: 0 and +1 cm $sec^{-1}$ isolines, with + and - centers $\geq |1.5|$ cm $sec^{-1}$ indicated.


0.0
-3.8
-2.8
+2.8
140W 20N
+1.8
140W 60N
+2.3
+2.1
+2.1
0.0
+1.7
-1.7
+1.9
-3.4
+2.1
160E 60N
160E 20N
+2.3

Fig. 40. Satellite-observed cloud patterns, vertical motion fields and $DG\bar{\theta}^*$ axes for the North Pacific Ocean region, 17 December 1966. + $DG\bar{\theta}^*$ axes (▬) with centers $\geq$ 15 but < 25 ($\geq$ 25) x $10^{-2}$ C $(100\ km)^{-2}$: ○ (●). Boundaries of major cloud patterns: cloud amount covered, ; cloud amount mostly covered, . Cloud vortex: . 850 mb vertical motion: 0 and +1 cm $sec^{-1}$ isolines, with + and - centers $\geq$ |1.5 cm $sec^{-1}$| indicated.

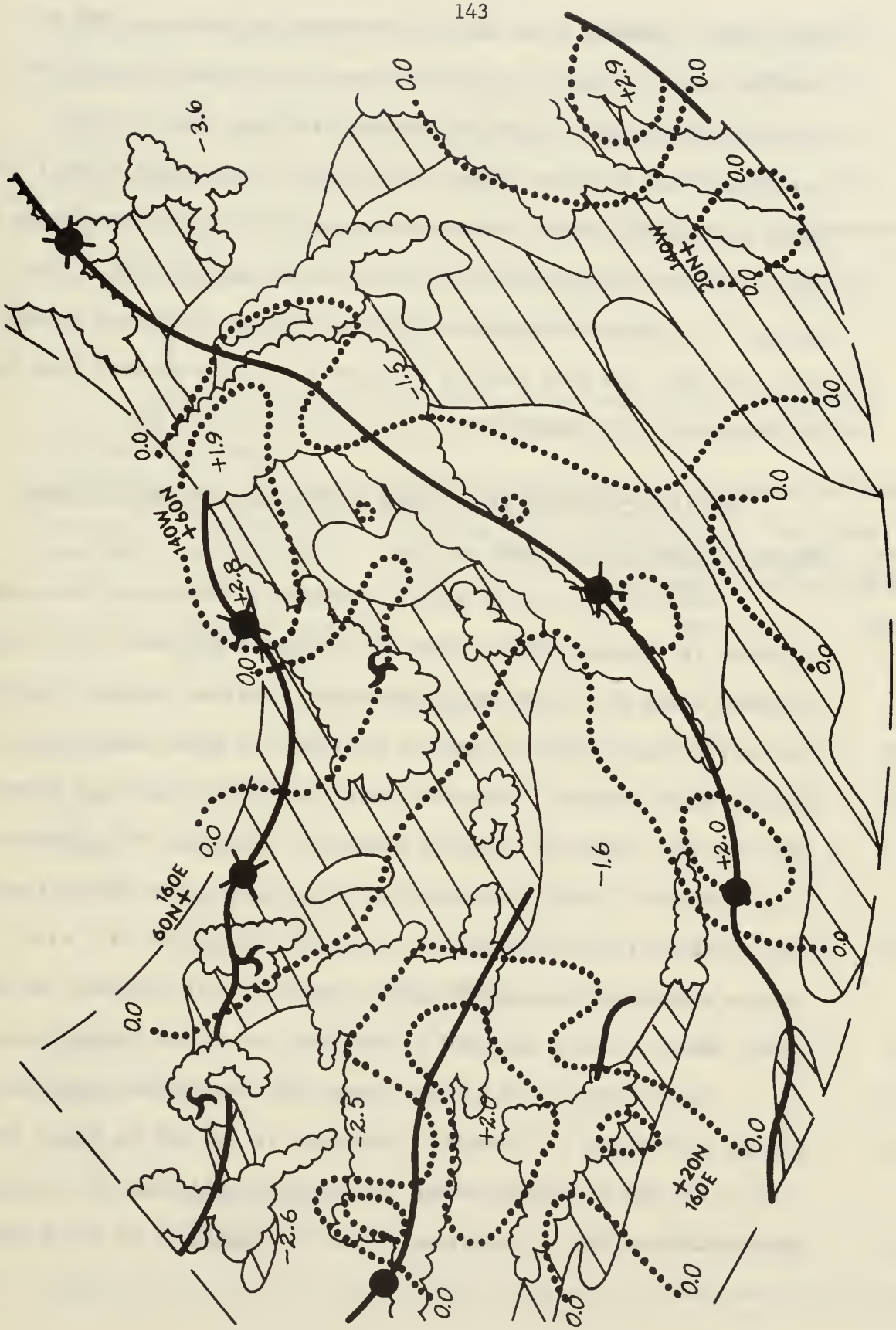
-3.6
0.0
+2.9
0.0
0.0
20N+
140W
0.0
0.0
-1.5
0.0
+1.1
0.0
+2.8
40N+
140W
0.0
0.0
60N+
160E
0.0
-1.9
+2.0
0.0
0.0
-2.2
-2.2
+2.2
0.0
+20N
160E
0.0
0.0
0.0

and clouds. However, it is obvious that HBZs and areas of 850 mb vertical motion equal to and greater than +1.0 cm $sec^{-1}$ are associated with major cloud bands and masses. Further, there is the suggestion that the less significant (i.e., very narrow) frontal cloud bands are found adjacent to and oriented similarly to the positive $DG\bar{\theta}^*$ axes; in these regions the vertical motion is generally less than + 1 cm $sec^{-1}$. In order to quantitatively specify the relations between cloud and HBZ, the next section presents statistics derived from the 7-17 December 1966 period.

Satellite-Observed Cloud Bands Versus Hyperbaroclinic Zones

Stratification by Latitude

Statistics on cloud bands, stratified by latitude, are shown in Table 12. Average $DG\bar{\theta}^*$ values are indicated for each of the three latitude bands in the two major hemispheric regions sampled, namely, the North Atlantic east to western Asia and the North Pacific east to western North America. The relatively high $DG\bar{\theta}^*$ intensities along the positive axes indicate that the warm-side boundaries of hyperbaroclinic zones represent closer approximations to a first-order discontinuity than the cold-side boundaries, as concluded in Chapter II. Also, the average magnitude of the $DG\bar{\theta}^*$ values increases with latitude, an indirect measure of the poleward intensification of the frontal zones.

The statistics on clouds versus HBZs demonstrate that the average percentage of C and MCO cloudiness in the HBZ is larger than that in the SBZ at corresponding latitudes, considering all latitudes between 15N and 60N. Conditions in the low latitudes of the Pacific

area and the high latitudes of the Atlantic area are most responsible for the near two to one ratio of cloud percentages in the HBZ versus the SBZ. Although the combined percentage of C and MCO cloud cover inside (especially) and outside the HBZ markedly increases with latitude, the actual area covered by clouds in each latitude band increases more slowly since the area ratios of the two latitude bands, 30-35N and 45-60N, to 15-30N are .86 and .65, respectively.

Table 12--Relation of satellite-observed clouds to hyperbaroclinic and subbaroclinic zones, stratified by latitude, for period 7-17 December 1966.

| Latitude band (deg) | Average $D\bar{G\theta}^*$ ($C[100\ km]^{-2}$) | | Percentage of latitude band within HBZ | Percentage of HBZ with cloud amount | | Percentage of SBZ with cloud amount | |
|---|---|---|---|---|---|---|---|
| | Negative Axes | Positive Axes | | C | MCO | C | MCO |
| | | | Atlantic-Eurasian-African Region | | | | |
| 15-30N | .11 | -.08 | 39 | 13 | 12 | 8 | 12 |
| 30-45N | .19 | -.09 | 30 | 41 | 18 | 19 | 15 |
| 45-60N | .20 | -.19 | 37 | 65 | 9 | 30 | 7 |
| | Area-weighted average for 15-60N | | 37 | 31 | 13 | 16 | 12 |
| | | | Pacific-North American Region | | | | |
| 15-30N | .11 | -.05 | 24 | 30 | 16 | 11 | 8 |
| 30-45N | .17 | -.13 | 37 | 51 | 26 | 25 | 16 |
| 45-60N | .20 | -.15 | 33 | 63 | 15 | 38 | 14 |
| | Area-weighted average for 15-60N | | 30 | 41 | 20 | 19 | 11 |

Stratification by
Geographical Area

Table 13 considers each type of cloud band (frontal covered, non-frontal covered, and non-frontal mostly covered) in each of the following six geographical zones: A, North Pacific; B, western North America; C, eastern North Atlantic; D, Europe; E, western Asia (C, D, E poleward of 30N); and F, Atlantic-Africa-Asia, 15-30N. Here, the word "frontal" refers to the satellite cloud entity labeled as such by the ESSA nephanalyst, apparently when the band is categorized as C and is thought to be associated with a conventional front as depicted on the NMC surface chart.

Pacific area A indicates that the average angle between the C bands and their associated $DG\overline{\theta}*$ axes is larger (29 deg versus 15 deg) and has a wider range (10-90 deg versus 5-45 deg) in the frontal than in the non-frontal cases. As discussed in Chapter III, the operational numerical frontal analysis model does not adequately depict occlusions while the amplitude and orientation of frontal cloud bands relates well to such fronts; this is a possible explanation for the observed relation. Corresponding values in area C appear to disagree with this, since the average angle in the frontal-covered category is small. However, as noted earlier in this chapter, the storm tracks and their attendant occlusions were well within the area studied in the Pacific but not in the Atlantic. Therefore the Atlantic and Pacific statistics do not conflict.

Further examination of Table 13 discloses that in the frontal-covered category a greater portion of the cloud band fell into the HBZ than in the SBZ in both ocean areas A and C, but the cloud amount in the

Table 13--Relation of satellite-observed cloud bands to hyperbaroclinic and subbaroclinic zones in the latitude band 15-60N, stratified by geographical area: North Pacific--A; North America, west of 95W--B; North Atlantic, poleward of 30N, east of 55W--C; Europe, poleward of 30N--D; Asia, west of 90E--E; and the Atlantic-Africa-Asia area, 15-30N between 55W and 90E--F.

| Area | Type cloud band and coverage | Number of bands sampled | Average angle between + $DG\bar{\theta}^*$ axis and cloud band (deg) | Range of angles (deg) | Average $DG\bar{\theta}^*$ ($C[100\ km]^{-2}$) along positive axis | Percentage of cloud bands in HBZ |
|---|---|---|---|---|---|---|
| A | Frontal C | 18 | 29 | 10 to 90 | .17 | 55 |
| | Non-frontal C | 9 | 15 | 5 to 45 | .13 | 35 |
| | Non-frontal MCO | 8 | 8 | 0 to 10 | .09 | 33 |
| B | Frontal C | 1 | 90 | | .20 | 40 |
| | Non-frontal C | 0 | | | | |
| | Non-frontal MCO | 0 | | | | |
| C | Frontal C | 8 | 14 | 5 to 35 | .25 | 61 |
| | Non-frontal C | 10 | 29 | 0 to 90 | .16 | 51 |
| | Non-frontal MCO | 1 | 10 | | .07 | 50 |
| D | Frontal C | 2 | 12 | 10 to 15 | .12 | 78 |
| | Non-frontal C | 7 | 13 | 0 to 30 | .16 | 63 |
| | Non-frontal MCO | 0 | | | | |
| E | Frontal C | 0 | | | | |
| | Non-frontal C | 10 | 28 | 0 to 90 | .23 | 55 |
| | Non-frontal MCO | 2 | 12 | 10 to 15 | .15 | 20 |
| F | Frontal C | 0 | | | | |
| | Non-frontal C | 0 | | | | |
| | Non-frontal MCO | 12 | Indefinite | | .11 | 50 |

SBZ is by no means insignificant. This result agrees with the interpretation of the model in Fig. 37, the broadening effect on the numerically-analyzed fronts, and the extensive zone width due to using $\bar{\theta}^*$ rather than $\theta^*$.

In the non-frontal C and MCO classes combined the statistics are inconclusive. In areas A and E most of the cloud banding occurs in the subbaroclinic region while in D this is true of the hyperbaroclinic zone; in C and F the bands are evenly split between the HBZs and SBZs. Non-frontal cloud bands, especially MCO, are frequently associated with the stratus and stratocumulus attending the stable regions of anticyclones and, as such, large amounts in the SBZs are to be expected.

The satellite cloud bands associated with major positive $D\bar{G}\bar{\theta}^*$ axes were also studied. An axis was classified as major if at least one $D\bar{G}\bar{\theta}^*$ value $\geq 15 \times 10^{-2}$ C $(100 \text{ km})^{-2}$ occurred along it. The results were similar to those presented in Table 13 and are not shown here.

## CHAPTER VII

## THE DG$\theta$* MODEL: HEMISPHERIC FREQUENCY AND AVERAGE INTENSITY OF HYPERBAROCLINIC ZONES

The DG$\theta$* analyses yield quite readily to an objective calculation of the frequency and average intensity of HBZs. Two 30-day periods were selected to demonstrate a synthesis of objective 1000 mb frontal analyses for the Northern Hemisphere; one, 15 January through 14 February 1966, exhibits winter-time conditions, and the other, the month of July, 1967, shows mean summer-time conditions. For both winter and summer periods the frequencies of subjectively-analyzed NMC surface fronts were also calculated. This was done over a reduced area comprising the western Northern Hemisphere, as appropriate to NMC's facsimilie transmissions of the 0000 GMT and 1200 GMT surface and 1000/500 mb thickness fields.

The frequency and intensity statistics were accumulated manually from the 0000 GMT and 1200 GMT numerical $DG\bar{\theta}$* analyses (1000/700 mb model) by tabulating the occurrence of and average intensity along those positive axes where $DG\bar{\theta}^* \geq .05$ C $(100 \text{ km})^{-2}$ for each of 3844 grid squares. Each square measures 381 km on a side, true at 60N. The NMC frontal positions, not allowing an intensity calculation, were tabulated in a similar way for frequency only.

Winter-season Sample: 15 January through 14 February 1966

Fig. 41 highlights the important features of frequency and intensity of numerically-analyzed 1000 mb fronts for the period selected. For frequency, the maximum possible occurrence per grid square is 62 which is equivalent to the number of 0000 GMT and 1200 GMT synoptic times involved in the statistic. Minimal frequency is zero, indicating no occurrence of numerical fronts in the grid zone during the period. Average intensity values have a lower limit of .05 C $(100\ km)^{-2}$ since only those positive $DG\overline{\theta}^*$ axes with values equal to or greater than five units were counted. The upper limit of intensity is only a practical one since most map-time intensities are less than 60 units of $DG\overline{\theta}^*$. In general, analysis at latitudes less than 20 deg lat is omitted due to the unreliable nature of data for these sparse-data areas.

As background to the interpretation which follows, it is to be noted that the last half of January, 1966, was anomalously cold over North America while the first half of February, 1966 (that is, at least from February 5 forward), represented a trend back to normal winter-time conditions (Ludlum, 1966). This suggests that over the ample-data North American region frontal activity should show supernormal occurrence at relatively low latitudes with subnormal, but not zero, frequency at polar latitudes. In fact, this same trend was evident over all of the western North Hemisphere (Posey, 1966; Green, 1966). The eastern section of the hemisphere, especially Europe and western Asia, was associated with relatively more disorganization and meridional flow as compared to the western section, particularly in January. The numerically-derived frontal averages for these months show essentially the same features.

Numerical Frequency

Axes of maximum frequency are multiple with mostly zonal orientation, except along the continent-ocean interface where overtones of coastal orientation are evident. Frequencies equal to or in excess of 30 percent are concentrated over land areas. Regional maxima appear on the Canadian west coast near 55N, over the extreme North Pacific in the Kamchatka Peninsula area, east of Japan at 35N, over the western and southern Mexican coastal area, and along the Asiatic front in the foothills of the Himalayas.

There are several areas of zero or near-zero frequency, as noted from the 3-percent lines in Fig. 41. The more extensive areas of minimal frequency, as in various parts of the Arctic latitudes, may be regarded as the traditional air-mass source regions. However, certain localized areas of this type are more difficult to explain, especially in view of the high frequencies in the surrounding grid zones. Examples may be found over the east coast of the United States near 35N, southwest United States, southern Finland, and ocean areas in the latitudinal band 45-50N. Most of the local minima over land have the common feature of being in a mountain-lee area while such ocean areas more likely represent tenuous boundaries between arctic air excursions toward the south and maritime-polar air traverses toward the north. Minimal zones south of the most equatorward positive $DG\overline{\theta}^*$ axes are not indicated. These zones are generally equatorward of 20N and display erratic patterns due to sparse data.

Numerical Intensity

The intensity field shows that the intense maritime fronts occur farther poleward than their counterparts over the continental regions.

Fig. 41. Frequency and intensity of numerically-analyzed 1000 mb fronts in the period 15 January through 14 February 1966. Frequency isolines for 3% (2 cases), 20% (12 cases), 30% (19 cases), and 45% (28 cases). Frequency axes: 20-29%, heavy dashed lines; $\geq$ 30%, heavy solid lines. Areas with frequencies < 3%, shaded. Axes of average $D\overline{G\theta}^*$ intensity (units, $10^{-2}$ C [100 km]$^{-2}$): 15-20 units, light dashed lines; > 20 units, light solid lines with crosses. Intensity areas $\geq$ 30 units enclosed by dashed line. Intensity axes omitted through areas of frequency < 3%.

In general, highest intensities are found over land with absolute maxima of .49 and .47 C (100 km)$^{-2}$ on the Alaskan west coast near 60N and 55N, respectively. Such figures are of significance considering that a total of 11 and 23 cases, respectively, are associated with these intensities.

The large-scale relation between intensity and frequency is one of maximum intensity lagging the most frequent position of the front. That is, the former is toward the coldest air from the axis of greatest frequency.

NMC Frequency

It is of interest to compare the frequencies of NMC's manually-analyzed fronts (Fig. 42) to the objective version in Fig. 41. The format in both figures is the same for easy comparison. However, an intensity comparison is not possible in the case of the NMC fronts.

The major differences between NMC and numerical in this short-period mean are similar to those found in the single-time views. For instance, the many occlusions in the eastern ocean areas give more meridional orientation to the NMC compared to the numerical frequency axes since the latter does not portray such fronts very well (Chapter III). Another extensive area of difference is eastern Canada and the North Atlantic Ocean, particularly Greenland and Hudson Bay, which shows high frequency in the $D\bar{G}\bar{\theta}^*$ field, but near zero occurrence on the NMC chart. Such a difference is to be expected since it is not common practice to depict orographic and other semi-permanent frontal zones on NMC's daily operational weather charts. The NMC and numerical patterns are most compatible over the Canadian Archipelago, mountainous sections of western

Canada, and the United States and the North Atlantic equatorward of 40N.

Summer-season Sample: July, 1967

Data for the summer-season month, July 1967 (Fig. 43), are presented in the same fashion as the winter period discussed above. Initially, the data were stratified by the upper-air observation times 0000 GMT and 1200 GMT in order to analyze diurnal variations, but one month's data proved to be inadequate for this purpose.

To aid in interpreting the July 1967 frontal statistics, the following comments regarding the Northern Hemisphere weather are of interest. The subject month was much like January 1966 in that North American temperatures were well below average east of the Rockies. Record lows were common and associated with polar-front penetrations well equatorward of normal, especially over southeast United States (Ludlum, 1967). In the European and central and west Atlantic and Pacific areas, low-troposphere high pressure systems were well developed with anticyclonic and supernormal zonal flow at higher latitudes than usual for July. Thus, frontal positions may be expected poleward of normal at these longitudes. In the Asiatic sectors the flow patterns were not suggestive of any marked or unusual frontal phenomena (Dickson, 1967b).

Numerical Frequency

Compared to winter, there are fewer and less extensive frequency axes with values $\geq$ 20 percent but relatively more points with frequency $\geq$ 30 percent along the axes. Isolines of 45 percent and 60 percent are

Fig. 42. Frequency of manually-analyzed NMC surface fronts in the period 15 January through 14 February 1966 for the western section of the Northern Hemisphere. Frequency isolines for 3% (2 cases), 20% (12 cases), 30% (19 cases), 45% (28 cases), and 60% (37 cases). Frequency axes: 20-29%, heavy dashed lines; $\geq$ 30%, heavy solid lines. Areas with frequencies $<$ 3%, shaded.

Fig. 43. Frequency and intensity of numerically-analyzed 1000 mb fronts, July 1967. Frequency isolines for 3% (2 cases), 20% (12 cases), 30% (19 cases), 45% (28 cases), and 60% (37 cases). Frequency axes: 20-29%, heavy dashed lines; $\geq$ 30%, heavy solid lines. Areas with frequencies < 3% shaded. Axes of average $D\bar{G}\bar{\theta}^*$ intensity (units, $10^{-2}$ C [100 km]$^{-2}$): 12.5-15 units, light dashed lines; > 15 units, light solid lines with crosses. Intensity areas $\geq$ 20 units enclosed by dashed line. Intensity axes omitted through areas of frequency < 3%.

to be found over Asia, Africa, Mediterranean Europe, and mountainous North America. An absolute maximum frequency of 70 percent is reached along the southern periphery of the Iranian mountains (near 30N), just inland from the Persian Gulf and the hot Saudi-Arabian desert to the southwest.

Areas with near-zero frequencies are of greater extent in summer than in winter, both in the Arctic and as buffer zones between the zonally-oriented major frontal axes. The multiplicity of such minimal areas points out the reduced latitudinal migration of fronts in the former as compared to the latter season.

Except for northern sections, frontal frequencies of any consequence over oceans are non-existent. However, the relation of latitudinal positions of continental and maritime fronts is similar to winter. The circulation patterns prevailing in July 1967 undoubtedly emphasize this relation. The zonal extent of fronts is interrupted by the coastal orientation and orographic influence over the western continental areas of Europe and North America. The extensive Asiatic front has shifted to the polar-side desert basins of the Himalayas at most longitudes, a seasonal shift expected from the nature of the thermal patterns in the two seasons.

The frontal ring over mountainous western North America may be explained by a number of features on the periphery of a July maximum-temperature area normally centered near 37N, 113W (U. S. Navy, 1966). One such feature was discussed in Chapter V (Fig. 26), namely the differential heating across the land-sea interface. Other sections of the ring-like front are due to the polar front, usually found near the

Canadian-United States boundary in the summer season, the sparse-data and cooler mountain and ocean sectors along the south-southwest fringe of the desert area, and a combination of moisture and temperature differences between land and water areas to the east and southeast of the hot elevated basin. The last-enumerated phenomenon generates the dew-point front, occurring often through the Texas area in summer (U.S. Navy, 1952). A less prominent but similar situation occurs over northwest Africa.

Numerical Intensity

As expected, the intensity field is more complex and much reduced in magnitude compared to winter. The maximum average intensity of .21 C $(100\ km)^{-2}$, found just off the Atlantic coast of African Morocco, is less than half of the absolute maximum noted in the winter sample. However, intensities over mountainous western North America closely approach 20 units. Most zonally-oriented fronts at latitudes less than 40N and most ocean fronts are not associated with intensity axes of significance, using $\geq$ 15 units as the criterion. The lag of the maximum intensity zones relative to maximum frequency zones, evident in winter over the east continent-west ocean areas, is not apparent in the summer picture; rather, the orientation of frequency and intensity axes tends toward coincidence in the mean.

NMC Frequency

The pattern of axes on the NMC analyses are not entirely according to expectation (Fig. 44). The multiplicity of major axes of frontal frequency not only exceed NMC's winter picture but numerical in summer as well. The relation to numerical is least expected as a result of variations noted in the daily patterns (Chapter III). An area in point is

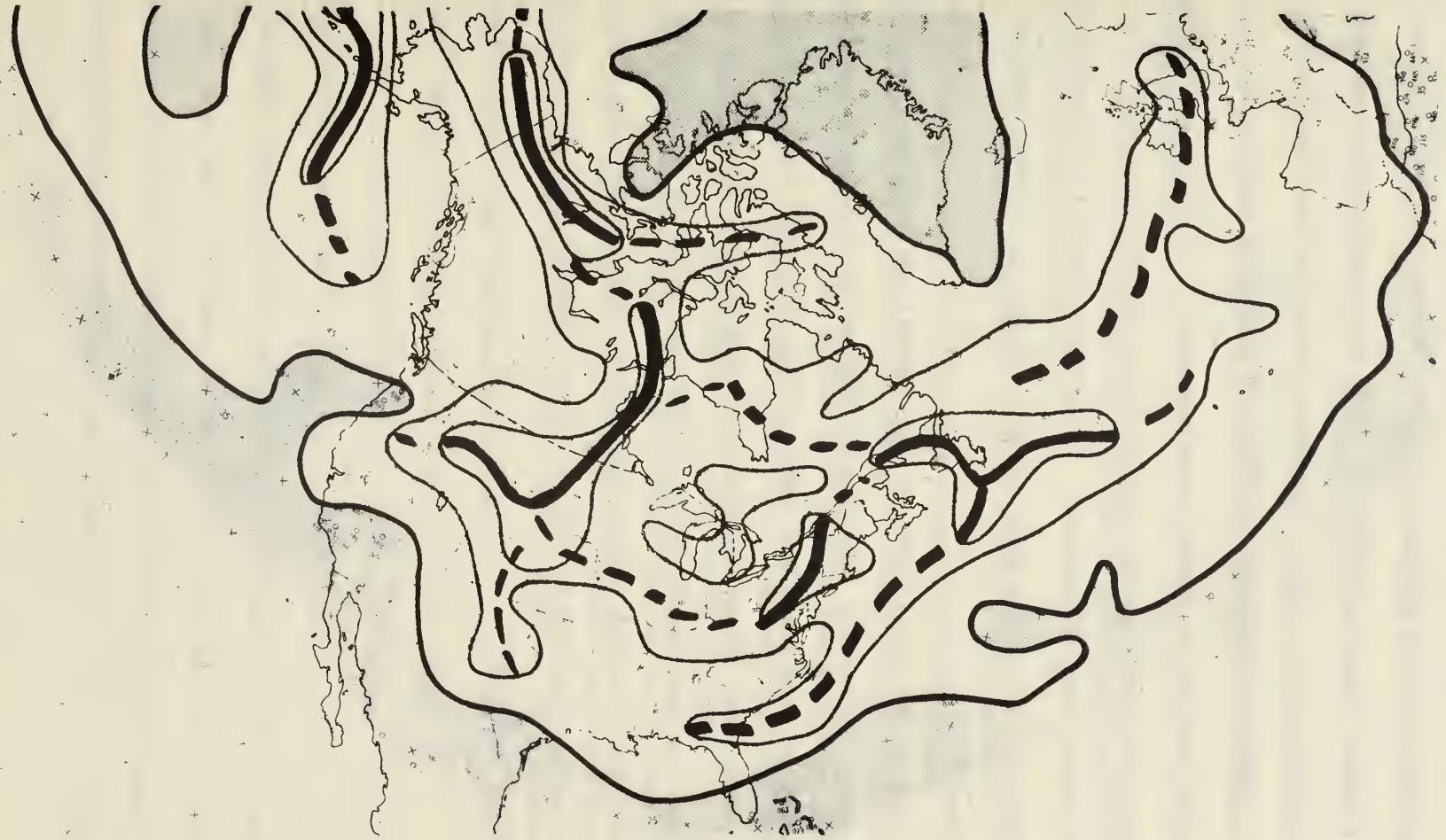

Fig. 44. Frequency of manually-analyzed NMC surface fronts, July 1967, for the western section of the Northern Hemisphere. Frequency isolines for 3% (2 cases), 20% (12 cases), 30% (19 cases), and 45% (28 cases). Frequency axes: 20-29%, heavy dashed lines; $\geq$ 30%, heavy solid lines. Areas with frequencies < 3%, shaded.

eastern North America and extreme western Atlantic, usually one of maximum agreement in the NMC and numerical frontal analyses. Since the manual product does not suffer greatly from sparse-data boundary effects and since the seasonal stationary fronts are not depicted in the daily subjective analyses, the frontal frequency pattern over southwestern North America is simpler than numerical. The usually troublesome extreme northeast Pacific area yields different solutions on the subjective and objective versions. In general, central and western ocean areas and the Arctic region show the best comparison between NMC and numerical patterns.

Prior to the development of the frontal analysis model described here, a simple, objective, quantitative method for measuring the location and intensity of fronts did not exist. Thus, frontal climatology has remained qualitative and descriptive over the years. However, it is obvious from the results of the prototype experiment of this chapter that quantitative frontal climatology is now feasible and that such a synthesis may be expected to relate well to geography, season, and the daily weather sequences.

# CHAPTER VIII

## RESUME' AND PROPOSALS FOR FURTHER STUDY

### Summary of Results

The following major accomplishments were achieved during the research study reported on here.

1. The most important result of the investigation is the development of the first operationally successful numerical-objective model for the synoptic-scale analysis of the location and intensity of hyperbaroclinic zones (HBZs). The scheme locates the constant pressure HBZ boundaries (i.e., fronts) along the axes of maximum baroclinicity gradient, simulating, in principle, the positioning of fronts by subjective analysts who adhere to the transition-zone concept of frontal phenomena. The model is easily adapted to a computer-oriented national weather service operation, as evidenced by the 1000 mb Northern Hemisphere numerical frontal analyses and prognoses being produced twice daily by the Fleet Numerical Weather Central, Monterey, California (FNWC).

2. A four-dimensional synoptic and statistical diagnosis of HBZ structure and motion is made possible by the development in 1. For this purpose, modeled and real-atmosphere virtual potential temperature data were employed to illustrate the relation of the merits and deficiencies of the analysis model to the numerically-processed and computed data. General characteristics of the HBZs are shown to be universal, although a

particular mode of numerical-data processing and computation, namely that of FNWC, was used throughout the study. Grid size, frontal-zone intensity (especially that due to zone width), air-mass dimension (i.e., width of the adjacent subbaroclinic zone), and use of layer versus mandatory-level temperatures are shown to be factors in yielding computed frontal structure which differs in degree from the real atmosphere as a function of the numerical manipulation of data. In general, the HBZs are weakened and the widths broadened by numerical processing, with these effects somewhat proportional to the original intensity in the transition zone. For a given mesh size, use of mean-layer vice single-level temperatures reduces the broadening effect on the HBZs. In this regard, use of the 1000/700 mb mean virtual potential temperature field, $\bar{\theta}^*$, was found to be suitable for generating 1000 mb (or surface) fronts. The reduction in mesh length, which must be closely tied to data density, appears to offer the most potential for improvement in accuracy and detail of numerical frontal analysis.

3. Several case studies from the years 1964-67 in extended time and space frames indicate the broader utility of the HBZ as compared to the conventional air-mass associated front. The numerical-analysis model has the advantage of locating fronts at any level, whether moving or orographically fixed, and not just those fronts separating air masses of recognizable thermal characteristics and dimensions. However, occluded structure is not evident from use of the model without empirical modification. Further, the relation of HBZs to vertical motion and cloud is shown to be complex and not operationally usable for locating HBZs.

4. The study also proposes a more elegant model for the purpose of analyzing the mesoscale structure of HBZs. The high resolution inherent

in vertical soundings, combined with a vertical extrapolation procedure, increases the resolution and amount of baroclinicity data to the extent that the fine structure of baroclinicity is clearly evident on the constant pressure mapping. The capacity of the major national weather centrals is not sufficient presently to take full advantage of such a model but it is offered as a prototype for future operational use.

## Proposed Areas for Further Research

The following areas for extended research on HBZs appears productive at this time.

1. It has been demonstrated that use of vertically-resolved thermal data allows the mesoscale structure of HBZs to be analyzed. In reality, the synoptic-scale HBZs comprise a multiple number of these subzones of hyperbaroclinicity (Kreitzberg, 1964). In this study such resolution was introduced at the baroclinicity stage of the HBZ analysis. It is proposed that the more basic field, temperature, be resolved by extrapolating the vertical temperature structure into the horizontal or constant pressure plane and then applying the subject model for the numerical analysis of HBZs. With a significant increase in data density, a judicious grid-size reduction can be fully effective in increasing the resolution of the analyzed HBZs. For a high-resolution model of this type, it is presumed that considerable smoothing of temperature and/or its derivatives will be necessary in order to locate the boundaries of the synoptic-scale HBZs, as found by previous researchers working with detailed frontal structure (e.g., Beniura, 1962).

2. The operational surface-front analysis model proposed here, utilizing $\bar{\theta}^*$, is essentially a thermal- as opposed to a weather-oriented scheme. With little guidance from national or international meteorological commissions, the latter approach is becoming popular with the field meteorologist as a convenient way of forcing apparent agreement with the satellite-observed cloud masses and bands. Perhaps regarding the frontal zone as the centrum of a circulation entity, (Bleeker, 1961; Eliassen, 1962; Todson, 1964; and Kirk, 1966) would allow relating vertical motion, and hence cloud, more intimately to baroclinicity, thus joining the thermal and weather concepts of the frontal zone. With the advent of night and day coverage by a multiple number of weather satellites, empirical modeling of vertical circulation, weather, and baroclinicity may now be feasible.

3. The limited substudy concerned with the long-period (as 30 days) frequencies and average intensities of HBZs indicated the potential use of these charts for discriminating between the fronts fixed to orography and those which are progressive. For operational analysis and forecasting it may be desirable to eliminate the orographic-type fronts in the daily analysis of HBZs. Some preliminary regional work contributing to the solution of this problem has been done by Reed (1961), who determined tables of average seasonal surface temperatures for synoptic map times over the western United States. Reed suggests, but does not show, that the deviation of temperature from a long-term mean be used to locate fronts in the complex mountain areas. The existence of monthly mean radiosonde temperatures, recently updated by the United States Navy (1966), makes such an experiment feasible. It is proposed that the HBZ model developed here be used in connection with the temperature anomalies.

4. Again, with reference to the substudy mentioned in 3 above, a computation of the average frequency and intensity of numerically-analyzed HBZs, as determined from a suitable period of several years, will allow the establishment of a much needed quantitative climatology of Northern Hemisphere fronts.

5. Operationally, there is need for a computer-plotted front in addition to the isolines of the front-location parameter since there is some subjectivity in locating the implied boundaries of the HBZ on meteorological charts of small scale. Some work has been done on this problem, using a directional third derivative of $\overline{\theta}^*$, but the effort was terminated due to the errors inherent in fields of such high-order derivatives.

Final Remarks

Experience in applying the numerically-analyzed fronts emphasizes the need for a man-machine mix (Snellman, 1969) due to the current gross grid size and poor horizontal resolution in the numerically-processed operational data. Using the $DG\overline{\theta}^*$ model, the computed frontal positions may be regarded as reasonably good first approximations to the actual locations. Mesoscale adjustment of the objectively-located fronts as a function of the adjacent and updated pressure, wind, and temperature observations is still deemed to be necessary. Such an approach does require plotted data as well as a knowledgable meteorologist but the time and effort involved is much less than a totally manual approach.

It is of interest to note the recent theoretical work by Williams (1967) which has as its goal the dynamical modeling of mesoscale frontogenesis from initial large-scale conditions of a simple, vertically-bounded,

atmosphere. Williams' developmental model yields vertically-sloping frontal zones whose boundaries may be located in terms of the characteristics of potential temperature and wind profiles, quite analogous to the operational frontal-analysis model described here.

# APPENDIX A

## PRELIMINARY EXPERIMENTS IN HYPERBAROCLINIC-ZONE ANALYSIS

### Experiments Using Wet-bulb Potential Temperature

The initial impetus for the study of numerical hyperbaroclinic zones (HBZs) came from some excellent statistical work on the air-mass distributions of wet-bulb potential temperature, $\theta_w$, published by Harley (1962). $\theta_w$ has been the prime parameter in the daily operational frontal-contour analyses emanating from the Central Analysis Office, Meteorological Service of Canada (CAO), since 1953.

Harley presents, among other things, monthly means, standard deviations, and modal values of $\theta_w$ in three air masses described by the Canadians as maritime tropical, maritime polar, and maritime arctic. His data sample is provided by a careful analysis of a full year (1957) of radiosonde observations from 89 stations in the area 25-90N and 15W to 170E across North America. The method used to determine an air-mass $\theta_w$ allows his statistics to be interpreted as usable climatological indicators of the warm-air edge of the HBZs separating two adjacent but dissimilar air masses. As an example, Table 14 contains the monthly means and standard deviations of frontal $\theta_w$s for the polar front, which separates maritime tropical from maritime polar air. The $\overline{\theta}_w$ values are taken from Harley, but rounded to the nearest .1C.

Some preliminary work, attempting to assess the utility of $\theta_w$ as a front-location parameter, is described in the following subsection. In

order to utilize the empirical results of Harley and yet limit the initial experiments on locating HBZ boundaries, the following conditions and procedures were imposed: (1) $\theta_w$ and $\nabla\theta_w$ are considered as the prime front-location parameters, (2) only the poleward boundary of tropical air (i.e., polar front) is located, (3) the 850 mb level is a suitable single test level, and (4) since objectivity is the goal, any successful subjective analysis scheme should be a prototype for a numerical-objective approach.

Table 14. Monthly mean $\theta_w$ and $\theta_e$ and their standard deviations, for the polar front, as analyzed by CAO.[e]

| Month | $\overline{\theta}_w$ (°C) | Standard deviation (°C) | $\overline{\theta}_e$ (°C) | Standard deviation (°C) |
|---|---|---|---|---|
| Jan | 14.0 | 1.1 | 42.1 | 3.1 |
| Feb | 14.0 | 1.0 | 42.2 | 3.0 |
| Mar | 14.2 | 1.0 | 42.6 | 2.9 |
| Apr | 14.9 | 1.0 | 45.0 | 3.0 |
| May | 15.5 | 1.3 | 46.7 | 4.0 |
| Jun | 16.8 | 1.3 | 50.8 | 4.4 |
| Jul | 17.7 | 1.0 | 53.9 | 3.7 |
| Aug | 17.7 | 1.1 | 53.9 | 3.8 |
| Sep | 17.4 | 0.9 | 52.9 | 3.0 |
| Oct | 16.5 | 1.0 | 49.8 | 3.3 |
| Nov | 15.6 | 1.0 | 46.8 | 3.3 |
| Dec | 14.9 | 1.1 | 44.8 | 3.3 |

## Relations of $\theta_w$ and $\nabla\theta_w$ to the Polar Front

Summer Case Study:
Manual Analysis

The National Meteorological Center (NMC) and CAO 850 mb polar-front analyses over North America, for 35 synoptic times (0000 GMT 21-26 May 1963, 0000 GMT 21 June to 1200 GMT 26 June 1963, and 0000 GMT 12 July to 1200 GMT 16 July 1963), were screened for their relationship to the $\theta_w$ field. The $\theta_w$ value at each radiosonde station was obtained graphically from the United States Naval Weather Service's standard thermodynamic chart, the AROWAGRAM, using transmitted radiosonde temperature and dew-point data.

Specifically, answers to the following equations were being sought from analyses of the 850 mb polar front on the NMC and CAO charts:

1. What is the relation of NMC and CAO $\theta_w$s along the front?

2. Are values of $\theta_w$ relatively uniform along either of the fronts?

3. Are frontal values of $\theta_w$ conservative with time?

4. In view of answers to 1, 2, and 3, do Harley's data assist in objectively placing an air-mass boundary?

With reference to these questions, analysis of the May, June, and July 1963 data indicated the following conclusions. The numbered paragraphs refer to the foregoing questions.

1. A sampling of the polar-front $\theta_w$s at longitude intervals of 5 deg over North America generated the percentage frequencies and averages shown in Table 15. Similarity of NMC and CAO frontal $\theta_w$s does exist in the mean, but apparently there are differences in $\theta_w$ values along the two versions of the polar front on a given day.

Table 15. Percentage frequency of wet-bulb potential temperature, $\theta_w$, along the 850 mb polar fronts analyzed by NMC and CAO.

| $\theta_w$ (°C) | Percentage Frequency | | | | | |
|---|---|---|---|---|---|---|
| | 21-26 May 1963 | | 21-26 June 1963 | | 12-16 July 1963 | |
| | NMC | CAO | NMC | CAO | NMC | CAO |
| 12 | | | 1 | 3 | | |
| 13 | | | | | | |
| 14 | 7 | | 5 | 2 | | |
| 15 | 3 | | 11 | 7 | | |
| 16 | 13 | 7 | 14 | 10 | 4 | |
| 17 | 15 | 28 | 12 | 12 | 16 | 22 |
| 18 | 36 | 36 | 22 | 46 | 30 | 28 |
| 19 | 23 | 26 | 14 | 9 | 26 | 26 |
| 20 | 3 | | 16 | 9 | 13 | 7 |
| 21 | | 3 | 2 | 2 | 4 | 2 |
| 22 | | | 3 | | 7 | 11 |
| 23 | | | | | | 4 |
| Average | 17.5 | 17.5 | 17.4 | 17.4 | 18.6 | 18.8 |
| Number of Cases | 39 | | 57 | | 46 | |

2. Inspection of the average frontal values of $\theta_w$ as a function of longitude, by analysis center, shows the geographical variation of $\theta_w$ along the front (Table 16). The variation is greatest in the case of NMC fronts. Apparently the polar-front values of $\theta_w$ are not uniform on the average, as indicated in Table 15 as well.

Table 16. Average wet-bulb potential temperature, $\theta_w$, as a function of longitude, along the 850 mb polar fronts, analyzed by NMC and CAO.

21-26 May 1963 (39 cases)

| | | Longitude (deg) | | | | | | |
|---|---|---|---|---|---|---|---|---|
| | | 75 | 80 | 85 | 90 | 95 | 100 | Average |
| $\theta_w$ | NMC | 15.8 | 17.7 | 17.6 | 17.8 | 18.4 | 18.0 | 17.5 |
| ($^oC$) | CAO | 16.9 | 17.9 | 18.0 | 17.7 | 18.5 | 17.7 | 17.9 |

21-25 June 1963 (57 cases)

| | | Longitude (deg) | | | | | | | | | | |
|---|---|---|---|---|---|---|---|---|---|---|---|---|
| | | 70 | 75 | 80 | 85 | 90 | 95 | 100 | 105 | 110 | 115 | 120 | Average |
| $\theta_w$ | NMC | 18.0 | 17.8 | 17.8 | 18.2 | 18.2 | 18.0 | 19.0 | 18.4 | 17.0 | 15.9 | 12.0 | 17.4 |
| ($^oC$) | CAO | 17.0 | 17.5 | 17.4 | 18.1 | 18.8 | 18.9 | 17.6 | 17.4 | 17.3 | 16.2 | 12.0 | 17.4 |

12-16 July 1963 (46 cases)

| | | Longitude (deg) | | | | | | | | | | |
|---|---|---|---|---|---|---|---|---|---|---|---|---|
| | | 70 | 75 | 80 | 85 | 90 | 95 | 100 | 105 | 110 | 115 | Average |
| $\theta_w$ | NMC | 17.1 | 17.6 | 18.2 | 18.3 | 18.7 | 20.1 | 19.0 | 19.4 | 18.1 | 17.4 | 18.6 |
| ($^oC$) | CAO | 17.2 | 18.0 | 18.9 | 18.6 | 19.4 | 19.9 | 18.7 | 19.8 | 17.9 | 17.2 | 18.8 |

3. Some measure of the conservativeness of frontal $\theta_w$ values and other features may be obtained by noting a characteristic day in the series. Fig. 45 for 0000 GMT and 1200 GMT 21 June 1963 shows the relation of NMC and CAO polar fronts to $\theta_w$ data and Harley's statistical estimate of the frontal positions.

4. Fig. 45 shows that the orientation of manually-analyzed and statistical frontal positions are similar but not coincident. In general, the temporal non-conservativeness and spatial non-uniformity of $\theta_w$ suggests the probable failure of trying to objectively locate fronts based on a single climatological value of $\theta_w$. But the preponderance of NMC and Canadian positions within one standard deviation ($\sigma$) of the monthly mean $\theta_w$ is suggestive of a statistical approach in which the warm-air boundary of the HBZ is searched for within the area bounded by $\bar{\theta}_w \pm k$, where $k \leq 3$ C.

Winter Case Study:
Numerical Analysis

The 1963 summer tests were considered at least encouraging enough to continue experimenting with the application of statistical values of $\theta_w$ for frontal analysis. However, since the aim was to develop an objective system operationally applicable to the Northern Hemisphere, use of numerically-processed data and fields[1] became necessary and computations of $\theta_w$ were converted to the numerical mode. In this connection an analytical expression for $\theta_w$ (Berry et al., 1945) of the following form was programmed for solution on FNWC's Control Data Corporation 1604 digital computer.

---

[1]Data were processed in accordance with FNWC's mass structure model as described in Chapter III.

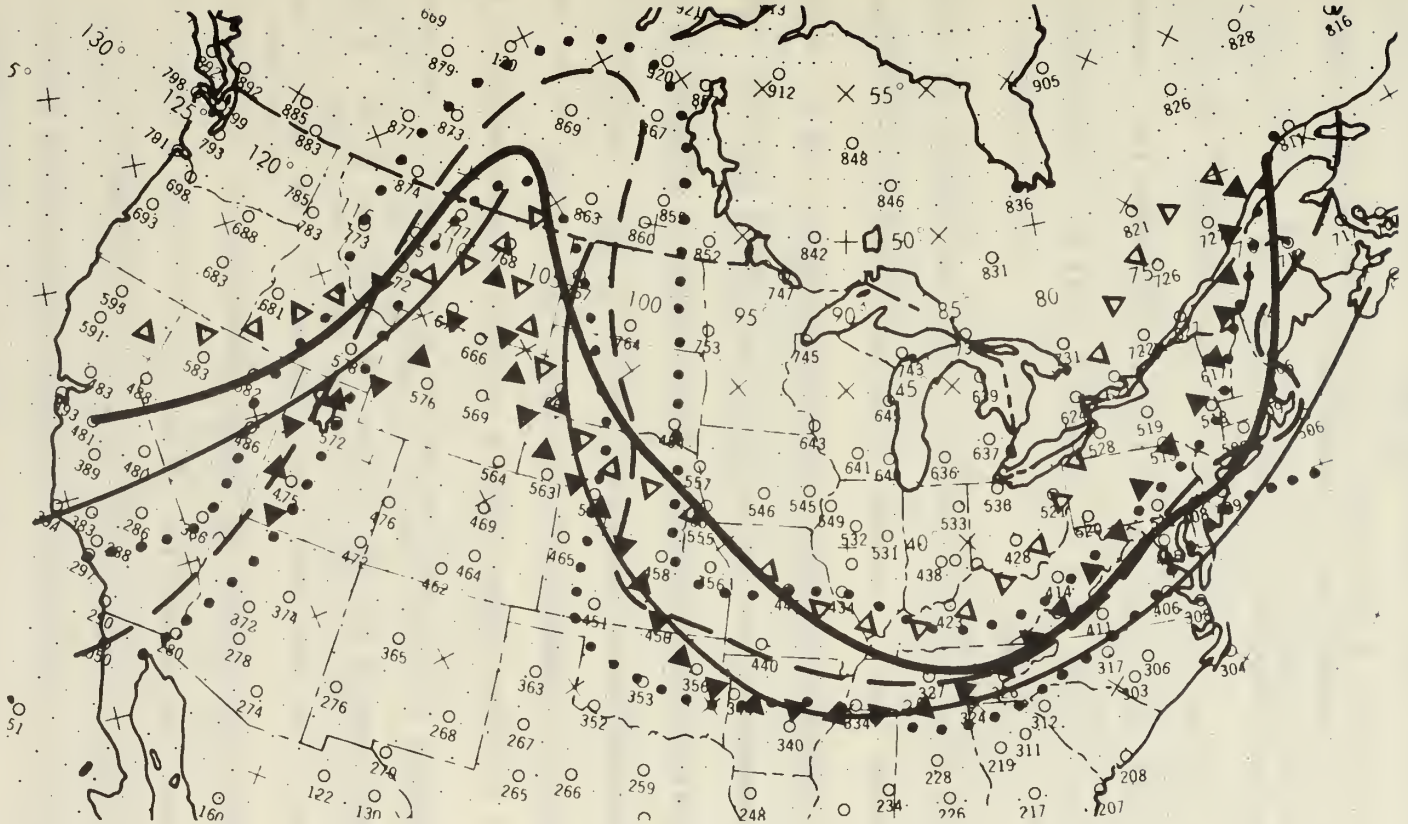

Fig. 45. 850 mb polar front analysis. 1200 GMT 21 June 1963: NMC front, heavy solid line; CAO front, thin solid line. Modal position (Harley, 1962), dashed line; $\theta_w \pm 1$ standard deviation (Table 14), dotted lines. NMC front, 0000 GMT 21 June 1963: ▽△▽. 1200 GMT NMC front at same $\theta_w$ as the 0000 GMT position: ▼▲▼.

$$\theta_w = \theta_e \exp - \left( \frac{[m_s L]\theta_w}{\theta_w C_p} + \frac{R_d e_s 1000}{1000 C_p} \right), \tag{25}$$

where

$$\theta_e = \theta \exp \left( \frac{L_c m_s}{C_p T_c} \right). \tag{26}$$

m is mixing ratio, L is latent heat of condensation, subscripts s and c indicate saturation and condensation levels, respectively, e is vapor pressure, 1000 is 1000 mb, and other notations are standard. Due to the limited nature of this experiment the various complex numerical approximations and iteration schemes used to compute $\theta_w$ will not be discussed here. Such are on file at FNWC.

The synoptic time 1200 GMT 5 February 1964 was chosen for experimentation in objective frontal analysis using the numerically-produced wet-bulb potential temperature field. In this case the field is actually wet-bulb virtual potential temperature, $\theta_w^*$, since FNWC's processed temperatures approximate virtual temperatures. Fig. 46 shows a portion of the 850 mb $\theta^*$ field over North America. The area within $\bar{\theta}_w + 3\sigma$, appropriate to February (Table 14), is regarded as the most likely region within which the polar front is located. Using $\theta_w^*$ as a suitable approximation to $\theta_w$, the first approximation to the position of the polar front is the zone (called search zone) between the $\theta_w^*$ isolines of 11.0C and 17.0C. Following the definition of the front used here (Chapter I), the line of maximum $\nabla\theta_w^*$ within the search zone became the second approximation to the polar front. In this case, the orientation of the axis of maximum $\nabla\theta_w^*$ is similar to the subjectively-located fronts, especially CAO, but locations differ. This and other tests of a like nature, although suggestive of the direction in which to pursue the research, did bring about the abandonment of

wet-bulb potential temperature as a front locator for the following reasons.

1. $\theta^*_w$ was being considered solely because of the existent air-mass statistics of Harley (1962). By using the Smithsonian Meteorological Tables (List, 1963) the $\theta_w$ statistics may be readily converted to their $\theta_e$ counterparts. Table 14 includes the monthly mean frontal values, $\bar{\theta}_e$, so determined.

2. $\theta^*_w$ computations are difficult and costly in computer time due to the multiple numbers of scans necessary to approximate $\theta^*_w$ to an acceptable degree of reliability. Consequently, the next testing phase, still following the lead of the Canadian statistical work, utilized numerically-computed $\theta^*_e$ vice $\theta^*_w$.

## Experiments Using Equivalent Potential Temperature

For reasons discussed above, further tests with $\theta^*_w$ were aborted in favor of the more easily computed equivalent virtual potential temperature, $\theta^*_e$, using a form of the analytical expression in Eq. (26).

One of the front-locator parameters developed is of the form:

$$F_i = \theta^{*n}_{e_i} \left|\nabla\theta^*_e\right|, \tag{27}$$

where i refers to polar, maritime, or arctic fronts; $\left|\nabla\theta^*_e\right|$ represents the magnitude of the gradient of $\theta^*_e$; and $\theta^{*n}_e$ is a normalized value of $\theta^*_e$, defined as

$$\theta^{*n}_{e_i} = \bar{\theta}^*_{e_i} - \left|\theta^*_e - \bar{\theta}^*_{e_i}\right|. \tag{28}$$

For the purpose of this experiment, $\bar{\theta}^*_{e_i} \pm k\sigma$ were regarded as equivalent to $\bar{\theta}_{e_i} \pm k\sigma$. The location of the front is taken as the axis of maximal values of $F_i$.

For the purpose of applying the scheme of Eq. (27) as a third approximation to the 850 mb polar front of 1200 GMT 5 February 1964 (Fig. 46), the following procedure is implemented. First, the $\theta_e^*$ lines are redesignated as $\theta_e^{*n}$ lines. Thus $\theta_e^*$ of 33.2C, 42.2C, and 51.2C become $\theta_e^{*n}$ of 33.2C, 42.2C, and 33.2C, respectively. Next, a search zone defined by $\bar{\theta}_e^* \pm 3\sigma$ is scanned for the axis of maximal values of $F_i$. Such a procedure forces location of the front between the maximum $\nabla\theta_e^*$ and $\bar{\theta}_e^*$, however always within the search zone. To assure this condition in the machine computation, the $F_i$ values may be arbitrarily set to small values outside the search zone. In those cases in which $\bar{\theta}_e^*$ does not lie in a direction toward warm air from the maximum $\nabla\theta_e^*$ the $F_i$ computation of the front location is less accurate than that dependent on the maximum $\nabla\theta_e^*$ alone.

Enhancement factors--In order to ensure placement of the front to the warm-air side of the axis of maximum $|\nabla\theta_e^*|$ in the search zone, a weighting factor, W, of dual form was used in combination with $F_i$ to generate $F'_i$, the final front-location parameter considered in this statistical synoptic approach. Thus,

$$F'_i = F_i \, W = \theta_{e_i}^{*n} \, |\nabla\theta_e^*| \, W, \tag{29}$$

and, as for $F_i$, the axis of maximal values of $F'_i$ locates the polar front.

At the boundary of and inside the search zone defined by $\bar{\theta}_e^* \pm 3\sigma$

$$W = W_1 = \left(\frac{\theta_e^*}{\bar{\theta}_e^* - 3\sigma}\right)^{\chi}, \tag{30}$$

where $\chi$ is a constant for a particular front. Thus, $W_1$ increases from one at the cold-side boundary to $(\bar{\theta}_e + 3\sigma)/(\bar{\theta}_e^* - 3\sigma)$ at the warm-side boundary of the search zone. $\chi$ values up to nine were used to enhance the search-area gradients of $\theta_e^*$.

Outside the search zone,

$$W = W_2 = \left(\frac{\theta_e^{*n}}{\bar{\theta}_e^{*}}\right)^{\chi}, \tag{31}$$

which always yields a fraction. $\chi$ values up to twenty were used to reduce the gradients outside the search area to extremely small fractional values.

As an example, following this scheme in the 1200 GMT 5 February 1964 case, Table 17 shows the weight factors and other information which result for the specified $\theta_e^*$ lines. For cases where maximum $\nabla\theta_e^*$ is at the location $\theta_e^* + 3\sigma$, $F'_i$ does not change the front-location estimate. For all other locations of a $\nabla\theta_e^*$ maximum, $F'_i$ yields a more consistent front-position estimate than $F_i$ or maximum $\nabla\theta_e^*$ alone. Fig. 46 shows the fourth approximation to the polar front using the $F'_i$ approach.

Table 17. Table of related values from Eqs. (27) and (29), as applied to a February 850 mb polar front.

| | $\theta_e^*$ ($^oC$) | $\theta_e^{*n}$ ($^oC$) | Symbolic weight factor | Magnitude of weight factor | $W = \frac{F'_i}{F_i}$ |
|---|---|---|---|---|---|
| | 24.2 | 24.2 | $W_2$ | 20 | 0.31 |
| $\bar{\theta}_e$-3 | 33.2 | 33.2 | $W_1$ | 9 | 1.00 |
| $\bar{\theta}_e$ | 42.2 | 42.2 | $W_1$ | 9 | 1.31 |
| $\bar{\theta}_e$+3 | 51.2 | 33.2 | $W_1$ | 9 | 1.69 |
| | 60.2 | 24.2 | $W_2$ | 20 | 0.31 |

Empirical adjustment to the statistical approach is almost endless. Wind shear or other front-associated parameters may be introduced as components of the weighting factor in Eq. (29), various values of $\chi$ may be

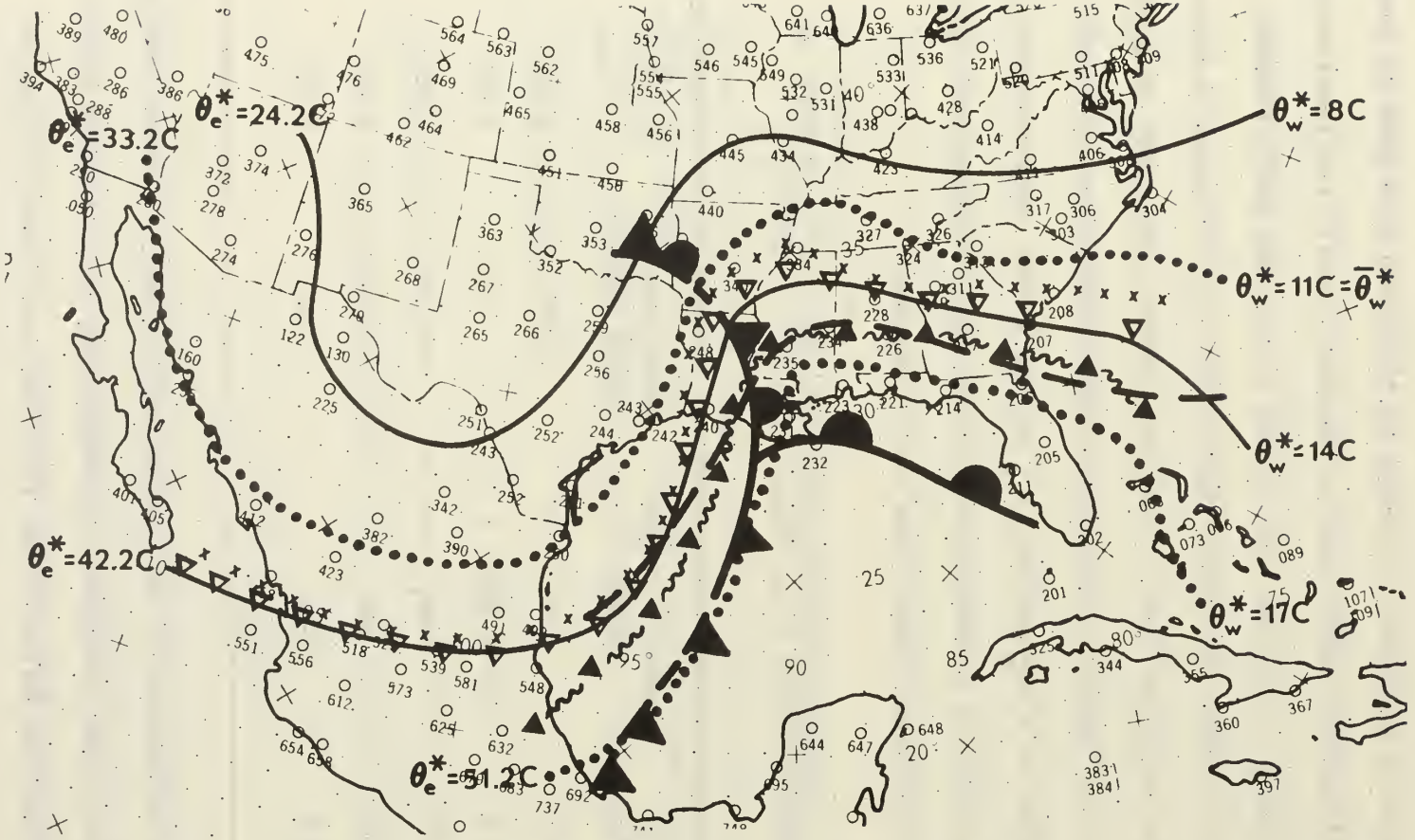


Fig. 46. Portion of 850 mb $\theta_w^*$ and $\theta_e^*$, at 1200 GMT 5 February 1964, computed numerically using a form of the analytical expressions in Eqs. (25) and (26). $\theta_w^*$ ($\theta_e^*$) at a 3C (9C) interval; first approximation to polar front is search zone bounded by $\bar{\theta}_w^* \pm 3\sigma^w$ ($\theta_e^* \pm 3\sigma$): dotted lines; second approximation is axis of maximum $\nabla\theta_w^*$ ($\nabla\theta_e^*$) in search zone: xxx; third approximation is axis of maximum $F_p$ from Eq. (27): $\nabla\nabla\nabla$; fourth approximation is axis of maximum $F'_p$ from Eq. (29): ▲∿∿▲. Canadian (▬ ▬) and NMC (▬◣) fronts shown.

employed in the enhancement scheme, and so on. A definite problem is proper hemispheric combination after each of the three fronts, polar, maritime, and arctic, is determined separately. Various arithmetic schemes of combining the individual $F_i$ or $F'_i$ fields were tried. The results were not satisfactory.

Since a more elegant, as well as a more utilitarian, model was developed (Chapter II), somewhat forced by the experiences just recounted, the illustrations here will be truncated to one experimental numerical plot of the arctic frontal field (Fig. 47), using a form of the enhancement scheme just outlined (Eq. 29). The axes of the elongated $F'_a$ isolines represent the arctic front. Note that this approach yields hemispherically continuous and mostly zonally-oriented fronts. Comparison with the Canadian arctic front is good, as might be expected from the dependence of $F'_a$ on Harley's values of $\overline{\theta}^*_e$; these values are used to some extent by the Canadians in their frontal analysis approach. A more extensive analysis of Fig. 47 is not warranted in view of the resume' immediately following.

## Summary

The various frontal-analysis schemes described in this Appendix restrict the fronts to a definite number, as well as to specific zones determined by air-mass statistics (Harley, 1962). That is, fronts outside the zone of $\overline{\theta}_e \pm 3\sigma$ for polar, maritime, and arctic fronts are not allowed. This is a very artifical restriction. Thus, final placement of a front is not dependent solely on factors involved in the definition of a front accepted here (see Chapter I) but rather on air-mass labels. A

Fig. 47. Frontal field, $F'_a$, generated for use in locating the 850 mb arctic front at 0000 GMT 5 March 1964. The search zone boundaries given by $F'_a = 1$: heavy lines. The axis of $F'_a$ within search zone locates the estimated position of the arctic front. The CAO version of the arctic front is shown for comparison: xxx.

dynamic-synoptic approach to the problem is desirable. Such is the model finally adopted, as described in Chapter II.

Further, $\theta_w^*$ and $\theta_e^*$ were abandoned as front-location parameters in favor of $\theta^*$ due to the relative inaccuracy of numerical moisture analyses. It was found that motorboating values and/or very low dew points were improperly rejected in the numerical processing procedures. This has the effect of giving excessive $\theta_w^*$ and $\theta_e^*$ values in the relatively cold dry air, thereby reducing the $\theta_w^*$ and $\theta_e^*$ gradients and causing the misplacement of the frontal positions. Additionally, detail inherent in the moisture field was not resolved by analysis procedures tuned to the gross mesh size appropriate to current-day numerical analyses. It might be added that some hope of improved and detailed moisture analysis has been given recently through at least partial incorporation of satellite data in the numerically-processed fields. However, objective frontal analysis experiments with parameters dependent on detailed moisture information are considered premature even to this date.

## REFERENCES


Anderson, R., B. W. Boville, and D. E. McClellan, 1955: An operational frontal contour-analysis model. Quart. J. R. Meteor. Soc., 81, 588-89.

Anderson, R. K., E. W. Ferguson, and V. J. Oliver, 1966: The use of satellite pictures in weather analysis and forecasting. World Meteorological Organization, Tech. Note No. 75, 184 pp.

Beniura, H., 1962: Mesoscale and microscale features of the lower portion of cold fronts. Master's Thesis, Agricultural and Mechanical College of Texas, College Station, Texas, 60 pp.

Bergeron, T., 1959: Methods in scientific weather analysis and forecasting; pp 440-74 of The atmosphere and sea in motion. Ed. B. Bolin. New York, The Rockefeller Institute Press in Association with Oxford University Press, 509 pp.

Berry, F. A., Jr., E. Bollay, and N. R. Beers, 1945: Handbook of meteorology. New York, McGraw Hill Book Co., 1068 pp.

Bjerknes, J., 1918: On the structure of moving cyclones. Geofys. Publik., Vol. 1, No. 2, 8 pp.

_____, 1951: Extratropical cyclones; pp 577-98 of Compendium of Meteorology. Ed. T. F. Malone. Boston, Mass., American Meteorological Society, 1334 pp.

Bleeker, W., 1961: Fronts and the jet stream; the front as a circulation system; a contribution to the UNESCO/WMO seminar on Mediterranean synoptic meteorology, Rome, 1958. Meteor. Abhand., Band IX, Heft I, 85-93.

Boucher, R. J., and R. N. Newcomb, 1962: Synoptic interpretation of some Tiros vortex patterns: a preliminary cyclone model. J. Appl. Meteor., 1, 127-36.

Brooks, C. E. P., J. E. McDonald, M. G. Wurtele, and others, 1959: Glossary of meteorology. Ed. R. E. Huschke. Boston, Mass., American Meteorological Society, 638 pp.

Clarke, L. C., and R. J. Renard, 1965: Evaluation of a numerical objective frontal analysis scheme. Presentation at 239th National Meeting of the Am. Met. Soc., Riverside, Calif. (Abstract: Bull. Amer. Meteor. Soc., 46, 145).

_____, 1966a: Objective frontal analysis. Tech. Note No. 24, U. S. Navy Fleet Numerical Weather Facility, Monterey, Calif. 40 pp.

_____, 1966b: The U. S. Navy numerical frontal analysis scheme: further development and a limited evaluation. J. Appl. Meteor., 5, 764-77.

Creswick, W. S., 1967: Experiments in objective frontal contour analysis. J. Appl. Meteor., 6, 744-81.

Danielsen, E. F., 1959: The laminar structure of the atmosphere and its relation to the concept of a tropopause. Archiv fur Met., Geoph. und Biokl., 11, 293-332.

_____, 1964: Report on Project Springfield. DASA 17, Hq., Defense Atomic Support Agency, Washington, D. C., 97 pp.

Defense Documentation Center, 1965: A report bibliography: forecasting baroclinic zones and frontal zones, ARB No. 037626, Scientific and Technical Information, Cameron Sta., Alexandria, Va., 332 pp. (originally classified as SECRET; declassified to UNCLASSIFIED by Naval Postgraduate School, Monterey, Calif., 16 Sept 65).

Dickson, R. R., 1967a: The weather and circulation of December 1966. Mon. Wea. Rev., 95, 148-52.

_____, 1967b: The weather and circulation of July 1967. Mon. Wea. Rev., 95, 700-04.

Eliassen, A., 1962: On the vertical circulation in frontal zones. Geofys. Publik. W. Bjerknes Memorial Vol. XXIV, 147-60.

Endlich, R. M., and G. S. McLean, 1957: The structure of the jet stream core. J. Meteor., 14, 543-52.

Galloway, J. L., 1958: The three-front model: its philosophy, nature, construction, and use. Weather, XIII, 3-10.

Godson, W. L., 1950: The structure of North American weather systems; pp 89-106 of Centenary proceedings of the Royal Meteorological Society. London, Royal Meteorological Society, 208 pp.

_____, 1951: Synoptic properties of frontal surfaces. Quart. J. R. Meteor. Soc., 77, 633-53.

Green, R. A., 1966: The weather and circulation of February 1966. Mon. Wea. Rev., 94, 345-50.

Haltiner, G. J., and F. L. Martin, 1957: Dynamical and physical meteorology, New York, McGraw-Hill Publ., 470 pp.

Harley, W. S., 1962: Distribution of wet-bulb potential temperature in North American air masses (1957) and a statistical analysis of results. Cir. 3622 (Tec 400) Met. Br., Dept. of Transport, Canada, 46 pp.

Hess, S. L., 1959: Introduction to theoretical meteorology. New York, H. Holt and Co., 362 pp.

Holl, M. M., J. P. Bibbo, and J. R. Clark, 1963: and Supplement, 1964: Linear transforms for state parameter structure. Tech. Memo. No. 1, second ed., Meteorology International, Inc., Monterey, Calif. 39 pp.

Holl, M. M., J. P. Bibbo, J. R. Clark, and C. A. Riegel, 1965: A multi-layer mass-structure model of the atmosphere. Presentation at 237th National Meeting of the Am. Met. Soc., jointly with Am. Geo. Un., Washington, D. C. (Abstract: Bull. Amer. Meteor. Soc., 46, 83).

Holl, M. M., 1966: The assimilation of wind observations in the analysis of the atmospheric mass structure, Qtrly Rpt #1, Project M-129, Meteorology International, Inc., Monterey, Calif., 16 pp.

Hughes, R. E., 1967: U. S. Naval Weather Service, Computer products manual. NAVAIR 50-1G-522. Dept. of the Navy, Washington, D. C., 261 pp.

Jacobs-Haupt, I., 1963: TIROS observations over the Mediterranean and North Africa: pp 323-32 in Proceedings of the first international symposium on rocket and satellite meteorology, Washington, D. C., April 23-25, 1962. Ed. H. Wexler and J. E. Caskey, Jr., Amsterdam, North Holland Publ. Co., and New York, John Wiley and Sons, Inc., 440 pp.

Jennings, W., 1964: First course in numerical methods. New York, The Macmillan Co., 233 pp.

Kirk, T. H., 1965: A parameter for the objective location of frontal zones. The Meteor. Mag., 94, 351-3.

_____, 1966: Some aspects of the theory of fronts and frontal analysis. Quart. J. R. Meteor. Soc., 92, 374-81.

_____, 1967: Discussion of some aspects of the theory of fronts and frontal analysis. Quart. J. R. Meteor. Soc., 93, 272-3.

Kreitzberg, C. W., 1964: The structure of occlusions as determined from serial ascents and vertically-directed radar. AFCRL Research Rpt., 64-26, 121 pp.

Krishnamurti, T. N., J. Nogues, and D. Baumhefner, 1966: Partitioning of the baroclinic vertical motions in a developing wave cyclone. Sc. Rpt. No. 1 (Contract No. AF 19(628)-4777, Project No. 6698, Task No. 669802), Dept. of Met., Univ. of Calif., Los Angeles, Calif., 33 pp.

List, R. J., 1963: Smithsonian meteorological tables, 6th Rev. Ed., Washington, D. C., Smithsonian Institution, 527 pp.

Ludlum, D. M., Ed., 1966: Weatherwatch, January and February 1966. Weatherwise, 19, 80-81.

_____, 1967: Weatherwatch, July 1967. Weatherwise, 20, 228-29, 242-43.

McClain, E. P., and E. F. Danielsen, 1955: Zonal distribution of baroclinicity for three Pacific storms. J. Meteor., 12, 314-23.

National Weather Records Center, 1966: Checked data. Asheville, N. C.

Neiburger, M., D. S. Johnson and C. Chien, 1961: Studies of the structure of the atmosphere over the eastern Pacific Ocean in summer. I. The inversion over the eastern North Pacific Ocean. Berkeley and Los Angeles, Calif., University of California Press, 94 pp.

Newton, C. W., 1958: Variations in frontal structure of upper-level troughs. Geophysica, 9, 357-75.

Palmen, E., 1951: The aerology of extratropical disturbances; pp 599-620 of Compendium of Meteorology. Ed. T. F. Malone. Boston, Mass., American Meteorological Society, 1334 pp.

Palmen, E., and C. W. Newton, 1951: On the three-dimensional motions in an outbreak of polar air. J. Meteor., 8, 25-39.

Petterssen, S., 1956a: Weather analysis and forecasting, Volume I, motion and motion systems. New York, McGraw-Hill Publ., 428 pp.

_____, 1956b: Weather analysis and forecasting, volume II, weather and weather systems. New York, McGraw-Hill Publ., 266 pp.

Posey, J. W., 1966: The weather and circulation of January 1966. Mon. Wea. Rev., 94, 275-82.

Reed, R. J., and F. Sanders, 1953: An investigation of the development of a mid-tropospheric frontal zone and its associated vorticity field. J. Meteor., 10, 338-49.

Reed, J. W., 1961: Surface temperature anomalies in mountain area weather analysis. Research Rpt. SC-4546(RR), Sandia Corp., Albuquerque, N.M., 18 pp.

Renard, R. J., 1967a: Further experiments in numerical analysis of baroclinicity. Progress Report No. 1, Research Contract 14215, Nav. Wea. Res. Fac., Norfolk, Va., 31 pp.

_____, 1967b: The application of numerical analysis of baroclinicity to the objective location of frontal zones. pp 179-99 of Air Wea. Serv. Tech. Rpt. No. 196, Proceedings of the Technical Exchange Conference, 4-7 April 1967, Monterey, Calif. Air Weather Service (MAC), United States Air Force, 302 pp.

_____, 1967c: Numerical baroclinic-zone analysis utilizing significant-level radiosonde data. Presentation at 47th Annual Meeting of the Am. Met. Soc., New York City. (Abstract: Bull. Amer. Meteor. Soc., 47, 905).

Renard, R. J., and L. C. Clarke, 1965a: Experiments on objective location of frontal zones. Presentation at 45th Annual Meeting of the Am. Met. Soc., New York City. (Abstract: Bull. Amer. Meteor. Soc., 45, 703).

_____, 1965b: Experiments in numerical objective frontal analysis. Mon. Wea. Rev., 93, 547-56.

_____, 1966: Present status of the U. S. Navy's experiments in numerical objective frontal analysis and prognosis. Presentation at Conference on Modern Methods of Weather Forecasting and Analysis, Chicago, Ill. (Abstract: Bull. Amer. Meteor. Soc., 47, 37).

Riehl, H., et al., 1952: Forecasting in middle latitudes. Meteorological Monograph, Vol. 1, No. 5, Boston, Mass., American Meteorological Society, 80 pp.

Riehl, H., M. A. Alaka, C. L. Jordan, and R. J. Renard, 1954: The jet stream. Meteorological Monograph, Vol. 2, No. 7. Boston, Mass., American Meteorological Society, 100 pp.

Sanders, F., 1955: An investigation of the structure and dynamics of an intense surface frontal zone. J. Meteor., 12, 542-52.

_____, 1963: Further research directed toward the study of relations of atmospheric flow to weather. Final Rpt (Contract No. AF 19 (604)-8373, Project No. 8641, Task No. 86410), Dept. of Meteorology, Mass. Inst. of Technology, Cambridge, Mass., 159 pp.

_____, 1967: A survey of frontal zones in the middle and upper troposphere; Appendix 5 of frontal structure and dynamics of frontogenesis. Dept. of Meteorology, Mass. Inst. of Technology, Cambridge, Mass., 333 pp.

Saucier, W. J., 1955: Principles of meteorological analysis. Chicago, Ill., Univ. of Chicago Press, 438 pp.

Sawyer, J. S., 1955: The free atmosphere in the vicinity of fronts. Geophys. Mem. No. 96, Meteorological Office, London, 24 pp.

_____, 1964: Meteorological analysis--a challenge for the future. Quart. J. R. Meteor. Soc., 90, 227-47.

Snellman, L. W., 1969: The man-machine mix in applied weather forecasting in the 1970s. Tech. Memo WR-40, Western Region, Weather Bureau, ESSA, Salt Lake City, Utah, 18 pp.

Taljaard, J. J., W. Schmitt, and H. vanLoon, 1961: Frontal analysis with application to the Southern Hemisphere. Notos, 10, 25-58.

Todson, M., 1964: A study of vertical circulations in a cold front. Part IV of Final Report, Air Force Cambridge Research Laboratory, Report 64-1014. 44 pp.

United States Air Force, 1965, 66, 67, 68: Quarterly Progress Reports for Automation. Hdq, Third Wea. Wing, Offutt AFB, Neb.

United States Navy, 1952: Practical methods of weather analysis and prognosis. NAVAER 50-1P-502. Office of the Chief of Naval Operations, Washington, D. C., 192 pp.

_____, 1966: Selected level temperatures and dew points for the Northern Hemisphere. NAVAER 50-1C-52. Office of the Chief of Naval Operations, Washington, D. C., 258 pp.

United States Weather Bureau, 1960: Synoptic meteorology as practiced by the National Meteorological Center. The NAWAC manual. NAVWEPS 50-1P-548. Government Printing Office, Washington, D. C., 38 pp.

Williams, R. T., 1967: Atmospheric frontogenesis: a numerical experiment. J. Atmos. Sci., 24, 627-41.

## INITIAL DISTRIBUTION LIST

| | | No. Copies |
|---|---|---|
| 1. | R. J. Renard<br>Department of Meteorology<br>Naval Postgraduate School<br>Monterey, California 93940 | 44 |
| 2. | Library<br>Naval Postgraduate School<br>Monterey, California 93940 | 2 |
| 3. | Dean of Research Administration<br>Naval Postgraduate School<br>Monterey, California 93940 | 2 |
| 4. | Defense Documentation Center<br>Cameron Station<br>Alexandria, Virginia 22314 | 20 |
| 5. | Naval Weather Service Command<br>Washington Navy Yard<br>Washington, D. C. 20390 | 2 |
| 6. | Officer in Charge<br>Naval Weather Research Facility<br>Naval Air Station, Building R-48<br>Norfolk, Virginia 23511 | 8 |
| 7. | Commanding Officer<br>Fleet Weather Central<br>Naval Air Station<br>Alameda, California 94501 | 1 |
| 8. | Officer in Charge<br>Naval Weather Service Environmental Detachment<br>FPO New York, New York 09597 | 1 |
| 9. | Commanding Officer<br>Fleet Weather Central<br>COMNAVMARIANAS, Box 12<br>FPO San Francisco, California 96630 | 1 |
| 10. | Commanding Officer<br>Fleet Weather Facility<br>P. O. Box 85<br>Naval Air Station<br>Jacksonville, Florida 32212 | 1 |

No. Copies

11. Commanding Officer — 1
Fleet Weather Facility
FPO Seattle, Washington 98790

12. Commanding Officer — 1
Fleet Weather Facility
Box 72
FPO New York, New York 09510

13. Commanding Officer — 2
Fleet Numerical Weather Central
Monterey, California 93940

14. Commanding Officer — 1
Fleet Weather Central
Box 110
FPO San Francisco, California 96610

15. Commanding Officer — 1
Fleet Weather Facility
Naval Air Station
Quonset Point, Rhode Island 02819

16. Commanding Officer — 1
Fleet Weather Central
Box 31
FPO New York, New York 09540

17. Commanding Officer — 1
Fleet Weather Facility
Naval Air Station, North Island
San Diego, California 92135

18. Commanding Officer — 1
Fleet Weather Facility, Box 30
FPO San Francisco, California 96652

19. Commanding Officer — 1
Fleet Weather Facility
Navy Department
Washington, D. C. 20390

20. Commanding Officer — 1
Fleet Weather Facility, Box 68
FPO San Francisco, California 96662

21. AFCRL-Research Library — 1
L. G. Hanscom Field
Attn: Nancy Davis/Stop 29
Bedford, Massachusetts 01730

No. Copies

22. Superintendent — 1
Naval Academy
Annapolis, Maryland 21402

23. Director, Naval Research Laboratory — 1
Attn: Tech. Services Info. Officer
Washington, D. C. 20390

24. American Meteorological Society — 1
45 Beacon Street
Boston, Massachusetts 02128

25. Atmospheric Science Group — 1
Engineering Science Bldg. 631
The University of Texas
Austin, Texas 78712

26. Bureau of Meteorology — 1
Attn: Library
Box 1289 K, G.P.O.
Melbourne Vic. 3001 AUSTRALIA

27. Program Director for Meteorology — 1
National Science Foundation
Washington, D. C. 20550

28. Office of Naval Research — 2
Department of the Navy
Washington, D. C. 20360

29. Commander, Air Weather Service — 2
Military Airlift Command
U. S. Air Force
Scott Air Force Base, Illinois 62226

30. Atmospheric Sciences Library — 1
Environmental Science Services Administration
Silver Spring, Maryland 20910

31. Chairman, Department of Meteorology — 1
Florida State University
Tallahassee, Florida 32306

32. Dr. R. Cecil Gentry — 1
Director, National Hurricane Research Laboratory
P. O. Box 8265, University of Miami Branch
Coral Gables, Florida 33124

33. Dr. Robert Simpson — 1
Director, National Hurricane Center
P. O. Box 8286
Coral Gables, Florida 33124

No. Copies

34. Dr. Frederick Sanders, Department of Meteorology — 1
Massachusetts Institute of Technology
Cambridge, Massachusetts 21038

35. Commanding Officer — 1
Fleet Weather Central
Naval Air Station
Norfolk, Virginia 23511

36. Chairman, Department of Meteorology — 1
San Jose State College
San Jose, California 95114

37. Director — 1
National Center for Atmospheric Research
Boulder, Colorado 80301

38. Dr. Noel E. LaSeur — 13
Department of Meteorology
Florida State University
Tallahassee, Florida 32306

39. Mr. Leo C. Clarke — 2
Fleet Numerical Weather Central
Monterey, California 93940

40. Mr. Herb Bomalaski — 1
Officer in Charge
U. S. Weather Bureau Station
Austin Straubel Airport
Green Bay, Wisconsin

41. Mr. Joseph Strahl — 1
Hydrology Division
U. S. Weather Bureau, ESSA
Grammax Building (8060 13th Street)
Silver Spring, Maryland 20910

42. Dr. Ed Zipser — 1
National Center for Atmospheric Research
Boulder, Colorado 80301

43. Mr. William H. Klein, Director — 1
Techniques Development Lab
U. S. Weather Bureau, ESSA
Grammax Building (8060 13th Street)
Silver Spring, Maryland 20910

44. Dr. Herbert Riehl, Department of Atmospheric Sciences — 1
Colorado State University
Fort Collins, Colorado 80301

No. Copies

45. Dr. George Cressman, Director — 1
Weather Bureau, ESSA
Grammax Building (8060 13th Street)
Silver Spring, Maryland 20910

46. Dr. C. W. Newton — 1
National Center for Atmospheric Research
Boulder, Colorado 80301

47. Dr. M. A. Shapiro — 1
National Center for Atmospheric Research
Boulder, Colorado 80301

Unclassified
Security Classification

## DOCUMENT CONTROL DATA - R & D

*(Security classification of title, body of abstract and indexing annotation must be entered when the overall report is classified)*

1. ORIGINATING ACTIVITY (Corporate author)
Naval Postgraduate School
Monterey, California 93940

2a. REPORT SECURITY CLASSIFICATION
Unclassified

2b. GROUP

3. REPORT TITLE

Hyperbaroclinic Zones: Numerical Analysis and Application to Fronts

4. DESCRIPTIVE NOTES (Type of report and, inclusive dates)
Technical Report, March 1970

5. AUTHOR(S) (First name, middle initial, last name)

R. J. Renard

| 6. REPORT DATE | 7a. TOTAL NO. OF PAGES | 7b. NO. OF REFS |
|---|---|---|
| March 1970 | 206 | 75 |

8a. CONTRACT OR GRANT NO.

b. PROJECT NO.

c.

d.

9a. ORIGINATOR'S REPORT NUMBER(S)

NPS-51RD0031A

9b. OTHER REPORT NO(S) (Any other numbers that may be assigned this report)

10. DISTRIBUTION STATEMENT

This document has been approved for public release and sale; its distribution is unlimited.

11. SUPPLEMENTARY NOTES

12. SPONSORING MILITARY ACTIVITY
Navy Weather Research Facility, Norfolk
Fleet Numerical Weather Facility, Monterey
Office of Naval Research, Washington, D.C.

13. ABSTRACT

An objective-numerical scheme for locating and specifying the intensity of hyperbaroclinic zones (HBZs) is presented and applied in both research and operational environments. The operational model, called DG$\theta$*, employs the isobaric gradient of virtual potential temperature ($\theta$*) to specify baroclinicity while a directional second derivative of $\theta$* is the parameter used to locate the HBZs and indirectly give a measure of their intensity.

The DG$\theta$* model is diagnosed from an analysis of modeled temperature profiles and a number of real-atmosphere temperature fields at 1000, 850, 700, and 500 mb, as taken from winter and summer situations in the years 1964-67. Consideration is given to location, intensity, frequency, slope, and vertical and horizontal distribution and consistency of the HBZs in relation to the numerical processing of data. A key synoptic time, 0000 GMT 6 March 1966, serves to exemplify analytical and diagnostic features of the HBZs. The numerically-analyzed 1000 mb fronts, produced operationally by Fleet Numerical Weather Central, Monterey, California since 1965, are statistically and graphically compared to subjectively-analyzed versions for winter and summer periods up to 30 days. The relation of the HBZ to vertical motion and cloud is illustrated by a case study from December 1966.

Experiments, using a high-resolution scheme for analyzing the HBZs, are also presented. A proposed model, employing parameters of vertical stability and isentropic slope, utilizes the thermal detail inherent in vertically-resolved radiosonde data to give an enhanced field of baroclinicity on the constant pressure surface. In addition, it is shown how the model may be coupled with a vertical extrapolation procedure to at least triple the amount of baroclinicity data used for HBZ analysis.

DD FORM 1 NOV 68 1473 (PAGE 1)
S/N 0101-807-6811

Unclassified
Security Classification

A-31408

| 14 KEY WORDS | LINK A | | LINK B | | LINK C | |
|---|---|---|---|---|---|---|
| | ROLE | WT | ROLE | WT | ROLE | WT |
| Numerical analysis | | | | | | |
| Baroclinicity | | | | | | |
| Hyperbaroclinicity | | | | | | |
| Fronts | | | | | | |
| Frontal zones | | | | | | |
| Air mass analysis | | | | | | |